Title
Experimental Investigation and Data-Driven Analysis of Binary and Multi-Component Droplet Evaporation

Author
Andalib, Sahar

Publication Date
2021

Peer reviewed|Thesis/dissertation

UNIVERSITY OF CALIFORNIA

Los Angeles

Experimental Investigation and Data-Driven Analysis of Binary and Multi-Component Droplet Evaporation

Dissertation Submitted in Partial Satisfaction of the Requirements for

Degree of Doctoral of Philosophy

in Mechanical Engineering

by

Sahar Andalib

2021

ABSTRACT OF THE DISSERTATION

Binary and Multi-Component Droplet Evaporation:

Experimental and Data-Driven Techniques

by

Sahar Andalib

Doctor of Philosophy in Mechanical Engineering

University of California, Los Angeles, 2021

Professor Hossein Pirouz Kavehpour, Chair

Sessile droplet evaporation is an omnipresent phenomenon both in nature and technologies such as biodiagnostics, microfabrication, inkjet printing, spray cooling, and agriculture irrigation. Evolution of single component sessile droplets has been extensively studied under various parameters. However, in real applications, sessile droplets usually consist of two or more components. It has been shown that the environmental conditions such as humidity and temperature substantially change the behavior of sessile droplets. The strong tendency of organic fluids to absorb water is an important factor in evaporation of these fluids in humid environment. The water vapor present in the surrounding adsorbs/absorbs and possibly condenses into the droplet transforming the droplet into a binary system. While the humidity of surrounding is typically an imposed condition resulting in unwanted effects for many industries, we have proposed that these undesired effects can be controlled and eliminated by tuning the temperature of the substrate. We have studied the combined effect of relative humidity of surrounding and substrate temperature on evaporation of methanol droplets. Our results demonstrated that the diffusion of water into the droplet can be limited by changing temperature of the substrate by both shortening the lifetime of droplet or increasing the temperature of the liquid-gas interface above the due point. Additionally, we have developed machine learning,

classification and regression, models to analyze the behavior of droplet under different conditions. We have shown that the regime of droplet evaporation can be accurately classified by analyzing the profile of the evolution of droplet macroscopic parameters. We have also demonstrated that the humidity of surrounding can be accurately estimated by analysis of droplet profile. Furthermore, the time evolution of diameter and contact angle are estimated by the regression model. As the number of components in the droplet increases, the underlying mechanisms become more complex. The proposed approach to analyze the dynamics of sessile droplet evaporation through data-driven techniques opens up ways to better understand the complicated physics behind multi-component droplet evaporation and in general intricate interfacial fluid mechanics problems. The combined effect of surrounding humidity and substrate temperature has been experimentally studied on the behavior of ternary droplet consisting of methanol, anise oil, and water. The simultaneous optical microscopy and infrared thermography revealed different mechanisms in the droplet such as hydrothermal waves, oil microdroplet nucleation, etc. Our results showed three stages in the evolution of hydrothermal waves during droplet lifetime. The experimental procedures and results in this work introduce easy and inexpensive method to control sessile droplet behavior which are crucial for the final product resolution in numerous applications.

The dissertation of Sahar Andalib is approved.

Adrienne G. Lavine

Jeff D. Eldredge

Kunihiko Taira

Hossein Pirouz Kavehpour, Committee Chair

University of California, Los Angeles

2019

To the memory of my father
To my mother and my husband

Contents

1 Introduction **1**

1.1 Sessile Droplet Evaporation 1

1.2 Application and Motivation 1

1.2.1 Droplet-Based Biodiagnostics 2

1.2.2 Inkjet Printing 4

1.3 Single-Component Droplet Evaporation 4

1.4 Binary Droplet Evaporation 7

1.5 Data-Driven and Machine Learning Techniques in Droplet Evaporation 9

1.6 Ternary Droplet Evaporation 10

2 Combined Effect of Relative Humidity and Substrate Temperature on Evaporation of Methanol Droplet **12**

2.1 Abstract 12

2.2 Introduction 13

2.3 Experimental Techniques 19

2.4 Results and Discussion 21

2.4.1 Droplet evolution 21

2.4.2 Evaporation rate 23

2.4.3 Regime map . . . 25
2.5 Conclusion . . . 27

3 Machine Learning Application in Prediction of Environmental Condition through Evaporation of a Liquid Droplet 30

3.1 Abstract . . . 30
3.2 Introduction . . . 31
3.3 Experimental Data . . . 33
3.4 Machine Learning and Data processing . . . 34
3.4.1 Methodology . . . 34
3.4.2 Data Selection and Models . . . 36
3.4.3 Data Partitioning . . . 37
3.4.4 Correlation Between Features . . . 37
3.5 Estimation Results . . . 38
3.5.1 Naive Bayes . . . 38
Cross Validation . . . 39
Forward Feature Selection . . . 41
3.5.2 Bagged Decision Tree . . . 42
Feature Importance . . . 42
3.6 Validating the Model . . . 43
3.6.1 Effect of Input Variables . . . 46
3.6.2 Effect of Data Distribution . . . 47
3.7 Conclusions and Future Work . . . 50

4 Data-Driven Time-Dependent State Estimation for Interfacial Fluid Mechanics in Evaporating Droplets 52

4.1 Abstract . . . 52
4.2 Introduction . . . 54
4.3 Results . . . 58
4.3.1 Physics of Droplet Evaporation . . . 58
4.3.2 Regime Classification . . . 61
4.3.3 Relative Humidity Estimation . . . 65
4.3.4 Diameter and Contact Angle Estimation . . . 66
4.4 Discussion . . . 69
4.5 Methods . . . 72
4.5.1 Experimental Setup and Procedures . . . 72
4.5.2 Data Acquisition . . . 73
4.5.3 Data Partitioning and Processing . . . 74
4.5.4 Training and Testing . . . 74
4.5.5 Cross Validation . . . 75
4.5.6 Validation . . . 75
4.5.7 State Estimation . . . 75
4.5.8 Performance Criteria . . . 76
4.5.9 Classifiers . . . 76

5 Onset of Ouzo Effect in Evaporative Mixture Droplet: Relative Humidity and Substrate Temperature Considerations 78

5.1 Abstract . . . 78
5.2 Introduction . . . 79
5.3 Experimental Methods . . . 82
5.4 Results and Discussion . . . 84

5.4.1 Relative Humidity Effect at Room Temperature 85
5.4.2 Combined Effect of Substrate Temperature and Relative Humidity of Surrounding 87
Optical Visualization 87
Infrared Thermography 91
5.5 Conclusion 97

6 Conclusion **99**

A Empirical Model on Methanol Droplet Evaporation **106**

B Ternary Diagram of Methanol- Water- Anise Oil **111**

C Empirical Model on Evaporation of Ternary Droplet **113**

References **126**

List of Figures

1.1 a) Sessile droplet of water on PDMS coated glass substrate; b) schematic of droplet and its relevant parameters. 2

1.2 a) Succesive microscopic images of droplet evaporation in the absence of biotin; b) successive images of droplet evaporation in the presence of biotin; c) microchannel schematic; d) schematic of flow with particles inside microchannel; e) schematic of droplet evaporation in the presence and absence of biotin biomarker. Adapted from Hurth et al. [41] 3

1.3 a) Forces on droplet at the contact line; b) schematic of droplet evolution in moving contact line phase; c) schematic of droplet evolution in pinned contact line phase. 6

1.4 Evaporation of water droplet on glass slide: a) evolution of diameter, D, volume, V,and contact angle, θ, over time, t; b) successive images of side view. Adapted from [4] 6

1.5 Schematic of a single-component, binary (two-component), and multi-component sessile droplet 7

2.1 Droplet Shape Analyzer (DSA100) from Krüss with (1) environmental chamber; (2) controlled-volume dosing system; (3) viewing and illumination windows; (4) controlled temperature substrate (Peltier plate); and (5) adjustable x-y-z stage 20

2.2 Time evolution of contact angle (), base diameter (), and volume () for relative humidity of 20% (a,b,c); 50% (d,e,f); 80% (g,h,i) with substrate temperatures of 15^oC (a,d,g); 25^oC (b,e,h); and 35^oC (c,f,i). 22

2.3 Time evolution of volume during evaporation of droplets at substrate temperatures of 15^oC (a); 25^oC (b); and 35^oC (c) at relative humidity of 20% (), 50% (), and 80% (). (d) initial evaporation rate calculated as rate of change of volume with respect of time at the beginning of evaporation. 25

2.4 Relative humidity and substrate temperature regime map of droplet evaporation showing distinct droplet behavior regions 27

3.1 a: Schematic of a droplet on a solid surface; b: image of the experimental set up including environmental chamber and dosing system; reprinted from Andalib et al. [1] 34

3.2 Experimental data on evolution of methanol: contact angle (_), base diameter (_), and volume (_)reprinted from Andalib et al. [1] 35

3.3 Schematic of data partitioning 37

3.4 Covariance matrices for three different models: a) model a that includes only contact angle and time both in dimensionless form; b) model b which has contact angle, time, temperature, and diameter all in dimensionless form; c) model c that has the same variables as model b but all in dimensional form. 38

3.5 Confusion matrices with Naive Bayes (a,b,c) and Bagged Decision Tree algorithms (d,e,f) for three models: model a that includes contact angle and time as input variables, both in dimensionless form; model b which consists of contact angle, time, temperature, and diameter as input variables, all in dimensionless form; and model c which has the same input variables as model b, but all in dimensional form. 40
3.6 Out of bag feature importance for Bagged Decision Tree feature with three different models 43
3.7 Validation error plots for Navie Bayes (a,b,c) and Bagged Decision Tree algorithm (d,e,f) with three models. Error values are listed in Table 3.5 . . . 44
3.8 Relative humidity prediction over time with model a with Bagged Decision Tree (a,b,c); Naive Bayes (d,e,f); and experimental data on time evolution of contact angle (g,h,i). Each row of the Figure corresponds to a single experiment: RH = 20% (first row), RH = 50% (second row), and RH = 80% (third row). 46
3.9 Error plots with uniform input data distribution: Naive Bayes (a,b,c); Bagged Decision Tree (d,e,f). Error values are listed in Table 3.6 48
3.10 Naive Bayes relative humidity prediction over time and experimental data. Each row of the Figure represents a single experiment: RH = 20% (first row) and RH = 50% (second row). 49

4.1 a) Schematic of the experimental setup with macroscopic parameters of droplet shown in the inset; b) regime map of droplet evaporation (top-left) under various relative humidity (RH) of surrounding and substrate temperature (T), evolutions of nondimensional contact angle, volume, and diameter versus time for evaporation-dominated (bottom-left), transition (top-right), and condensation-dominated (bottom-right) regimes. Each scale bar in droplet images represents a length of 1mm. The schematic is made using free and open-source software Inkscape (Harrington [38]) 59

4.2 Results of regime classification: a) correlation matrix for parameters in droplet evaporation; b) results of test set for regime detection illustrated with confusion matrices for Naïve Bayes (NB) and decision tree (DT) algorithms; c) point-by-point validation results with NB and DT classifiers for regime detection with experimental data of droplet evaporation for RH = 80% and T = 35°C; d) point-by-point results of estimation set with NB and DT classifiers for regime detection with experimental data of droplet evaporation for experiment #4 (RH = 75% and T = 25°C) in estimation set. The colors in c and d correspond to the regime colors used in Figure 4.1.b. 62

4.3 Relative humidity regression results: a) test set; b) validation; c) estimation. Markers for all colors in (b) represent different temperatures as shown in legend. Markers and colors in (c) are the same as in (a). 66

4.4 Diameter (D*) and contact angle (θ^*) regression results: a) test set; b) validation set; c) estimation set; d) diameter estimation with quadratic regression for E3 (top) and contact angle estimation with third-order polynomial regression for E1 (bottom). 71

5.1 Schematic of experimental setups: a) optical microscopy from the top for studying the sole effect of humidity; b) simultaneous optical visualization from the side and infrared thermography from the top for studying the combined humidity and substrate temperature effect. 84
5.2 Successive images of methanol and anise oil mixture droplet; a) RH = 20 %, b) RH = 50 %, c) RH = 80 % all at room temperature; d) time evolution of area at different relative humidity of the environment and room temperature 88
5.3 Dimensionless diameter of droplet at the onset of oil ring for different relative humidity of surrounding 89
5.4 Evolution of diameter and contact angle under different relative humidity and substrate temperature values for a mixture droplet of methanol-anise oil. D and θ are the diameter and contact of droplet. D^* and θ^* are the diameter and contact angle of the middle section. Onset subscript corresponds to the onset of the oil ring in the droplet. 90
5.5 Ternary methanol-anise oil-water droplet at $RH = 80\%$ and $T = 15°C$; a) CCD camera side view, b) IR camera top view. 91
5.6 Time evolution of the number of hydrothermal waves: a) $RH = 70\%$, $T = 35°C$; b) $RH = 20\%$, $T = 15°C$. The blue circular markers represent the number of primary hydrothermal waves and the grey triangular markers correspond to the number of secondary hydrothermal waves. The snapshot of droplet with IR camera are connected to their corresponding data points in the plots. The horizontal time axes are not uniformly scaled. . 93

5.7 Number of hydrothermal waves (HTWs) versus time at different relative humidity (RH) of surrounding and substrate temperature (T); inset shows the early sharp decline in number of waves in log-log scale. The markers are similar to Figure 5.7. 95

5.8 Scaled number of hydrothermal waves versus scaled normalized time for various relative humidity of surrounding and substrate temperatures in log-log scale. Experimental data (different shades and symbols) and fit by power law $N_w = a(d_0/Lc)(\Delta T/T_{amb})(RH(t/t_f))^b$ with $a = 7.13$ and $b = -0.301$. 96

A.1 a) Geometry of the mathematical model. Free surface of droplet, $z = h$, is a spherical cap with radius R, contact radius R, and contact angle θ. The arrows show the evaporative flux from the free surface of the droplet into the surrounding gas. Adapted from Stauber et al. [89]. 107

A.2 Time evolution of volume for methanol droplet evaporation: empirical model vs. experimental data. 110

B.1 Ternary diagram of methanol- water- anise oil. The orange shaded represents the region where oil microdroplet nucleation occurs, i.e., Ouzo effect. . 112

C.1 Time evolution of volume for methanol- anise oil droplet evaporation: empirical model vs. experimental data. 115

List of Tables

3.1 Class and features for the classification problem 36

3.2 Description of models 37

3.3 Average test error (plus standard deviation) with 10-fold cross validation for different models 40

3.4 Results of Sequential Feature Selection for Naive Bayes Classifier 41

3.5 Validation error values (plotted in Figure 3.7) 44

3.6 Validation error values for uniform input data distribution (plotted in Figure 3.9) 49

4.1 Regime classification results on test set: standard metrics for two different classifiers 61

4.2 Regime classification results on validation set under each specific RH and T condition with two different classifiers 63

4.3 Results of regime estimation for four experiments under new conditions unseen by the model. The true regime of each experiment is shown on the regime map in Figure 4.1b. 64

Acknowledgment

I would like to take this opportunity to acknowledge those who helped throughout my doctoral program. First, I want to thank my advisor, Professor Hossein Pirouz Kavehpour, for his support, guidance, and motivation throughout my studies at UCLA. Second, I want to thank Professor Kunihiko Taira for his invaluable guidance and support throughout the last year of my doctoral program. I would like to thank my mother for her endless love, motivation, and sacrifice without whom I would not be able to finish my studies. I want to thank my beloved husband, Dr. Nima Jabbari, whose everyday support and help gave me the energy to keep making progress in my doctoral studies. I would also like to thank my committee members Professor Adrienne Lavine and Professor Jeff Eldredge for their efforts and contribution to this dissertation.

I would also like to thank my mother, Jamileh Soroushan. Her endless love, support, and sacrificesustained me throughout my life. I would like to dedicate this dissertation to my father, Akbar Andalib, whose memory has always been a great inspiration throughout my entire life. Lastly, I would like to thank my loving husband, Dr. Nima Jabbari, without his constant support andencouragement, my Ph.D. would not be possible.

VITA

2006 - 2010 B.Sc. (Mechanical Engineering), University of Tabriz, Iran
2010 - 2013 M.Sc. (Mechanical Engineering), University of Tabriz, Iran
2014 - 2017 M.Eng. (Mechanical Engineering), Iowa State University, USA

Publications

Journal articles:

- **Andalib, Sahar**, Kunihiko Taira, and H. Pirouz Kavehpour. "Data-driven time-dependent state estimation for interfacial fluid mechanics in evaporating droplets." Scientific Reports (2021).
- Alshehri, Ali, **Sahar Andalib**, and H. Pirouz Kavehpour. "Numerical modeling of vapor condensation over a wide range of non-condensable gas concentrations." International Journal of Heat and Mass Transfer 151 (2020): 119405.
- **Andalib, Sahar**, Ali Alshehri, and Pirouz Kavehpour. "Combined effect of relative humidity and substrate temperature on evaporation of methanol droplet." Journal of Coatings Technology and Research 16, no. 6 (2019): 1691-1698.

Conference papers:

- **Andalib, Sahar**, Kunihiko Taira, and H. Pirouz Kavehpour. "Analysis of a Binary Sessile Droplet Evolution through Machine Learning Algorithms". In 5th International Conference on Droplets (2021).
- **Andalib, Sahar**, H. Pirouz Kavehpour. "Ouzo Effect in Droplet Evaporation under Controlled Environmental Condition". In 5th International Conference on Droplets (2021).
- **Andalib, Sahar**, Kunihiko Taira, and H. Pirouz Kavehpour. "Data-Driven Analysis of Contact Line." Bulletin of the American Physical Society (2020).
- **Andalib, Sahar**, Ali Alshehri, and Pirouz Kavehpour. "Effect of a second component in organic droplet evaporation: initially present versus absorbed during the process." In APS Division of Fluid Dynamics Meeting Abstracts, pp. M04-031. (2019).
- **Andalib, Sahar**, and Pirouz Kavehpour. "Effect of Evaporation Rate on Stick-Slip Behavior of the Contact Line." Bulletin of the American Physical Society 63 (2018).

- **Andalib, Sahar**, and Pirouz Kavehpour. "Experimental Investigation of Evaporation Rate of a Droplet on Behavior of the Contact Line." In: 19th International Coating Science and Technology Symposium (2018)
- **Andalib, Sahar**, and Pirouz Kavehpour. "Fluorescence microscopy of precursor films in evaporating drops." In Southern California Flow Physics Symposium XII (2018).
- **Andalib, Sahar**, and Pirouz Kavehpour. "Fluorescence microscopy of precursor films in evaporating droplets." In APS Division of Fluid Dynamics Meeting Abstracts, pp. Q11-003 (2017).

In preparation:

- **Andalib, Sahar**, Kunihiko Taira, and H. Pirouz Kavehpour. "Machine Learning Application in Prediction of Environmental Condition through Evaporation of a Liquid Droplet."
- **Andalib, Sahar** and H. Pirouz Kavehpour. "Onset of Ouzo Effect in Evaporative Mixture Droplet: Relative Humidity and Substrate Temperature Considerations."

Chapter 1

Introduction

1.1 Sessile Droplet Evaporation

Sessile droplet forms when a drop of liquid is deposited on a solid surface. The gravitational forces can be neglected if the size of droplet is smaller than the capillary length ($L_c = \sqrt{\sigma/\rho g}$), where σ, ρ, and g are surface tension of liquid-gas interface, density of liquid, and gravitational acceleration, respectively. The liquid molecules diffuse into surrounding gas and the droplet vanishes eventually. The behavior of sessile droplet during evaporation can be described by a couple of parameters such as the base diameter of droplet, volume, and contact angle. Contact angle is the angle that forms at the three phase contact line where all three solid, liquid, and gas meet. This angle is measured from the liquid side in the droplet (see Figure 1.1).

1.2 Application and Motivation

Sessile droplet evaporation is an amnipresent phenomenon both in nature and numerous industries such as biodiagnostics, inkjet printing, microfabrication, spray cooling, and agricultural irrigation [63, 10, 62, 5, 22, 47, 60, 85, 83, 88, 58, 41, 93, 34]. Understanding

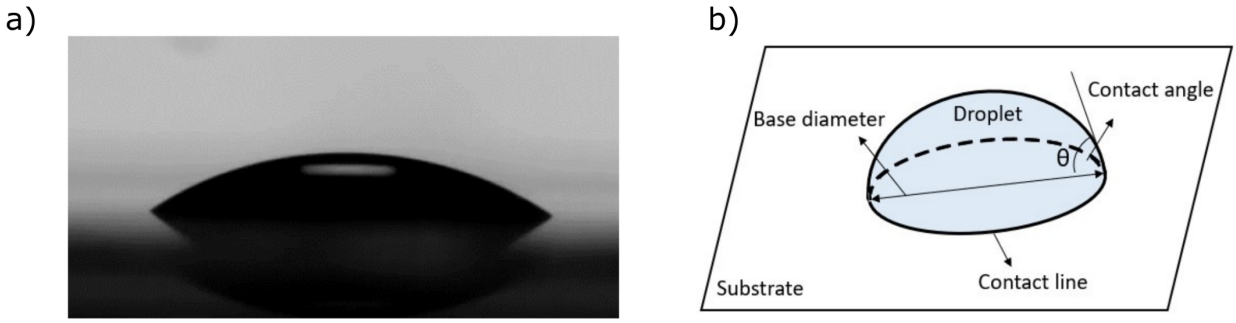

FIGURE 1.1: a) Sessile droplet of water on PDMS coated glass substrate; b) schematic of droplet and its relevant parameters.

the mechanisms of evaporation and the effect of different parameters are of great importance to control the behavior of droplet and tune the unwanted influence of environment. This is a crucial step to achieve better resolution and quality of the products involving evaporative menisci.

1.2.1 Droplet-Based Biodiagnostics

Droplet-based biosensors are being used extensively to detect different target disease. Trantum et al. [93] and Gulkta et al. [34] have used fluorescence microscopy and biomarkers to detect malaria in droplets containing the target molecules. Hurth et al. [41] suggested a low-cost fast biosensing mechanism by employing the biological bonding force between biotin and streptavidin. They observed different morphology of the stains after droplet evaporation in the presence and absence of biotin. They also performed microchannel experiments to estimate the biological bonding force between biotin and streptavidin (see Figure 1.2).

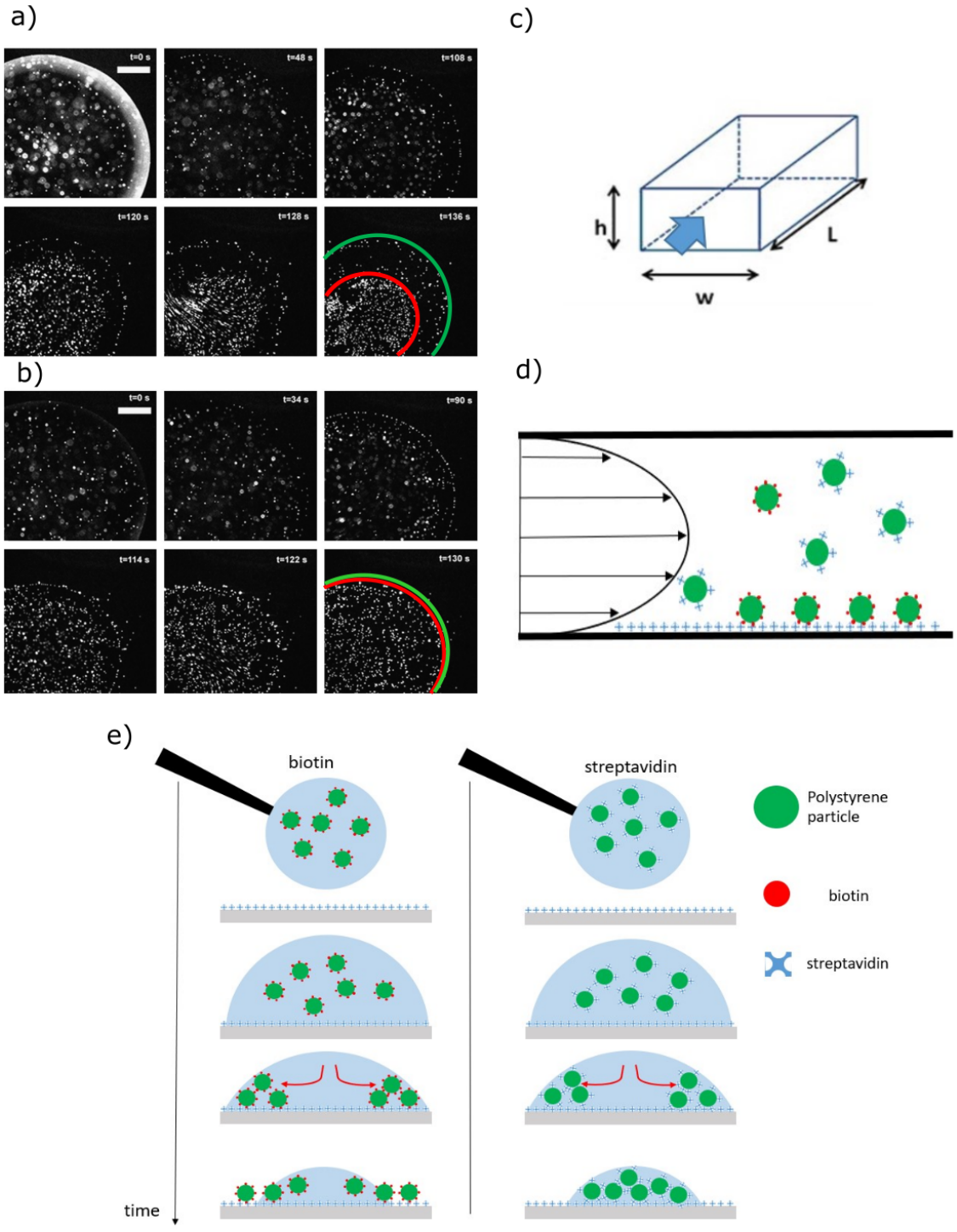

FIGURE 1.2: a) Succesive microscopic images of droplet evaporation in the absence of biotin; b) successive images of droplet evaporation in the presence of biotin; c) microchannel schematic; d) schematic of flow with particles inside microchannel; e) schematic of droplet evaporation in the presence and absence of biotin biomarker. Adapted from Hurth et al. [41]

1.2.2 Inkjet Printing

Inkjet printing consists of individual droplets of ink deposited on the surface. The final resolution of the printing process is highly dependant on how evenly the ink particles are distributed after evaporation of the solvent. The environmental conditions such as humidity and temperature highly influence the behavior of ink droplets. For example, at higher humidity of surrounding, the lifetime of droplet is noticeably prolonged which makes the drying process very long. The surface tension gradient along the interface strongly affects the distribution of ink particles. In order to achieve high resolution prints, the surface tension gradients need to tuned.

1.3 Single-Component Droplet Evaporation

Anytime we spill coffee or any other beverage, the stains after evaporation of the drops look darker at the edge. This color difference between the periphery and center of the stains are caused by a well-known mechanism called coffee ring effect. Sessile droplet evaporation has gained increasing attention from scientific community for about twenty-five years now by the original work of Deegan et al. [24]. In this work they showed that the evaporation flux is not distributed evenly along the liquid-gas interface and increases the radial distance increase. In fact, the maximum evaporation occurs at the contact line of droplet which derives a radially outward flow inside droplet. This outward flow brings more liquid and potential particle to the contact line to replenish the evaporated liquid. Figure 1.3.a illustrates the acting forces on droplet at the contact line. The red arrows represent the interfacial forces and the green force shows the surface friction force. The sum of interfacial forces tend to contract the droplet while the surface friction force resists the contraction. Therefore, how droplet evolves depends on the magnitude of these

forces. Figure 1.3.b and c demonstrate the schematics of droplet evolution for two scenarios. If surface tension (interfacial) force is much larger than the surface friction force, the contact line will recede and contact angle remains relatively constant 1.3.b. On the other hand, if surface friction force is much larger than surface tension force, the contact line is pinned and the volume loss due to evaporation is only noticed by reduction in contact angle. As contact angle decreases, the horizontal component of surface tension increases due to increase in $\cos(\theta)$. Figure 1.4 shows a water droplet evaporation on a glass slide. As seen, during the pinned region diameter remains relatively constant and contact angle and volume decrease. Once the contact angle reaches a threshold where surface tension force overcomes the surface friction force, droplet experiences a sudden contraction in its diameter. The droplet stays pinned again until the next contraction occurs. This is called stick-slip evaporation mode which is mainly observed for water droplets.

Various parameters influence the behavior of droplet during evaporation. It is observed that increasing the substrate temperature reduces surface tension which in turn enhances droplet pinning. It is also shown that adding surfactant reduces surface tension of water droplets and enhances pinning of droplet during evaporation [77]. Sefiane and Tadrist observed that reducing the surrounding pressure results in sudden contraction of water droplets while under atmospheric pressure the droplet undergoes smooth transition [74]. The effect of substrate thermal conductivity has also been investigated on evaporation of pure liquid droplets. Ristenpart et al. [69] concluded that the ratio of thermal conductivity of substrate and liquid determines the direction of temperature gradient along the interface and hence changes the resulting Marangoni flow. David et al. [21] reported that the difference in evaporation rate between substrates with different thermal conductivity is more pronounced for lower pressure of surrounding.

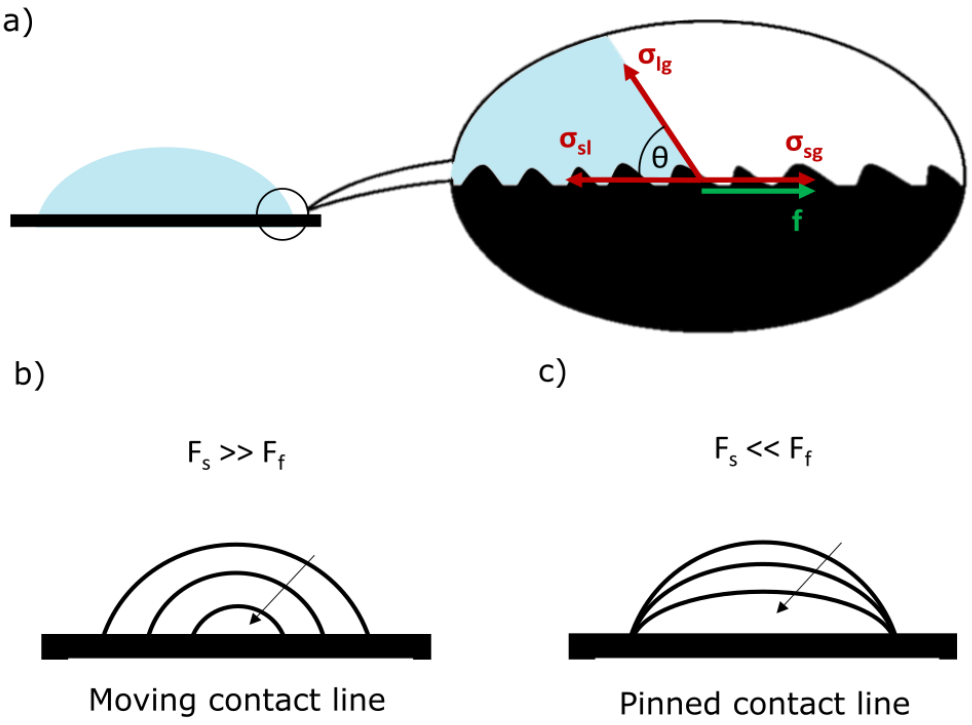

FIGURE 1.3: a) Forces on droplet at the contact line; b) schematic of droplet evolution in moving contact line phase; c) schematic of droplet evolution in pinned contact line phase.

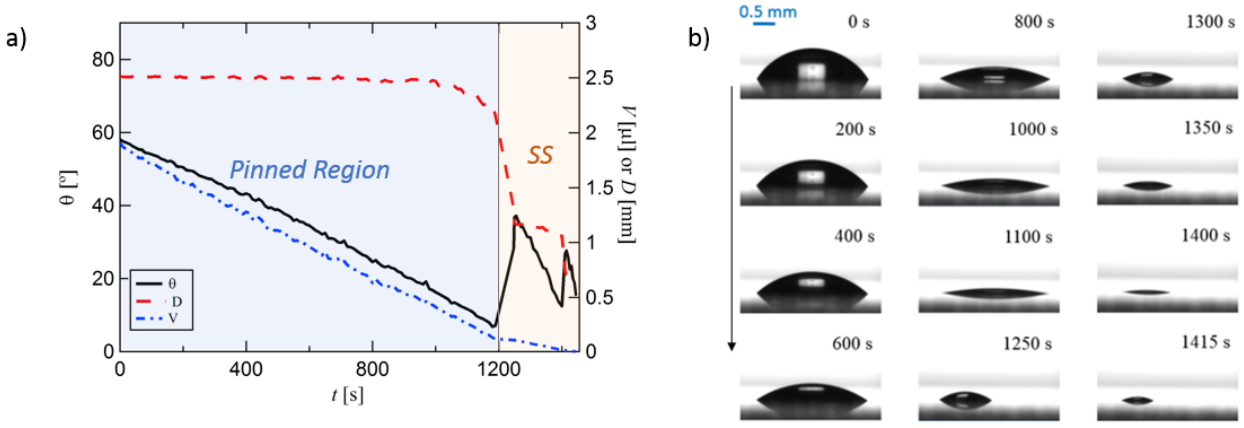

FIGURE 1.4: Evaporation of water droplet on glass slide: a) evolution of diameter, D, volume, V,and contact angle, θ, over time, t; b) successive images of side view. Adapted from [4]

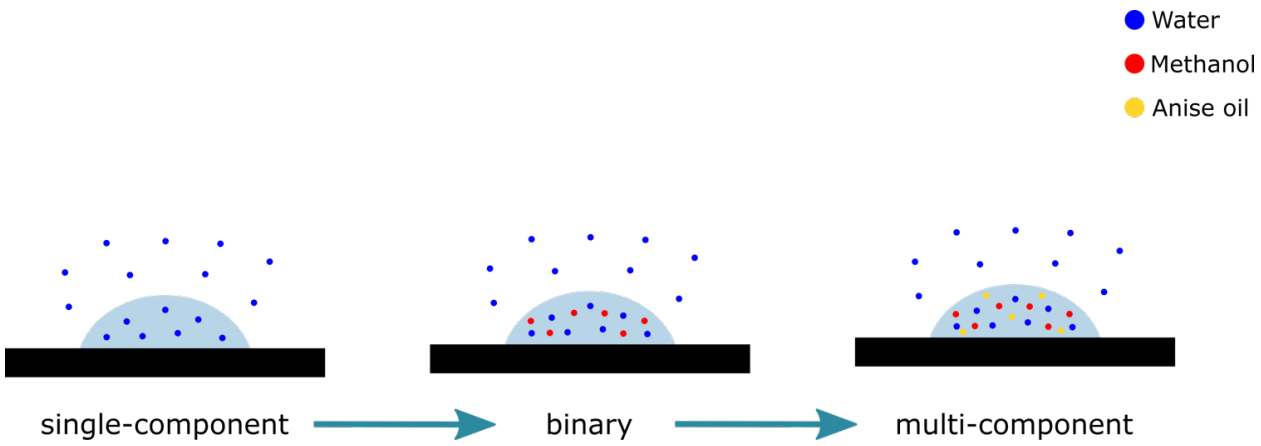

FIGURE 1.5: Schematic of a single-component, binary (two-component), and multi-component sessile droplet

1.4 Binary Droplet Evaporation

Although the effect of various parameters are extensively studied in pure liquid droplet with a single component, the physics become more complex when there are more than one component inside droplet. An example for a binary droplet could develop when methanol droplet is initially deposited on a solid substrate in a humid surrounding. Due to hygroscopic property of methanol, water vapor present in surrounding gets absorbed/adsorbed into droplet. If the substrate temperature is set to values below room temperature and also due to evaporative cooling effect, the water vapor will also condense on the droplet. In the described scenario, droplet evaporation starts as a single-component, but transforms into a binary droplet as the second components is up taken to the droplet. In some cases, there are more than two components in the droplet. For example, anise oil dissolves in methanol, but it does not dissolve in water. If a droplet of methanol and anise oil is deposited on a substrate and let evaporate in a humid environment, the water vapor will get absorbed/adsorbed and possibly condensed in the droplet. This results in a ternary droplet which consists of three components.

Evaporation of binary mixture droplet has been investigated by Sefiane et al. [75] for ethanol-water droplet. They showed that the initial contact angle of mixture droplet decreases as the concentration of ethanol increases compared to water. They also reported three different stages in evaporation of binary droplet. The first stage corresponded to evaporation of a more volatile component, i.e., methanol, and the third stage attributes to the evaporation of a less volatile component, which is water. The middle stage was a transition stage during which the contact angle experienced a rise.

The effect of relative humidity of surrounding has been studied in a comprehensive study by Chen et al. [18] where they combined three techniques of optical microscopy, infrared thermography and acoustic echography. They showed that the humidity level of surrounding has noticeable effect on behavior of ethanol droplet while it has no effect on butanol droplet due to the hygroscopic property of ethanol. Fukatani et al. [32] focused on the early stage of ethanol droplet evaporation by controlling both environment humidity and temperature. In another study, Kita et al. [50] investigated ethanol droplet evaporation under controlled humidity and temperature of surrounding by gas injection chromatography. They developed an empirical model to predict the volume of droplet over time.

Humidity of the environment is often an imposed condition that introduces some unwanted effects into the system. For example, longer evaporation times adversely effect the speed of biosensing mechanisms. Also, a droplet that takes for ever to evaporate is not desired for microfabrication or printing purposes. In the last two studies mentioned above, they tried to control and eliminate the unwanted effect of humidity by changing the temperature of surrounding. This approach requires the whole system to be inside an environmental chamber. It is evident that using an environmental chamber for real world applications is not feasible due to higher cost of these chambers as well as their size.

Sometimes it is not possible to fit the huge industrial equipment inside an environmental chamber.

In chapter 2 of this dissertation, we have proposed a low-cost and simple approach to control the unwanted humidity effect of surrounding by tuning the substrate temperature. Changing the temperature of the substrate is a straightforward and low-cost method. We investigated behavior of methanol droplet under three relative humidity of surrounding and three substrate temperature. It was observed that changing the humidity does not affect the initial evaporation rate of droplet. We have also proposed a regime map, which is a function of surrounding humidity and substrate temperature, based on behavior of droplet during evaporation.

1.5 Data-Driven and Machine Learning Techniques in Droplet Evaporation

Data-driven and machine learning techniques are used as powerful tools in analyzing a wide range of fluid mechanics problems [12, 13] such as turbulence [29, 84, 28, 31, 30], phase transition [44], ignition [64], vortex vibrations [66, 94], and aerodynamics disturbances [39]. Image processing and pattern recognition techniques have been employed to analyze the remaining stains after evaporation of sessile droplets. Analysis of patterns in dried drops of biological fluids revealed a lot of information for medical diagnostics [95, 48, 80, 15, 37]. Two different studies [49, 33] showed that the chemistry of fluid and substrate can be identified by recognition of patterns in the stains. The aforementioned studies utilize machine learning techniques to indirectly measure and detect the mechanisms inside droplet from the footprint after evaporation. Here, we introduce a data-driven approach to directly analyze the dynamics of binary droplet evaporation (induced

by transfer of a second component present in the atmosphere).

In chapters three and four of this dissertation, we have used machine learning, classification and regression, algorithms to analyze the evaporation of methanol droplet under controlled relative humidity of surrounding and substrate temperature. The relative humidity of the surrounding is estimated by both classification and regression algorithms. The regime of droplet evaporation is estimated through classification models. We have used Naïve Bayes and decision tree classifiers. It was observed that decision tree outperforms Naïve Bayes and benefits from additional features. The diameter and contact angle evolution over time are estimated with polynomial regressors (linear to fourth order) and regression tree. Although higher order polynomials showed improved accuracy for testing set, their performance deteriorated for the validation and estimation sets due to overfitting the data.

1.6 Ternary Droplet Evaporation

As the number of droplet components increase, the underlying physics of evaporation becomes more complicated. It was not until recently that the study of Tan et al. [92] on evaporation of Ouzo droplet shed some light on the complex mechanisms underlying a ternary droplet. They reported as ethanol evaporates faster than water, the solubility of the mixture for anise oil reduces. By increase in concentration of water, oil microdroplets nucleate in the droplet and create a white opaque mixture. By coalescence of oil microdroplets, an oil ring forms at the periphery of droplet.

In chapter five of this dissertation, we have examined the behavior of a ternary droplet, i.e., methanol-water-anise oil, under controlled environmental humidity and substrate temperature. We have used simultaneous infrared thermography and optical microscopy

to analyze the time evolution of droplet parameters such as diameter, volume, and contact angle, as well as hydrothermal waves. We observed that the humidity of surrounding has noticeable influence on internal flows of droplet. Tuning the substrate temperature was observed to eliminate the unwanted effects of surrounding humidity by both changing the droplet lifetime and the temperature of the liquid-gas interface.

Chapter 2

Combined Effect of Relative Humidity and Substrate Temperature on Evaporation of Methanol Droplet

This manuscript has been published by the Journal of Coatings Technology and Research.

Sahar Andalib [a] , Ali Alshehri [a,b], H. Pirouz Kavehpour [a,*]

[a] Mechanical and Aerospace Engineering Department, Henry Samueli School of Engineering and Applied Science, University of California, Los Angeles, CA 90095, USA

[b] Mechanical Engineering Department, King Fahd University of Petroleum and Minerals (KFUPM), Dhahran 31261, Saudi Arabia

[*] Corresponding Author: Phone: +1 (310)-825-6494, Fax: +1 (310)-206-4830

2.1 Abstract

Understanding and manipulating the mechanisms involved in evaporation of organic solvent droplet in humid environment are of great importance for numerous industrial and biological applications. The combined effect of substrate temperature and relative

humidity of the environment on evaporation of pure methanol droplets has been experimentally investigated. A drop shape analyzer was used to record the evolution of contact angle, base diameter, and volume of droplet. At low relative humidity, droplet experiences three stages of evaporation: constant, slightly increasing, and sharply decreasing contact angle. Substrate temperature has no effect on the qualitative behavior of droplet at low relative humidity. At high relative humidity, droplet evolution is influenced by substrate temperature. At relatively high substrate temperature, droplet undergoes two stages of evaporation where contact angle increases to a maximum then decreases until the end of evaporation. At low substrate temperature, the droplet experiences a single stage where it reaches an equilibrium state with finite volume, diameter, and contact angle. In humid environment, water vapor gets adsorbed-absorbed and/or condensed on the droplet. Decreasing substrate temperature causes the temperature at the liquid-gas interface to fall below the dew point which enhances the water condensation. Evaporation rate diminishes as the relative humidity rises and its effect is more pronounced for lower substrate temperature. Relative humidity of the surrounding seems to have a negligible effect on the initial evaporation rate which is mainly attributed to evaporation of methanol. A regime map is proposed based on different evolution of droplet under different condition of environment as well as substrate temperature. A semi-empirical model is used to predict the evolution of droplet volume over time. In all nine conditions, evaporation rate is underestimated by the model due to neglecting free convection.

2.2 Introduction

Evaporation of a liquid droplet on a solid surface is a ubiquitous phenomenon in nature as well as industries such as ink-jet printing [60, 47, 23], cooling systems [90, 83, 88],

bio-diagnostics [41, 93, 34], DNA mapping [45, 19, 27], agricultural irrigation [58, 43], and crop dusting [6]. Droplet evaporation is influenced by various factors such as the liquid/substrate properties [57, 77, 7, 21, 63, 10, 73, 87] as well as environmental conditions [76, 8, 61, 32, 50]. However the combined effect of liquid/substrate properties and surrounding condition has rarely been explored. The quality and resolution of coating techniques and ink-jet printing are highly affected by the evaporative behavior of the liquid phase. A profound study of the underlying mechanisms of droplet evaporation under different parameters provides necessary information to suitably design and precisely control systems involving droplet evaporation.

Mollaret et al. [57] studied evaporation of sessile water droplet on two different heated substrates, namely aluminum and polytetrafluoroethylene (PTFE) . Their results showed that on aluminum substrate for high temperatures the droplet stayed pinned during its lifetime and the volume decreased linearly. However at low temperatures on aluminum substrate, the volume deviated from linear trend toward the end of drop lifetime as the contact line receded. Unlike aluminum, very little effect of temperature on evaporation process for PTFE substrate was observed. Different contact angle evolution was also observed on two substrates. On aluminum substrate, contact angle decreased during pinned stage followed by a slight increase as de-pinning and then stayed constant until a sharp decrease toward the end of droplet lifetime. On the other hand, the transition in contact angle between pinned and de-pinned behavior was smooth on PTFE substrate. Sefiane [77] investigated the combined effect of surfactant concentration and substrate temperature on water droplet evaporation. While the effect of temperature was in agreement with the results of Mollaret et al. [57], adding surfactant caused the drop base to increase before reaching steady constant base regime. Furthermore, increasing surfactant concentration was found to delay the de-pinning phenomenon. In another study Sefiane and

Tadrist [74] examined the de-pinning phenomenon through three parameters: controlled environment pressure, substrate temperature, and surfactant concentration. Their results demonstrated abrupt contraction of the contact line under reduced pressures while under atmospheric pressure the de-pinning occurred smoothly. Evaporation rate was clearly enhanced by reduction in pressure. A critical temperature was found beyond which de-pinning did not happen and the droplet stayed pinned during the entire lifetime. The effect of surfactant was similar to Sefiane [77]. Even though studying single component droplet evaporation is crucial to the understanding of the mechanisms involved, multi-component droplets exist in many industrial applications such as binary refrigerants in cooling technologies.

Sefiane et al. [75] experimentally studied evaporation of water-ethanol mixture droplets. They found that behavior of binary mixture droplets differed from that of pure substances. Three distinct stages of evaporation were observed for binary mixtures. The first stage corresponded to the behavior of the more volatile liquid. The second stage was the transition stage and the third stage correlated with evolution of the less volatile component. The contact angle of the mixture sharply decreased during the first stage followed by a rise to a maximum value until it finally decreased toward the end of droplet lifetime. They also showed that the initial contact angle of the mixture was between the initial contact angle of pure substances (i.e. water and ethanol) and it dropped by increasing the ethanol concentration. Sefiane et al. [78] extended the study on binary mixtures by controlling the environmental conditions. Evolution of different concentrations of water/methanol mixture droplets were reported and analyzed under nitrogen and water saturated environments. The droplet reached an equilibrium state in the saturated environment while under nitrogen surrounding it experienced four stages of evaporation.

The maximum contact angle observed under nitrogen environment decreased by increasing the initial methanol concentration which suggested the hypothesis that methanol does not entirely evaporate at the first stage. However, initial contact angle for saturated and unsaturated surroundings was the same showing that the presence of saturated environment only affects the evaporation process not the wettability of the droplet. It should be noted that the saturated environment in this study was created by placing a water reservoir in the testing chamber and relative humidity was not measured quantitatively. In a similar work Liu et al. [55] performed a comprehensive study on evaporation of water/ethanol droplet with different mixing ratios under the environments with various relative humidity and ethanol vapor pressure. They also observed an increase in contact angle for binary droplets at any relative humidity. Nevertheless, the fast growth in contact angle suggested the possibility of water condensation on the drop. The binary droplet volume experienced a rise when evaporating in high ethanol vapor pressure environment. The increase in volume and faster reduction in contact angle at higher ethanol vapor pressure suggested that ethanol condenses onto the droplet. The results also demonstrated an acceleration in evaporation of water droplets in higher vapor pressure of ethanol present in the atmosphere. [18] used three different techniques of optical visualization, infrared thermography, and acoustic high-frequency echography to study the evaporation of butanol, ethanol, water/butanol, and water/ethanol droplets. No effect of relative humidity was observed on evaporation of pure butanol droplet. Homogeneous infrared images and constant acoustic reflection coefficient confirmed the unchanged concentration of butanol in the drop during evaporation. This is due to the low hygroscopic power of butanol. On the other hand, high hygroscopic power of ethanol resulted in noticeable effect of relative humidity on the evolution of pure ethanol droplets. At high relative humidity plot of $V^{2/3}$ could obviously be divided into two stages with

different slopes corresponding to evaporation of ethanol and that of water. Heteregeneous thermal patterns alongside evolution of acoustic reflection coefficient proved that ethanol droplet undergoes continuous water loading. Studies of butanol/water binary droplet revealed that butanol evaporated at the first stage and its exhaustion time estimated by acoustic method was in agreement with optical and infrared observations. However for ethanol/water binary droplet the exhaustion time calculated from visual and infrared techniques was considerably shorter than acoustic measurements. This suggested the presence of ethanol residuals at the bottom of the droplet and in-liquid diffusion controlled evaporation process toward the end of droplet lifetime. Furthermore, Innocenzi et al. [42] examined evaporation of ethanol and ethanol/water mixtures by time-resolved infrared spectroscopy. They reported adsorption of water by the droplet during the first stage of evaporation followed by three stages where both ethanol and water evaporate. Their observations illustrated that the evaporation of ethanol followed a monotonic trend and was not influenced by complicated water behavior.

The effect of horizontal air velocity on evaporation of methanol droplets was looked into by Bin et al. [8]. They illustrated that the larger the air velocity the higher the evaporation rate. Evaporation process consisted of three stages: constant contact angle, constant base diameter, and transition stage. They reported that the largest evaporation rate was related to the constant contact angle regime and the least evaporation rate corresponded to the constant diameter one. The rate of evaporation for transition regime was between the two values. Recently, Fukatani et al. [32] and Kita et al. [50] studied the combined effect of environmental conditions, namely ambient temperature and relative humidity on the evolution of ethanol droplet. Fukatani et al. [32] focused on the first stage of evaporation, i.e. pinned contact line. Their results indicated that self-generated thermal patterns were enhanced by increasing ambient temperature, but relative humidity seemed to have

a reverse effect. At a higher temperature, greater evaporative cooling led to greater temperature difference between the apex and the edge of the drop which was the driving force for hydrothermal waves. On the contrary, at higher relative humidity the heat of adsorption-absorption and/or condensation of water onto ethanol drops made the temperature along the interface more uniform. However, it should be noted that at higher relative humidity of the surrounding the water intake into the droplet starts from the early stages of evaporation. Considering that both concentration and distribution of water within the drop are unknown, analysis of the IR images becomes very complicated due to large difference in emissivity of ethanol and water. Kita et al. [50] used gas injection chromatography (GIC) with drop profile analysis to directly measure the amount of evaporated ethanol and loaded water. Results from gas chromatography exhibited a drop in ethanol concentration over time. Reduction in ethanol concentration was attributed to both its own evaporation as well as water intake on the drop. They concluded that at low relative humidity the main mechanism for water intake was that of adsorption-absorption though at high relative humidity water condensation play a more dominant role. Additionally, they proposed a combined evaporation-adsorption/absorption and/or condensation empirical correlation which took into account the change of ethanol concentration over time, relative humidity dependent diffusion coefficient, and water intake on the the drop.

Although numerous studies investigated the effect of liquid/substrate properties or environmental condition, none of these research works examined the coupled effect of the two categories mentioned. While in practical applications the environmental conditions are either imposed or expensive to control, manipulating the evaporation process by tuning the substrate properties would be an easier approach to compensate the environmental effects. The current work experimentally investigates the combined effect of

environmental factor (i.e. relative humidity) and substrate temperature on evaporation of methanol droplet. The experiments were performed in a chamber with controlled relative humidity. Droplet evolution was described and analyzed through its characteristic parameters such as volume, base diameter, and contact angle.

2.3 Experimental Techniques

Experiments are carried out in a temperature and humidity controlled chamber (with a dimension of $127 \times 127 \times 76\ mm^3$) of drop shape analyzer (DSA 100) from KRÜSS (Figure 3.2). The relative humidity (RH) and ambient temperature (T_{amb}) in the chamber were controlled between 20% and 80% and at 25 °C. The bottom side of the chamber was equipped with a Peltier plate with temperature control. The tested substrate temperature ($T_{substrate}$) was between 15 °C and 35 °C. The needle was fitted in the chamber through a small hole at the top side. The DSA 100 equipment was placed on an optical anti-vibration table to eliminate environmental disturbances.

Methanol was purchased from Fisher Scientific with purity of 99.8%. The glass substrates were coated with a very thin PDMS (polydimethylsiloxane) layer to achieve spherical and reproducible droplets with measurable contact angles. The temperature and relative humidity of the chamber as well as substrate temperature were set to desired values. Enough time was allowed for the chamber and substrate to achieve quasi-steady state. Drops of methanol with specified volume were deposited on the coated substrate and let evaporate under the set conditions. Evolution of the drop was recorded by DSA 100 camera at 50 frames per second. Post-processing was done with DSA Advanced software to study the time evolution of droplet contact angle (θ), base diameter (D), and volume (V). Elliptical fitting was used to compute the volume and contact angle of the droplet

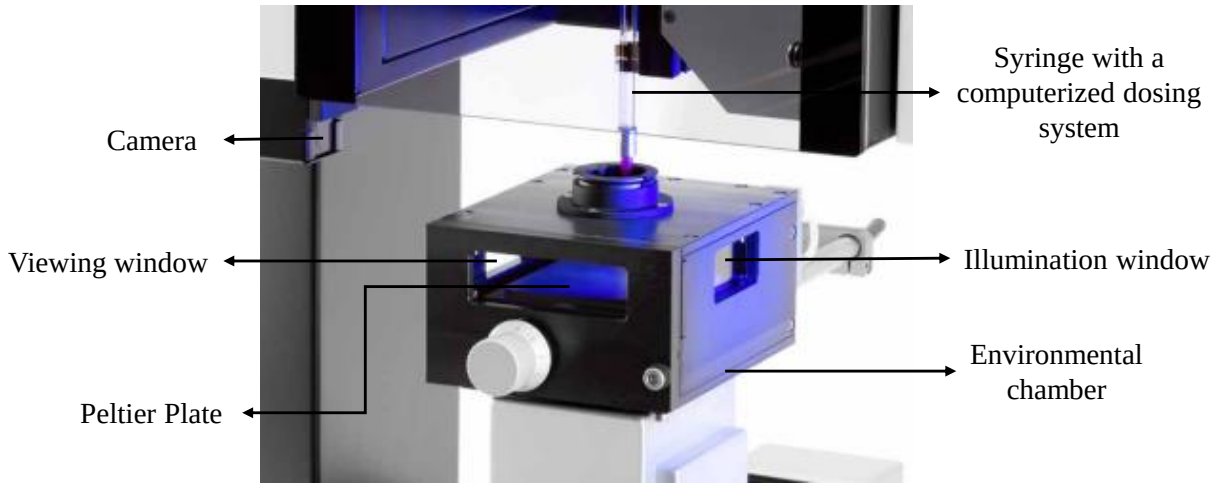

FIGURE 2.1: Droplet Shape Analyzer (DSA100) from Krüss with (1) environmental chamber; (2) controlled-volume dosing system; (3) viewing and illumination windows; (4) controlled temperature substrate (Peltier plate); and (5) adjustable x-y-z stage

due to the observed differences in right and left contact angle. In order to confirm that methanol did not interact with the coating on the substrate, multiple droplets were repeatedly deposited at the same location. No change was observed in their initial contact angle or evolution during evaporation. The deposited droplet volumes were all smaller than 10 μl in order to keep the droplet size lower than the capillary length. The corresponding volume to the capillary length for methanol is around 45 μl.All experiments were repeated five times to ensure reproducible data. Base diameter (D) and volume (V) are normalized by their initial values i.e. $D^* = D/D_0$ and $V^* = V/V_0$, while the time t is nondimensionalized by final evaporation time of the droplet $t^* = t/t_f$.

2.4 Results and Discussion

2.4.1 Droplet evolution

In what follows the experimental data on the evaporative behavior of methanol droplet on PDMS coated glass substrate is presented under different relative humidity (RH) and substrate temperature ($T_{substrate}$). Figure **??** illustrates the time evolution of contact angle (θ), non-dimensional base diameter (D^*), and dimensionless volume (V^*) for $T_{substrate}$ = 15 °C, 25 °C, and 35 °C and RH = 20%, 50%, and 80%. Plots are reported in dimensionless form to enable easier analysis of droplet behavior.

At low relative humidity (RH = 20%), evaporation methanol droplet is divided into three stages. At the first stage, contact angle stays relatively constant. This stage covers tha majority of droplet lifetime. During the second stage, the contact angle rises slightly. The third stage is where the contact angle sharply drops until the droplet disappears. Volume and base diameter continuously decrease during all three stages of evaporation. The regime of constant contact angle followed by a modest rise is also reported for pure ethanol droplets evaporating at room temperature and relative humidity of 20% [18]. Sefiane et al [78] theoretically explained that the rise in contact angle for methanol droplets can be a consequence of high evaporation rates at the triple line and its receding speed. Different values of substrate temperature have no obvious effect on the evolution of droplet qualitatively. Higher substrate temperature accelerates evaporation of the droplet (which is not illustrated in Figure **??**), however the dimensionless behavior remains the same.

Under relative humidity of 50% and substrate temperature between 15 °C and 35 °C as well as relative humidity of 80% and substrate temperature of 25 °C and 35 °C, the droplet undergoes two stages of evaporation. At the first stage, the contact angle increases

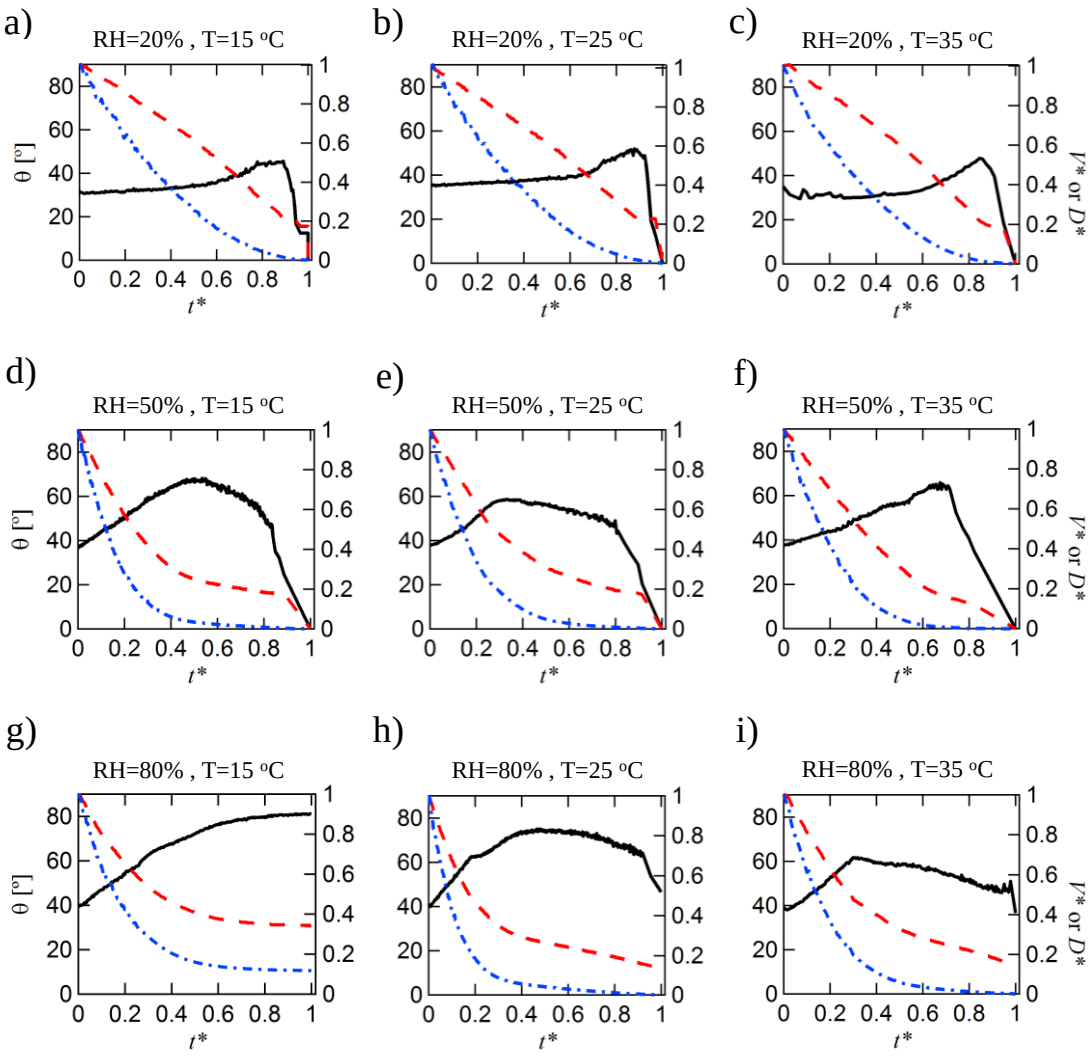

FIGURE 2.2: Time evolution of contact angle (), base diameter (), and volume () for relative humidity of 20% (a,b,c); 50% (d,e,f); 80% (g,h,i) with substrate temperatures of 15^oC (a,d,g); 25^oC (b,e,h); and 35^oC (c,f,i).

to a maximum value and at the second stage, it reduces until the end of evaporation. Since methanol is highly hygroscopic, water vapor present in the humid environment gets adsorbed-absorbed and/or condensed on the surface of pure methanol droplet. The local growth in the concentration of water at liquid-gas interface changes the interfacial tensions and results in larger contact angle [18, 50]. Initially methanol evaporates while water is continuously being added to the droplet. At the point of maximum contact angle, most of methanol has evaporated and the drop mainly consists of water. However, it is noteworthy that the contact angle of the drop is lower than the equilibrium contact angle of water on PDMS coated substrate (i.e. 105 °). This phenomenon is observed and reported in literature due to the presence of residual methanol that remains in the drop after the first stage of evaporation [78, 55]. The second stage corresponds to evaporation of water and the remaining methanol until droplet disappears. Nevertheless, it is observed that at relative humidity 80 % and substrate temperature 15 °C, the volume, contact angle, and diameter of droplet reach a plateau where no more significant change is observed in the drop profile. Similar results were observed in the work of Kita et al [50] where ethanol droplets fully evaporated at relative humidity 35% for both ambient temperature 30 °C and 40 °C while at more humid environment the drops reached to an equilibrium state with finite volume.

2.4.2 Evaporation rate

Figure 2.3a-c illustrate the time evolution of methanol droplet volume under different relative humidity and substrate temperature. Increasing substrate temperature accelerates evaporation process and reduces the final evaporation time [57, 74]. On the contrary, higher relative humidity of the surrounding results in longer evaporation time. Growth in total evaporation time through increasing relative humidity of the environment is more

pronounced for lower substrate temperature. At substrate temperature 35 °C increasing relative humidity from 20% to 80% enlarges the total evaporation time around 100% (Figure 2.3c). Whereas the same change in relative humidity at substrate temperature 25 °C results in 500% growth in droplet life time and at substrate temperature 15 °C rise in humidity of the environment causes the drop to reach an equilibrium state with surrounding (i.e. infinitely large evaporation time, Figure 2.3a-b). At lower substrate temperature, the temperature of the liquid-gas interface can drop below the dew point and water vapor from the environment condenses on the droplet in addition to the amount getting adsorbed-absorbed by diffusion. At higher substrate temperature, the liquid-gas interface temperature remains above the dew point. Hence, rise in humidity of the surrounding only increases the amount of water being adsorbed-absorbed on the drop. Interfacial temperature distribution of organic solvent droplets evaporating in humid environment has been thoroughly investigated with the aid of infrared camera by Fukatani et al [32] and [18]. However, due to complex nature of the problem, continuous addition of water on the drop, its unknown concentration and distribution, huge difference in emissivity of water and organic solvent, it accurately measuring the temperature at the liquid-gas interface would be difficult.

The initial evaporation rate of droplet is calculated and demonstrated versus substrate temperature for different relative humidity of the environment in Figure 2.3d. It is observed that increasing substrate temperature results in higher initial evaporation rate for all relative humidity of the environment. On the other hand, change in relative humidity does not effect the initial evaporation rate noticeably. The initial stage of evaporation is mainly attributed to evaporation of methanol and the diffusion coefficient of methanol in dry air and that of methanol into humid air is found to differ by less than 1% [32]. This is further shown in the empirical model proposed by Kita el al [50] that the change in

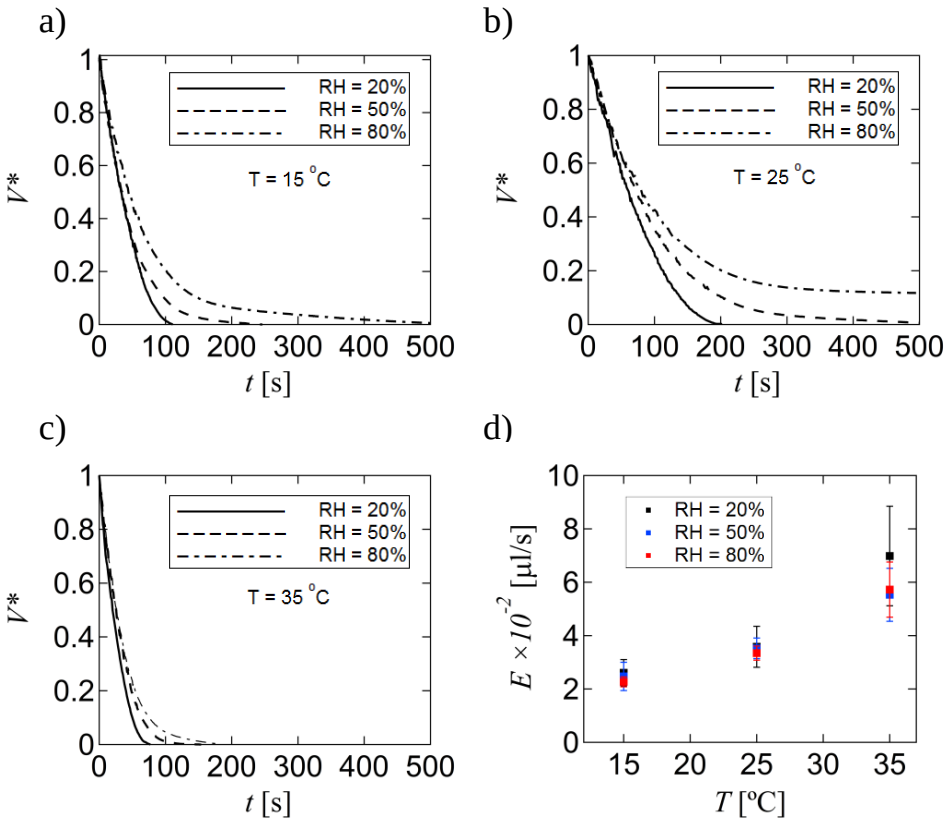

FIGURE 2.3: Time evolution of volume during evaporation of droplets at substrate temperatures of 15^{o}C (a); 25^{o}C (b); and 35^{o}C (c) at relative humidity of 20% (), 50% (), and 80% (). (d) initial evaporation rate calculated as rate of change of volume with respect of time at the beginning of evaporation.

diffusion coefficient of volatile component into dry air versus humid air is negligible.

2.4.3 Regime map

Dimensionless plots of droplet evolution enables easier analysis of its behavior under different conditions. Three different behavior of droplet were observed under the tested values for relative humidity of surrounding and substrate temperature. Therefore a regime map is proposed to classify the evaporative behavior of droplet as shown in Figure 2.4. It

is worth noting that the regime map is solely proposed to illustrate different behaviors observed during droplet evaporation. The boundaries in the regime map are roughly drawn and simply based on the experimental results and analysis of the mechanisms involved. More data points are needed in order to sketch a more accurate regime map as well as its boundaries. At low relative humidity (squares in regime map in Figure 2.4) droplet undergoes three stages of evaporation, namely constant, slightly rising, and sharply decaying contact angle. The substrate temperature has no effect on the qualitative behavior of the drop. The adsorption-absorption and/or condensation of water is negligible on the drop due to its low vapor pressure in the surrounding.

At higher relative humidity, substrate temperature influences the evaporative behavior of droplet. For both high relative humidity and substrate temperature (triangles in regime map in Figure 2.4), droplet experiences two stages of evaporation: a region of increasing contact angle followed by its reduction until the end of drop lifetime while the volume and base diameter decrease monotonically. At high relative humidity when substrate temperature is low enough (circle in regime map in Figure 2.4), the droplet evolution consists of only a single step. The contact angle rises monotonically while volume and diameter decrease continuously until all three parameters reach a plateau. When relative humidity is high, organic solvent drop absorbs a non-negligible amount of water during evaporation [18, 42, 50]. Figure 2.4 includes the dew point temperature for each value of the surrounding relative humidity. Water uptake on the drop is through adsorption-absorption and/or condensation. When substrate temperature is low enough so that the temperature at the liquid-gas interface falls below the dew point at that relative humidity, condensation becomes the dominant mechanism for water uptake on the drop. At higher substrate temperature, since the liquid-gas interface temperature stays above the dew point, water is loaded to the drop mainly by adsorption-absorption. Hence,

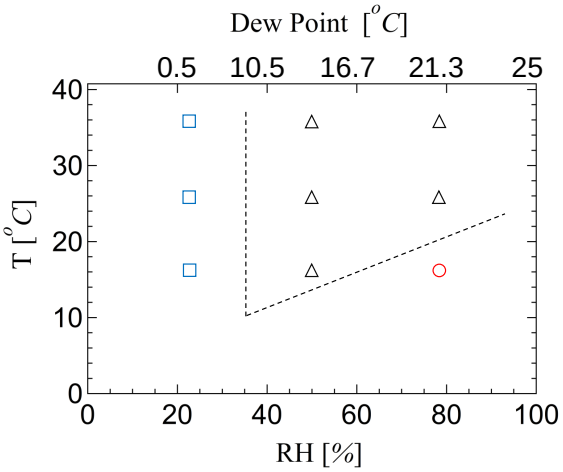

FIGURE 2.4: Relative humidity and substrate temperature regime map of droplet evaporation showing distinct droplet behavior regions

higher relative humidity of the environment increases the amount of water adsorbed-absorbed on the drop but does not change the behavior of the droplet considerably. It is worth noting that the time span that contact angle stays at values close to the maximum point seems to vary for different conditions. This needs further investigation of the droplet behavior using more experimental data.

2.5 Conclusion

An experimental investigation is carried out to study the combined effect of substrate temperature and relative humidity of the environment on evaporation of pure methanol droplet. Experiments were performed in an environmental chamber with controlled relative humidity and at room temperature of 25 °C. The substrate temperature was also controlled with the aid of a Peltier plate.

At low relative humidity of the surrounding, droplet undergoes three stages of evaporation: constant, slightly increasing, and sharply decreasing contact angle while volume

and diameter drop continuously. No significant effect of substrate temperature was noticed on the qualitative behavior of droplet during evaporation at low relative humidity. At high relative humidity, substrate temperature plays a role on the evolution of droplet. At high temperature, droplet experiences two stages of evaporation. The contact angle rises to a maximum value while both volume and diameter decrease, then it drops until the end of droplet lifetime. If the substrate temperature is low enough, the drop undergoes a single stage of evaporation where contact angle, volume, and diameter reach plateau and droplet stops evaporating. Water vapor present in humid environment gets adsorbed-absorbed and/or condensed on the droplet. Changing the substrate temperature affects the temperature at the liquid-gas interface. If the temperature at the liquid-gas interface drops below the dew point at that specific relative humidity, the condensation of water takes place in addition to adsorption-absorption of water. This will result in more water uptake on the droplet and will change its evolution. The maximum value of contact angle during evaporation is lower than that of pure water which confirms the presence of residual methanol in the drop after the first stage of evaporation. Evaporation rate enhances by increasing substrate temperature and reduces by rising the relative humidity. The enhancement in total evaporation time with increase in relative humidity is more pronounced for lower substrate temperature. This is due to the lower dew point temperature at higher relative humidity as well as lower liquid-gas interface temperature which augments the condensation of water on the droplet. The initial evaporation rate is found to be independent of relative humidity of surrounding. A regime map was suggested based on different evolution of droplet under different conditions of surrounding and substrate.

In conclusion, what has been presented in the current work suggests that the unwanted environmental effects on droplet evaporation can be alleviated and controlled

by tuning the temperature of the substrate. The idea can be applied to any industrial application involving droplet evaporation such as ink-jet printing, fabrication techniques, etc. It is worth mentioning that changing the substrate temperature is more practical and economical than changing the ambient temperature.

Chapter 3

Machine Learning Application in Prediction of Environmental Condition through Evaporation of a Liquid Droplet

This manuscript is in preparation for submission.

Sahar Andalib [a,*] , Kunihiko Taira [a], H. Pirouz Kavehpour [a]

[a] Department of Mechanical and Aerospace Engineering, University of California, Los Angeles, CA 90095

* Corresponding Author: email sandalib@ucla.edu

3.1 Abstract

Droplet evaporation is important in many industrial and biological applications such as spray cooling, ink-jet printing, microfabrication, and biosensors. Droplet behavior during evaporation is highly influenced by relative humidity of surrounding. In the present study, a classification problem is solved to reversely detect the relative humidity of the environment by analyzing methanol droplet evaporation under controlled environment.

Two different linear classifiers, Naive Bayes and Bagged Decision Tree, have been trained by three different models. Testing and validation show that Bagged Decision Tree outperforms Naive Bayes for all models. Adding extra information as input variables significantly improves the accuracy of Bagged Decision Tree while it has no net effect on the overall performance of Naive Bayes. The influence of input data distribution on target variable is also investigated. Performance of Bagged Decision Tree Classifier is not dependent on input data distribution, whereas some models of Naive Bayes seem to change their accuracy as input data distribution changes.

3.2 Introduction

Droplet evaporation is an omnipresent phenomenon in nature as well as industries such as spray cooling [83, 88], ink-jet printing [60, 47, 23], microfabrication, dye painting, agricultural irrigation [58, 43], bio-diagnostics, and biosensors [41, 93, 34]. Liquid/substrate properties [57, 77, 7, 21, 63, 10, 73, 87] as well as environmental conditions [76, 8, 61, 32, 50, 1] are among factors influencing droplet evaporation.

Noticeable change in evolution of droplet by relative humidity of the surrounding [1, 50] suggests the opportunity to reversely detect the humidity of the environment. At all temperatures and pressures, relative humidity is defined by the ratio of water vapor pressure to the saturation water vapor pressure at the temperature of the gas [59]. Hygrometer is a humidity sensing device that functions based on measurements of a parameter such as temperature, mass, etc in a substance as the moisture gets absorbed. One of the most precise humidity sensors is chilled mirror which requires frequent cleaning and skilled operator. On the other hand, some sensors like capacitive, resistive ,or thermal that are cost-effective and require small space have lower accuracy. Measuring humidity is still

a challenging task with a trade-off between accuracy and convenience. Hence, it would beneficial to explore new different methods for measuring humidity.

Application of machine learning algorithms has recently gained increasing attention in the field of droplet evaporation and deposition. Junior et al. [46] proposed a new method based on machine learning techniques (Artificial Neural Network and Regression Tree) to efficiently predict the deposition configuration of drops containing plant protection products in agricultural irrigation and spraying systems. They showed that their method is a more practical approach where the high computational cost is an issue. Gorr et al. [33] employed supervised and unsupervised machine learning algorithms as a pattern recognition technique to detect various solution composition after droplet evaporation. Recently, Hamadeh et al. [37] have analyzed dried patterns from blood droplets by machine learning in order to differentiate between patterns in droplet stains with and without exercise-induced changes in blood chemistry. They have applied Principal Component Analysis (PCA) [26] for dimensionality reduction as an unsupervised learning method and Linear Discriminant Analysis (LDA) [9] as a supervised learning approach. Even though, machine learning methods have been used in droplet stain pattern recognition or its deposition, these methods are not yet applied on analyzing the behavior of droplet during evaporation which is a dynamic process. In the present work, machine learning classification algorithms are employed to analyze the dynamic evolution of droplet while evaporating. An inverse detection method is proposed for sensing the relative humidity of the environment. The experimental data on evolution of methanol droplet under controlled humidity of environment is used to train two different machine learning classification algorithms: Naive Bayes and Bagged Decision Tree. Details of the experimental work is briefly discussed in section II and can be found comprehensively in Andalib et al. [1]. Section III discusses the two classifiers used and elaborates on data

processing and correlation between features. Section IV further talks about building the models, accuracy of the models while testing and importance of each feature to make predictions. Finally, section V explains validation of the model, effect of input variables, and input data distribution on the performance of both algorithms.

3.3 Experimental Data

The data used in this work is from our recent study [1] where the combined effect of relative humidity of the surrounding and substrate temperature was experimentally investigated on evaporation of methanol droplets.

Experiments were carried out in a temperature and humidity controlled chamber (with a dimension of $127 \times 127 \times 76\ mm^3$) of drop shape analyzer (DSA 100) from KRÜSS (Figure 3.1.b). The relative humidity (RH) and ambient temperature (T_{amb}) in the chamber were controlled between 20% and 80% and at 25 °C. The bottom side of the chamber was equipped with a Peltier plate with temperature control. The tested substrate temperature ($T_{substrate}$) was between 15 °C and 35 °C.

Methanol was purchased from Fisher Scientific with purity of 99.8%. The glass substrates were coated with a very thin PDMS (polydimethylsiloxane) layer to achieve spherical and reproducible droplets with measurable contact angles. Evolution of the drop was recorded by DSA 100 camera at 50 frames per second. Post-processing was done with DSA Advanced software to study the time evolution of droplet contact angle (θ), base diameter (D), and volume (V). Elliptical fitting was used to compute the volume and contact angle of the droplet due to the observed differences in right and left contact angle. Figure 3.2 shows experimental results for three different relative humidities and three different substrate temperatures. Base diameter (D) and volume (V) are normalized

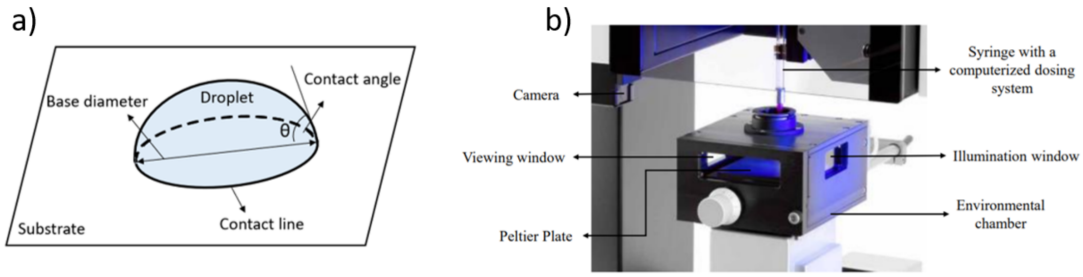

FIGURE 3.1: a: Schematic of a droplet on a solid surface; b: image of the experimental set up including environmental chamber and dosing system; reprinted from Andalib et al. [1]

by their initial values i.e. $D^* = D/D_0$ and $V^* = V/V_0$, while the time t is nondimensionalized by final evaporation time of the droplet $t^* = t/t_f$.

3.4 Machine Learning and Data processing

3.4.1 Methodology

We are solving a classification problem. Two classifiers are used: Naive Bayes [16, 51, 52, 53] and Bagged Decision Tree [91, 72, 67]. Each has its own pros and cons. Naive Bayes is a simple algorithm. Therefore it is easy to interpret it and explain to others. With simple algorithm also there is less chance for overfitting. It is faster to work with Naive Bayes and it needs smaller memory footprint. However Naive Bayes has lower accuracy. It has restrictive underlying assumptions which makes its use in real cases with compromised accuracy. Bagged Decision Tree is one of the most complicated classification algorithms. It has a built-in support for cross validation and a specialized function to measure feature importance. Nonetheless, it usually results in complex models that are not very transparent. It is often hard to understand what the Decision Tree algorithm is up to and how it is making predictions.

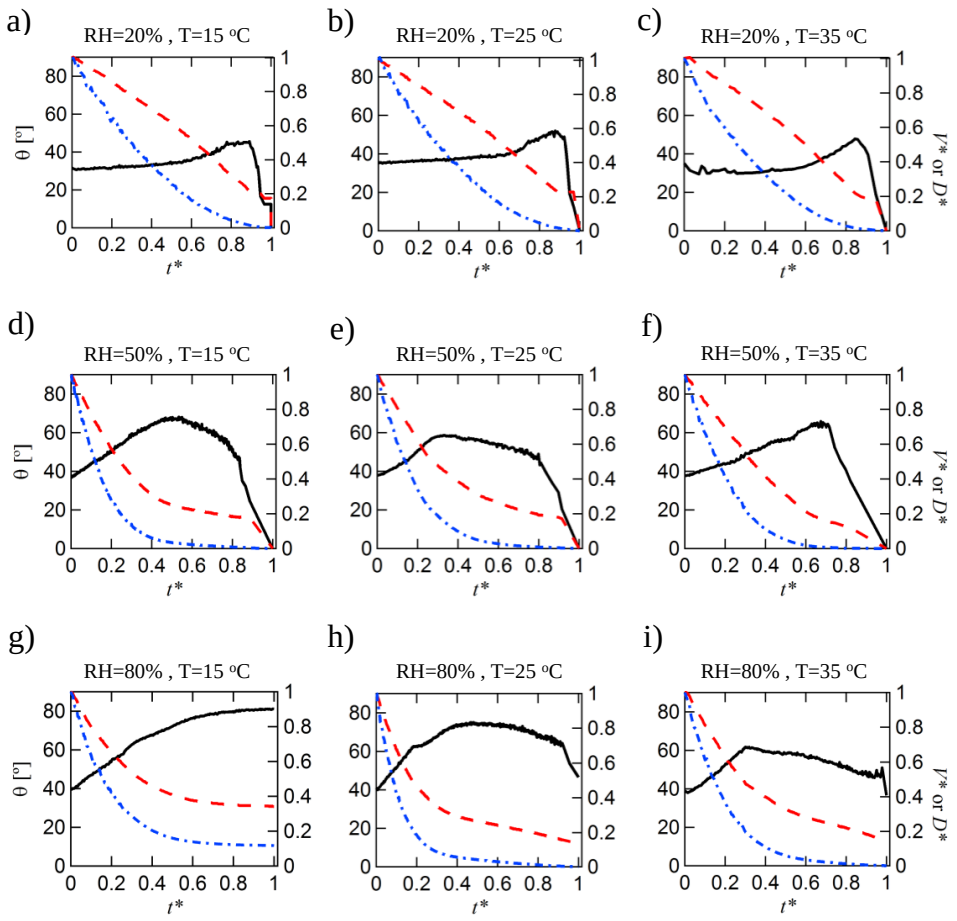

FIGURE 3.2: Experimental data on evolution of methanol: contact angle (–), base diameter (–), and volume (–)reprinted from Andalib et al. [1]

TABLE 3.1: Class and features for the classification problem

Class (target variable)	Features (input variables)					
RH (%)	T ($^\circ C$)	θ	t	D	V	Runs
20	15	...	...	...	...	10
50	23	...	...	...	...	5
80	35	...	...	...	...	5

3.4.2 Data Selection and Models

Classification is a predictive modeling approach using discrete classes. Classes are what we are trying to predict and features are the data that we use to make predictions. In the current problem, there is only one class (or target variable) which is relative humidity and the features (or input variables) are temperature, contact angle, time, diameter, and volume either in dimensionless or dimensional form. The total number of data points is 10,890 which come from a total of 60 experiments. It should be noted that there are more experimental data (i.e. runs) with RH = 20% compared to other two cases (Table 3.1). Three different models are built based on input variables. As shown in Table 3.2, model a includes only two variables (i.e. dimensionless mean contact angle and time), model b has four input variables (mean contact angle, time, temperature, and diameter all in dimensionless form), and model c has consists of the same variables as model b, but all in dimensional form. Model a is built so that it only includes information about the most important features (i.e. contact angle over time). Model b is built in order to examine whether adding extra information to the variables in model a further improves the performance. Model c tests if dimensionality of variables has an effect on performance of the classifier.

TABLE 3.2: Description of models

	Input variables
Model a	θ^*, t^*
Model b	θ^*, t^*, T^*, D^*
Model c	θ, t, T, D

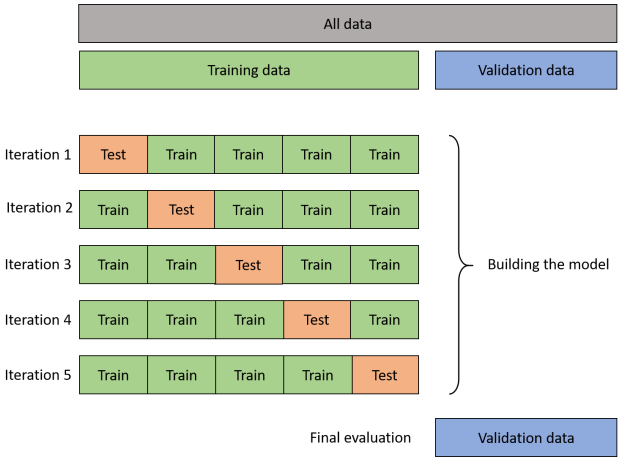

FIGURE 3.3: Schematic of data partitioning

3.4.3 Data Partitioning

As demonstrated in Figure 3.3, the data is partitioned into a training set and a validation set. The machine does not see the data in the validation set during training. When building the model, the training data is further separated into multiple subgroups of training and test sets (i.e. cross validation). This process will be explained later in section IV. The final model is trained on all available data in the training set.

3.4.4 Correlation Between Features

One of the underlying assumptions of Naive Bayes Classifier is that the features are independent. In order to check whether our data fulfills this assumption we use covariance matrix. Covariance matrix is a symmetrical matrix which shows the correlation between

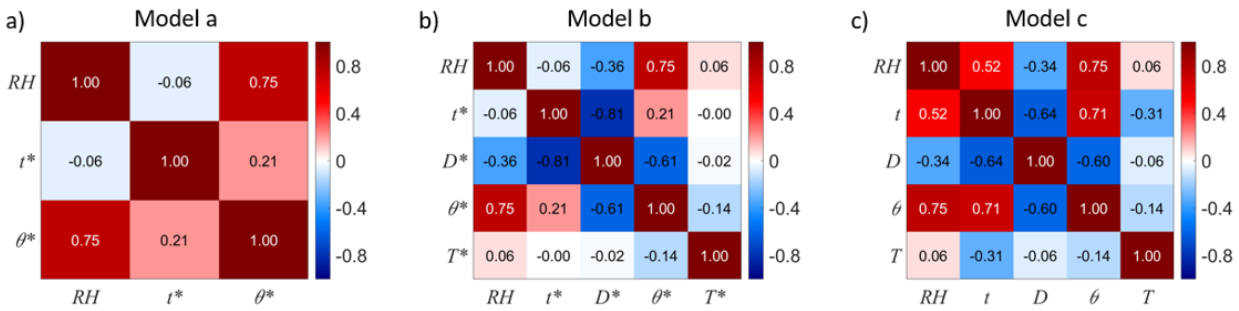

FIGURE 3.4: Covariance matrices for three different models: a) model a that includes only contact angle and time both in dimensionless form; b) model b which has contact angle, time, temperature, and diameter all in dimensionless form; c) model c that has the same variables as model b but all in dimensional form.

features as well as the class. Figure 3.4 illustrates the covariance matrix for three models. All the boxes on the diagonal have the correlation of unity because it shows the correlation of a variable with itself. Aside from that, strong correlation is observed between the mean contact angle (θ^* or θ) and relative humidity. Furthermore, the independence assumption of features are not fully satisfied as some features are correlated to each other for example time and contact angle. Nevertheless, sometimes Naive Bayes Classifier produces relatively accurate results even if this assumption is not satisfied for all features.

3.5 Estimation Results

3.5.1 Naive Bayes

After setting aside 2% of the entire data for validation, the remaining data records are randomly divided into a training set (80%) and a test set (20%) by 'Holdout' method [68, 20]. The performance of the algorithm in predicting the relative humidity value in the test set is illustrated using confusion matrices (see Figure 3.5). The vertical axes on confusion matrices represent the true relative humidity while the horizontal axes show

the predicted relative humidity values. The numbers on the diagonal of the confusion matrix represent the number of instances that are correctly predicted by the machine. The off-diagonal numbers show the incorrect predictions. For example, in Figure 3.5.a the top middle box that has a value of 54 shows that 54 data points that had an actual RH of 20% were predicted as RH of 50%. The overall error of a model is calculated from its confusion matrix defined as:

$$\text{Error} = 1 - \frac{\text{trace (confusion matrix)}}{\text{sum (confusion matrix)}} \tag{3.1}$$

It is seen that different models do not change the accuracy of Naive Bayes significantly (see Figure 3.5.a,b, and c).

Cross Validation

When the data is randomly partitioned into a training and test set, there might be a chance that some potential anomalies in the data would go either to the training or test set. To check this possibility and ensure that there are no anomalies in the data set a method called K-fold cross validation is used [82]. In this method, the data is separated into K subgroups (Figure 3.3). The training and testing the model is performed K times and each time one of the K subgroups is selected as the test set. At the end, the training error for each of K fold is reported. K-fold cross validation gives the opportunity for all the data to be in the test set at least once. We have applied 10-fold cross validation on all three models. Table 3.3 lists the average test error for all folds plus the standard deviation.

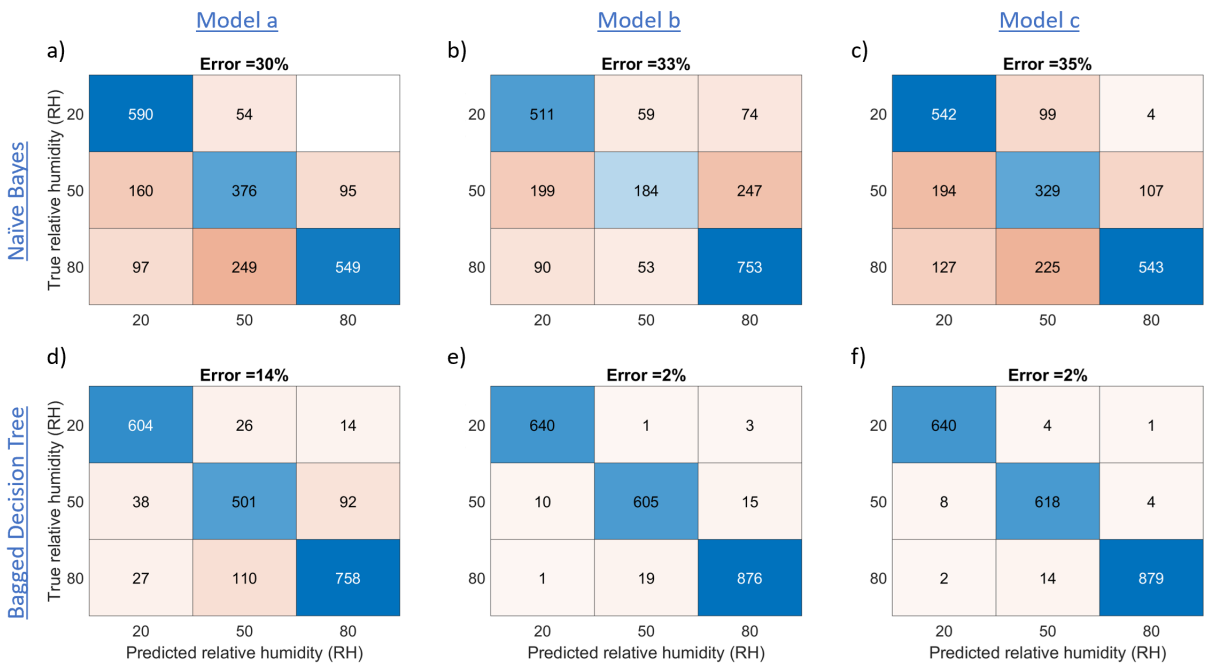

FIGURE 3.5: Confusion matrices with Naive Bayes (a,b,c) and Bagged Decision Tree algorithms (d,e,f) for three models: model a that includes contact angle and time as input variables, both in dimensionless form; model b which consists of contact angle, time, temperature, and diameter as input variables, all in dimensionless form; and model c which has the same input variables as model b, but all in dimensional form.

TABLE 3.3: Average test error (plus standard deviation) with 10-fold cross validation for different models

model a error (%)	model b error (%)	model c error (%)
$31(\pm 2)$	$35(\pm 2)$	$34(\pm 2)$

TABLE 3.4: Results of Sequential Feature Selection for Naive Bayes Classifier

Dimensionless input variables: t*, V*, D*, θ^*, T*		Dimensional input variables: t, V, D, θ,T	
Added variables	Error(%)	Added variables	Error(%)
θ^*	32	θ	32
T*	30	T	30
t*	29		

Forward Feature Selection

It is important to see which input variables (or features) are more important in making predictions. Even though, relying on the physics of the problem one can see that contact angle is the most dominant parameter, it is still beneficial to examine and see which features are statistically important to the machine. In order to do so, we use a sequential (or forward) feature selection algorithm [36, 70, 79]. Through this algorithm, the machine selects a subset of features that best predict the target variable until there is no statistically significant improvement on prediction results. The first feature added is the most important one. We have performed Sequential (Forward) Feature Selection for Naive Bayes Classifier with two sets of input variables: dimensionless and dimensional. As seen in Table 3.4 for dimensionless input variables, dimensionless contact angle (θ^*) is added first and resulted in error of 32%. Dimensionless temperature (T*) is added second and dimensionless time (t*) is added third to further reduce the error to 30% and 29%, respectively. It is noteworthy that forward feature selection stops after adding t* for dimensionless input variables. This means that adding dimensionless diameter (D*) or dimensionless volume (V*) does not improve the accuracy of Naive Bayes. For the case of dimensional input variables, this process stops only after adding contact angle (θ) and temperature (T).

3.5.2 Bagged Decision Tree

While Naive Bayes is one of the simplest classification algorithms, Bagged Decision Tree is one of the most complicated ones. It constructs n classification trees by bootstrap sampling of the data to combine their predictions for a final meta-prediction [91, 72, 67]. We have used 250 trees for our Bagged Decision Tree Classifier. When using Bagged Decision Tree, there is no need to further partition the data into training and test sets as the algorithm does that automatically. It also has a built-in support for cross validation. Although training and test sets are not required for this algorithm, to test the model we separate it into a training and test sets to obtain the confusion matrices illustrated in the second row of Figure 3.5. It is clear that models b and c produce more accurate results than model a. The reason is that models b and c include extra information on diameter and temperature. Therefore, Bagged Decision Tree makes use of this extra information to make better predictions despite Naive Bayes. It is also evident that Bagged Decision Tree outperforms Naive Bayes for every model (compare second vs. first row of Figure 3.5). This result is expected since Bagged Decision Tree is a more powerful tool than Naive Bayes.

Feature Importance

Importance of different features can be visualized for Bagged Decision Tree by out of bag feature importance [97] (see Figure 3.6). The values assigned to each feature in different models is the increase in mean square error (MSE) averaged over all trees and divided by standard deviation taken over the trees. The larger this value, the more important the feature [11]. It can be observed for all models that contact angle (either in dimensionless or dimensional form) has the highest feature importance value.

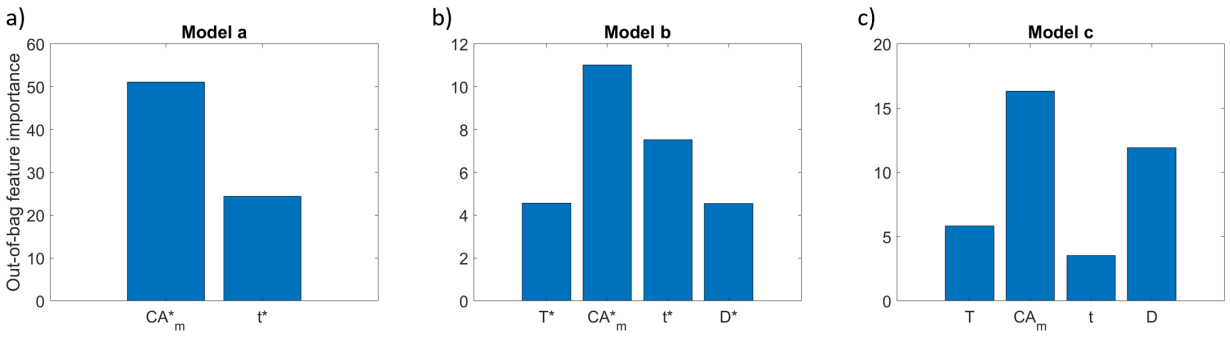

FIGURE 3.6: Out of bag feature importance for Bagged Decision Tree feature with three different models

3.6 Validating the Model

Once the machine is trained and tested, it is time to validate its performance by the data not seen by the machine before. Figure 3.7 summarizes the validation error with three models for both Naive Bayes and Bagged Decision Tree Classifiers. The vertical axes on the plots show the error vs relative humidity plotted on horizontal axes, while different colors correspond to different temperatures. Validation results show that Bagged Decision Tree outperforms Naive Bayes for all models specially for models b and c which is in agreement with the results of the training and testing. The error values are also listed in Table 3.5.

In order to obtain some insight on how the model works, it is beneficial to look at a single experiment and see how the model predicts its relative humidity value through the data points over time. Figure 3.8 illustrates the relative humidity prediction using model a. It is noteworthy that model a only includes dimensionless contact angle and time as input variables. Each row of Figure 3.8 represents a single experiment. Three sample experiments with constant RH of 20% (first row), 50% (second row), and 80% (third row) are shown. This means that there is only one true RH value for each row of the Figure that we are going to predict. Figure 3.8.a, b, and c illustrate prediction plots by Bagged Decision

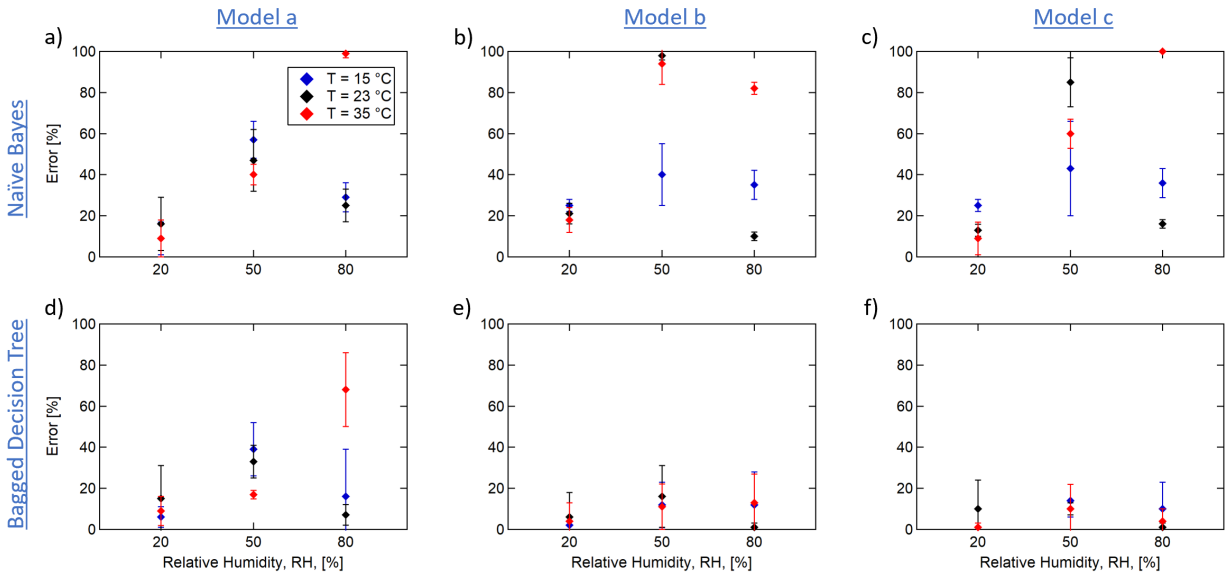

FIGURE 3.7: Validation error plots for Navie Bayes (a,b,c) and Bagged Decision Tree algorithm (d,e,f) with three models. Error values are listed in Table 3.5

TABLE 3.5: Validation error values (plotted in Figure 3.7)

		Naive Bayes			Bagged Decision Tree		
RH(%)	T(°C)	Model a	Model b	Model c	Model a	Model b	Model c
20	15	9(±8)	25(±3)	25(±3)	6(±5)	2(±2)	1(±2)
20	23	16(±13)	21(±5)	13(±5)	15(±16)	6(±12)	10(±14)
20	35	9(±9)	18(±6)	9(±8)	9(±7)	4(±9)	1(±2)
50	15	57(±9)	40(±15)	43(±23)	39(±13)	12(±11)	14(±8)
50	23	47(±15)	98(±2)	85(±12)	33(±8)	16(±15)	10(±3)
50	35	40(±5)	94(±10)	60(±7)	17(±2)	11(±11)	10(±12)
80	15	29(±7)	35(±7)	36(±7)	16(±23)	12(±16)	10(±13)
80	23	25(±8)	10(±2)	16(±2)	7(±5)	1(±2)	1(±2)
80	35	99(±2)	82(±3)	100(±0)	68(±18)	13(±14)	4(±6)

Tree and Figure 3.8.d, e, and f demonstrate prediction plots using Naive Bayes. Figure 3.8.g, h, and i represent the experimental data on time evolution of contact angle for each experiment. The green markers are the points in each experiment whose RH value is predicted correctly and the red markers are incorrectly guessed. For example in the first row, the relative humidity is 20% (as written on the title of the experiment **RH20**T15run4), therefore the correct predicted RH for both Naive Bayes and Bagged Decision Tree should be 20% (shown by green markers). This value is 50% and 80% for the second and third row of the Figure, respectively.

The shaded regions in Figure 3.8.g, h, and i correspond to the prediction of data points by Naive Bayes. The green shaded region shows the range that Naive Bayes predicts relative humidity correctly and the red shaded region represents the range whose relative humidity is predicted incorrectly. If we look closely at the values of dimensionless contact angle in shaded plots, it becomes clear that Naive Bayes makes predictions by defining threshold values for contact angle. It should be noted that model a only takes dimensionless contact angle and time as inputs. Whenever the θ^* is below 0.5, relative humidity is predicted as 20%. Anytime θ^* is above 0.7, the machine labels the data point as RH of 80%. Any value between 0.5 and 0.7 is classified as RH of 50%. For RH20T15run4, most of the contact angle values are below 0.5 except a few data points that show slightly increased contact angle (although the red region does not cover at the range with higher contact angle). For RH50T35run3, the green region is when the contact angle goes beyond 0.5. Finally for RH80T35run4, the model can barely detect the value of relative humidity of 80% except one point which exceeds a threshold value of 0.7 at around t* of 0.3. Despite Naive Bayes, it is not very transparent how Bagged Decision Tree makes predictions. No obvious trend is found by observing the experimental data and the predictions made by Bagged Decision Tree. However it is performing much better than Naive Bayes as it is

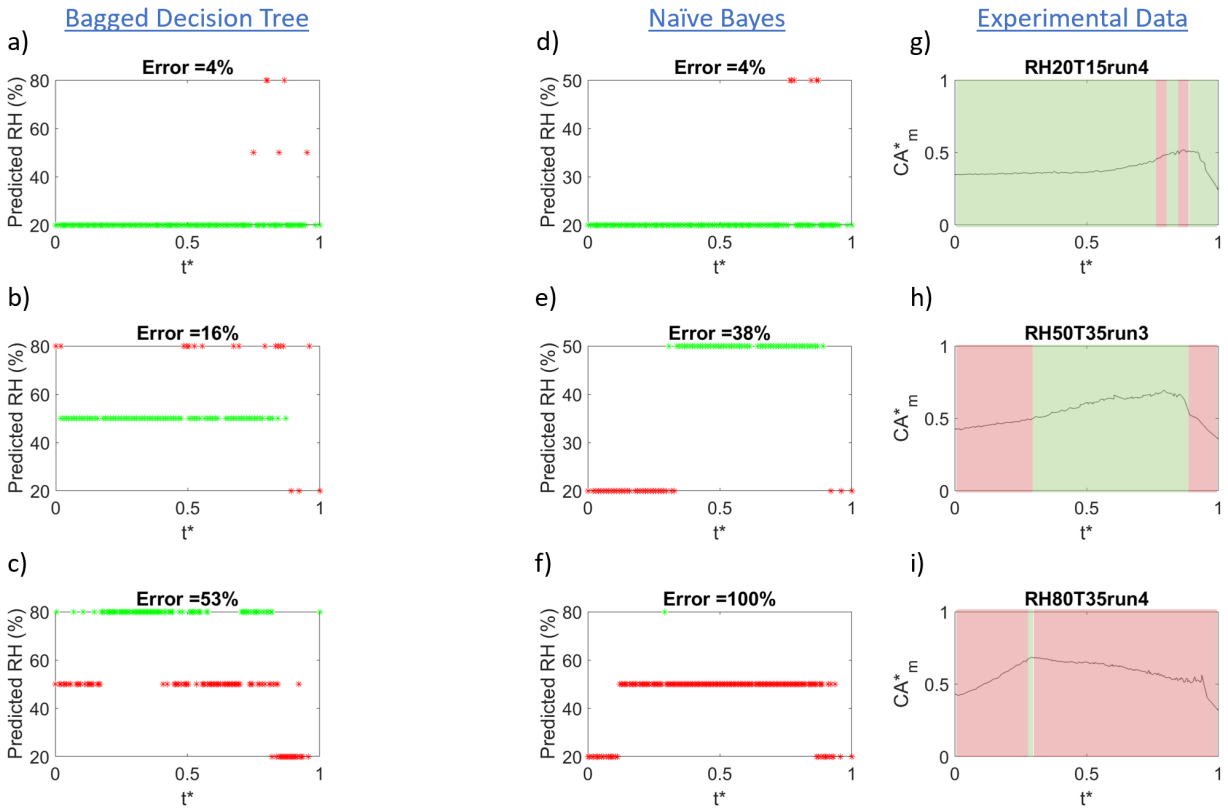

FIGURE 3.8: Relative humidity prediction over time with model a with Bagged Decision Tree (a,b,c); Naive Bayes (d,e,f); and experimental data on time evolution of contact angle (g,h,i). Each row of the Figure corresponds to a single experiment: RH = 20% (first row), RH = 50% (second row), and RH = 80% (third row).

making a better use of the input features.

3.6.1 Effect of Input Variables

The difference between models is in the input variables or features. Since performance of model b and c are relatively similar, the comparison will be made between model a and b, only. As illustrated in Figure 3.7, for Bagged Decision Tree model b results in more accurate predictions for all RHs. The reason is the same as in the testing stage. By adding to the number of input variables in model b, Bagged Decision Tree makes use of extra

information to make better predictions. For Naive Bayes (first row of Figure 3.7) going from model a to model b does not affect RH of 20% while influencing RH of 50% and 80%. The error for RH of 50% increases in model b for temperatures of 23°C and 35°C and decreases for RH of 80% at temperatures of 23°C and 35°C. Hence, adding extra information on diameter and temperature in model b does not have a net effect on overall performance of Naive Bayes Classifier. This is consistent with results of Forward Feature Selection.

3.6.2 Effect of Data Distribution

As mentioned earlier in section III.B, our experimental data is not uniformly distributed on relative humidity values. The size of data with RH of 20% is double the size for RH 50% and 80%. In order to examine whether the input data distribution affects the performance of the classifiers, another set of training, testing, and validating steps are performed by only including the same number of experimental runs for all relative humidities (i.e. only 5 runs are considered for RH = 20%). The validation results are illustrated in Figure 3.9 and the values are listed in Table 3.6. If we compare these plots with the ones in Figure 3.7, it becomes clear that input data distribution does not have a noticeable impact on Bagged Decision Tree with any model. This is attributed to the nature of Bagged Decision Tree algorithm where it builds a more robust model which is less dependent on data distribution. Models b and c of Naive Bayes are also intact by changing input data distribution. However, accuracy of model a has changed noticeably for RH of 20% and 50%. Figure 3.10 compares the performance of model a on two sample experiments for RH = 20% (first row) and RH = 50% (second row) with distribution of data as is and uniform distribution. It can be observed that Naive Bayes error increases for RH = 20% (4% to 30%) and decreases for RH = 50% (38% to 2%). This is due to the change in threshold

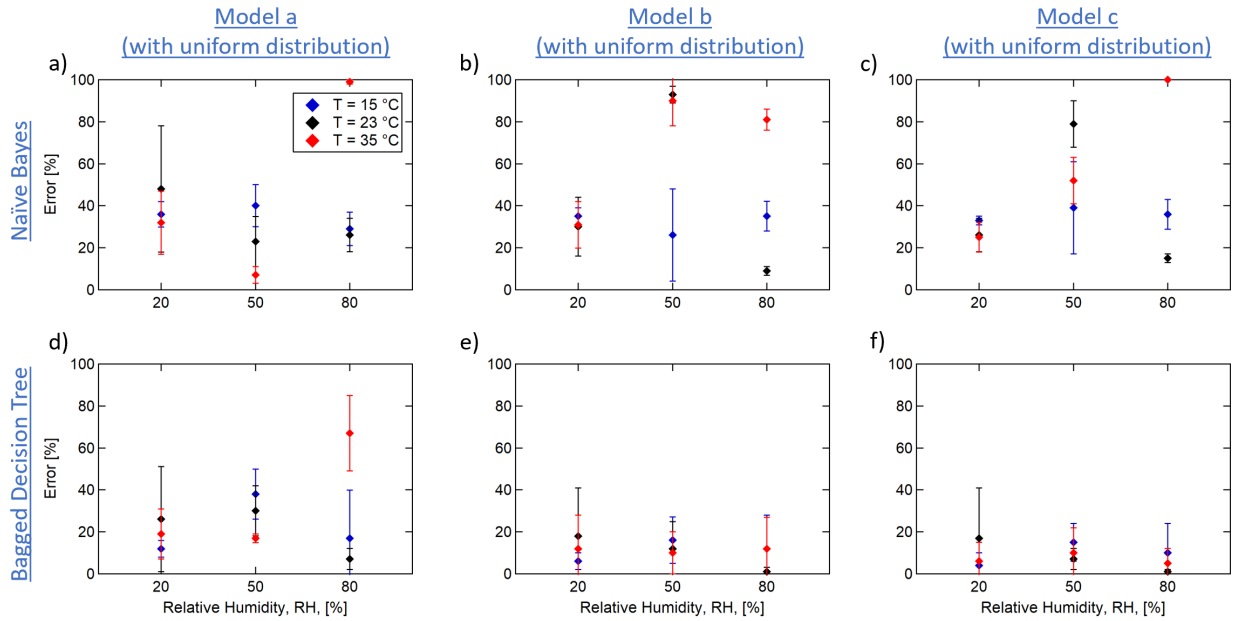

FIGURE 3.9: Error plots with uniform input data distribution: Naive Bayes (a,b,c); Bagged Decision Tree (d,e,f). Error values are listed in Table 3.6

value for contact angle with the new distribution of the input data. By a closer look, it becomes clear that changing the input data distribution changes the threshold values for dimensionless contact angle. With uniform distribution, the new threshold value for θ^* between RH of 20% and 50% is set at 0.4 instead of 0.5. As for the first row, more data points (that exceed the contact angle of 0.4) are miss-labeled as RH of 50% in the first row. On the other hand, more data points are correctly classified as RH of 50% because their value is higher than 0.5. So improvement in the accuracy of one value of the class is followed by a reduction in the accuracy of another value of the class. This is due to the fact that Naive Bayes only used the contact angle value to make predictions.

TABLE 3.6: Validation error values for uniform input data distribution (plotted in Figure 3.9)

		Naive Bayes			Bagged Decision Tree		
RH(%)	T(°C)	Model a	Model b	Model c	Model a	Model b	Model c
20	15	36(±6)	35(±4)	33(±2)	12(±4)	6(±4)	4(±6)
20	23	48(±30)	30(±14)	26(±8)	26(±25)	18(±23)	17(±24)
20	35	32(±15)	31(±11)	25(±7)	19(±12)	12(±16)	6(±9)
50	15	40(±10)	26(±22)	39(±22)	38(±12)	16(±11)	15(±9)
50	23	23(±12)	93(±4)	79(±11)	30(±12)	12(±13)	7(±5)
50	35	7(±4)	90(±12)	52(±11)	17(±2)	10(±10)	10(±12)
80	15	29(±8)	35(±7)	36(±7)	17(±23)	12(±16)	10(±14)
80	23	26(±8)	9(±2)	15(±2)	7(±5)	1(±2)	1(±1)
80	35	99(±1)	81(±5)	100(±0)	67(±18)	12(±15)	5(±7)

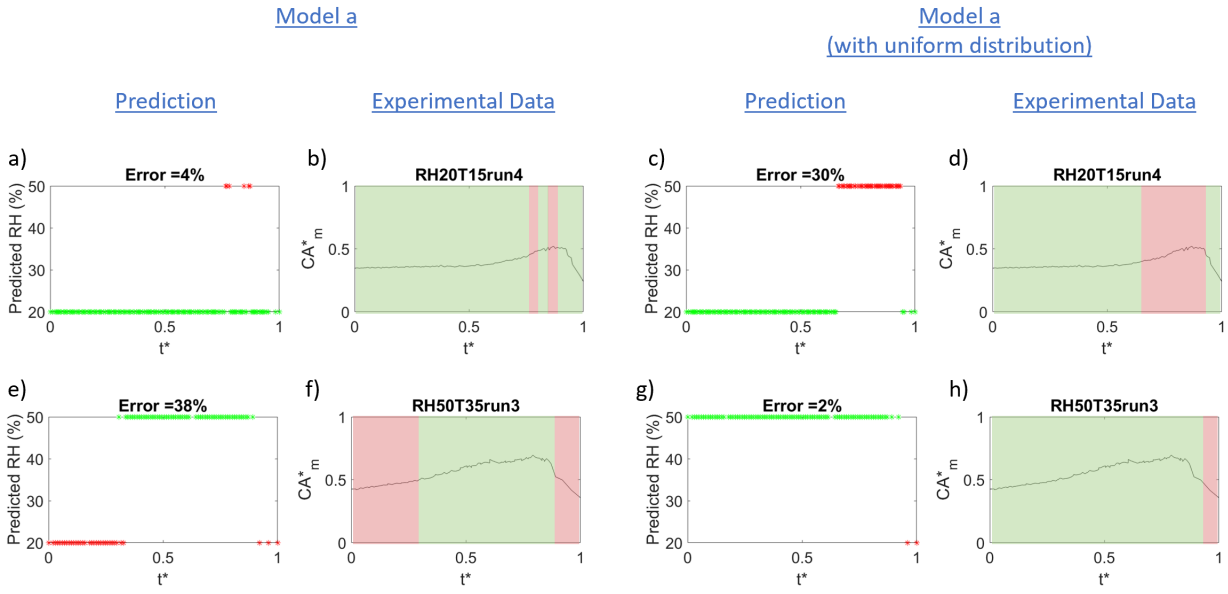

FIGURE 3.10: Naive Bayes relative humidity prediction over time and experimental data. Each row of the Figure represents a single experiment: RH = 20% (first row) and RH = 50% (second row).

3.7 Conclusions and Future Work

Study of droplet evolution has been used to reversely detect the environmental condition (i.e. relative humidity). The detection has been performed by one data point in time including macroscopic parameters. Two different classifiers have been tested: Naive Bayes and Bagged Decision Tree. Three models were built based on input variables. Model a only contains dimensionless contact angle and time as features, however models b and c include extra information on temperature and diameter in dimensionless and dimensional format, respectively. As expected Bagged Decision Tree Classifier produced more accurate results with all three models compared to Naive Bayes. Further examining the predictions made by Naive Bayes revealed that the algorithm defines threshold values for contact angle. However, it was not so transparent how Bagged Decision Tree was making predictions.

Model b and c highly improved the accuracy of Bagged Decision Tree while it did not have a net effect on Naive Bayes. This is due to the fact that Naive Bayes does not use extra information on temperature or diameter and it heavily relies on the value of contact angle. The effect of input data distribution was examined with both algorithms and all three models. It was observed that Bagged Decision Tree was very stable and did not change by altering the input data distribution. Models b and c of Naive Bayes were also quite intact by input data distribution. Nevertheless, the results of model a with Naive Bayes Classifier changed substantially by input data distribution. The reason is changing input data distribution changed the threshold values for contact angle. Therefore, the accuracy for RH = 20% decreases while it increases for RH = 50%.

Detection of relative humidity is performed by a classification problem. It is similar to classify the groups of RH as low, medium, and high. However, the ultimate goal is to

develop an algorithm which can detect any numerical value for RH. For this purpose, the classification problem should be replaced by a regression problem and more experimental data is required as well. Moreover, currently only one data point in time is used to make predictions. The next step would be to modify the approach so that it uses a series of consecutive data points in time (time window). This will probably increase the accuracy of the algorithm.

Chapter 4

Data-Driven Time-Dependent State Estimation for Interfacial Fluid Mechanics in Evaporating Droplets

This manuscript is published in Scientific Reports Journal.

Sahar Andalib [a,*] , Kunihiko Taira [a], H. Pirouz Kavehpour [a]

[a] Department of Mechanical and Aerospace Engineering, University of California, Los Angeles, CA 90095

* Corresponding Author: email sandalib@ucla.edu

4.1 Abstract

Droplet evaporation plays crucial roles in biodiagnostics, microfabrication, and inkjet printing. Experimentally studying the evolution of a sessile droplet consisting of two or

more components needs sophisticated equipment to control the vast parameter space affecting the physical process. On the other hand, the non-axisymmetric nature of the problem, attributed to compositional perturbations, introduces challenges to numerical methods. In this work, droplet evaporation problem is studied from a new perspective. We analyze a sessile methanol droplet evolution through data-driven classification and regression techniques. The models are trained using experimental data of methanol droplet evolution under various environmental humidity levels and substrate temperatures. At higher humidity levels, the interfacial tension and subsequently contact angle increase due to higher water uptake into droplet. Therefore, different regimes of evolution are observed due to adsorption-absorption and possible condensation of water which turns the droplet from a single component into a binary system. In this work, machine learning and data-driven techniques are utilized to estimate the regime of droplet evaporation, the time evolution of droplet base diameter and contact angle, and level of surrounding humidity. Droplet regime is estimated by classification algorithms through point-by-point analysis of droplet profile. Decision tree demonstrates a better performance compared to Naïve Bayes (NB) classifier. Additionally, the level of surrounding humidity, as well as the time evolution of droplet base diameter and contact angle, are estimated by regression algorithms. The estimation results show promising performance for four cases of methanol droplet evolution under conditions unseen by the model, demonstrating the model's capability to capture the complex physics underlying binary droplet evolution.

4.2 Introduction

Wetting and spreading of liquid on a solid surface is an omnipresent phenomenon in nature and engineering technologies such as biodiagnostics, inkjet printing, microfabrication, spray cooling, and agricultural irrigation [63, 10, 62, 5, 23, 47, 60, 85, 83, 88, 58, 41, 93, 34]. Droplet evaporation has gained increasing attention over the past twenty-five years [17, 81, 14, 3, 4, 96]. The original work of Deegan et al. [24] on the coffee-ring effect was followed by the comprehensive study of Hu and Larson [40] where they theoretically, experimentally, and numerically calculated the evaporation rate of sessile water droplets. Evaporation of a single component sessile droplet is influenced by various factors such as substrate temperature (Mollaret et al. [57]), environment pressure (Sefiane & Tadrist [74]), surfactant concentration (Sefiane [77]), substrate thermal conductivity (Ristenpart et al. [69], David et al. [21], Sobac & Brutin [87]), and surrounding gas (Sefiane et al. [76]). When an organic fluid droplet evaporates on a solid surface, thermocapillary instabilities known as hydrothermal waves (HTWs) are created due to surface tension gradient along the interface (Sobac & Brutin [86]).

Although the evolution of a single component droplet is mainly understood, the physics becomes complex when there is more than one component in the droplet. Three stages were reported for evaporation of water-ethanol mixture droplets (Sefiane et al. [75]) where the first stage corresponded to evaporation of a more volatile component while the last stage was responsible for evaporation of a less volatile component. The humidity of the surrounding plays a crucial role in evaporation of a binary sessile droplet. Sefiane et al. [78] and Liu et al. [55], in separate studies, observed a rise in contact angle of binary mixtures which suggested possible condensation of water on droplet. Innocenzi et

al. [42] also reported adsorption of water in ethanol and ethanol/water mixtures by time-resolved infrared spectroscopy. In a comprehensive study, Chen et al. [18] employed three different techniques of optical visualization, infrared thermography, and acoustic high-frequency echography to study the evaporation of butanol, ethanol, water/butanol, and water/ethanol droplets. Their results showed that due to the high hygroscopic power of ethanol, the humidity of the environment had a noticeable effect on the evolution of pure ethanol droplets. Heterogeneous thermal patterns alongside the evolution of acoustic reflection coefficient proved that ethanol droplet undergoes continuous water loading. The combined influence of ambient temperature and relative humidity on early stages (i.e. pinned contact angle) of ethanol droplet was examined by Fukatani et al. [32] Kita et al. [50] quantified the water loaded onto ethanol droplet by gas injection chromatography (GIC) under controlled ambient temperature and relative humidity. The observed reduction in ethanol concentration was attributed to both ethanol evaporation as well as water intake on the drop. They concluded that at low relative humidity the main mechanism for water intake was that of adsorption-absorption, though at high relative humidity water condensation plays a more dominant role. While the changes in relative humidity are commonly imposed environmental conditions, controlling ambient temperature to tune the effect of humidity is rather an expensive method for practical applications. Andalib et al. [1, 2] proposed regulating the effects of relative humidity on methanol droplet evaporation by adjusting the temperature of the substrate which is less expensive compared to controlling ambient temperature. They concluded that increasing substrate temperature maintains the liquid-gas interface temperature above the dew point which in turn limits the water condensation on the drop. They also proposed a regime map based on droplet evolution under various environmental conditions.

As the number of components in the droplet increase, the underlying physics become

more complex. Recently, multi-component droplet evaporation revealed new phenomena such as spontaneous nucleation of oil microdroplets, phase transition, and multi-component diffusion (Tan et al. [92], Diddens et al. [25], Li et al. [54], Lohse & Zhang. [56]). Such intricate physics with numerous parameters in play makes experimental studies sophisticated and time-consuming while requiring advanced equipment to finely control the environmental condition. On the other hand, the highly non-axisymmetric nature of the problem due to compositional inhomogeneities brings up significant challenges to numerical models.

Machine learning methods have emerged as powerful tools for analyzing a wide range of fluid mechanics problems (Brenner et al. [12] and Brunton et al. [13]) such as turbulence (Duriez et al. [29], Singh et al. [84], Duraisamy et al. [28], and Fukami et al. [31, 30]), phase transition (Jadrich et al. [44]), ignition (Popov et al. [64]), vortex vibrations (Raissi et al. [66] and Verma et al. [94]), and aerodynamics disturbances (Hou et al. [39]). Image processing and pattern recognition techniques have been employed to analyze the remaining stains after evaporation of sessile droplets. Analysis of patterns in dried drops of biological fluids revealed a lot of information for medical diagnostics (Yakhno et al. [95], Killeen et al. [48], Shabalin et al. [80], Brutin et al. [15], and Hamadeh et al. [37]). Kim et al. [49] and Gorr et al. [33] showed that the chemistry of fluid and substrate can be identified by recognition of patterns in the stains. The aforementioned studies utilize machine learning techniques to indirectly measure and detect the mechanisms inside droplet from the footprint after evaporation. Here, we introduce a data-driven approach to directly analyze the dynamics of binary droplet evaporation (induced by transfer of a second component present in the atmosphere).

In the present study, we use data-driven classification and regression algorithms to

analyze the real-time behavior of a methanol droplet at different levels of environmental humidity and temperature of the substrate. The present approach is real-time in a sense that the model reveals the state of the droplet at each point in time. Water uptake into droplet through adsorption-absorption and possibly condensation turns methanol droplet into a binary system. Based on the environmental condition, droplet evolves in different regimes: evaporation-dominated, transition, or condensation-dominated. The capability of the proposed model is evaluated by estimating four different parameters, namely: regime of droplet evaporation (through classification algorithms), level of surrounding humidity (through regression algorithms), time evolution of droplet base diameter (through regression algorithms), and time evolution of droplet contact angle (through regression algorithms). First, a classification algorithm is trained to estimate the regime of droplet evaporation through analysis of diameter and contact angle evolution over time. The objective of the model is to detect the regime of droplet evolution with even a single data point at a specific time. Second, a regression algorithm is utilized to detect the humidity of the surrounding by analyzing droplet evolution. The high hygroscopic nature of methanol allows greater amount of water uptake into droplet in humid environments. The higher content of water in droplet increases the contact angle and alters the rate of change of volume. The regression model analyzes these changes and reversely estimates the humidity. Last, given the condition of the surrounding, the continuous evolution of macroscopic parameters of droplet, i.e., diameter and contact angle, is estimated. Our method shows great potential in opening up new paths to analyze more complicated multi-component droplet evolution and interfacial fluid mechanics in general. Estimating the evolution of different parameters of droplet is a crucial step in designing high quality and high-resolution finish products in droplet-based biodiagnostics, inkjet printing, and microfabrication technologies. Our proposed method provides necessary information on

evaporation of organic liquid droplet under various environmental conditions with simple and easy-to-use algorithms without the need to perform complicated simulations. We show that the regime of droplet, relative humidity of surrounding, and time evolution of diameter and contact angle can be estimated under various conditions. In real-world applications anticipating the regime of droplet is of great importance as in many instances, the occurrence of one regime or the other should be avoided. For example, a droplet sitting on a surface forever is not ideal for high resolution of printing or biosensing.

4.3 Results

4.3.1 Physics of Droplet Evaporation

Droplet evaporation is influenced by numerous factors including liquid/substrate properties as well as environmental conditions [7, 21, 87, 69, 76, 32, 50]. We analyze the evolution of a sessile methanol droplet through macroscopic parameters: volume, V, diameter, D, contact angle, θ, and time, t, under controlled relative humidity of surrounding, RH, and substrate temperature, T (see Fig. 4.1a inset). The variables are nondimensionalized as: $t^* = t/t_f$, $V^* = V/V_0$, $D^* = D/D_0$, $\theta^* = \theta/\theta_0$, $T^* = T/T_0$, $RH^* = RH/RH_0$, where $\theta_0 = 90^\circ, T_0 = 35^\circ C, RH_0 = 100$, and t_f, V_0, D_0, that are experimentally measured, stand for total evaporation time, initial volume, and initial diameter, respectively. The experiments are conducted in a chamber with controlled humidity and on a substrate with controlled temperature (Fig. 4.1a). Fig.4.1a Details of experimental procedure are given in Materials and Methods Sect. Three regimes of droplet evolution are observed under various relative humidity of the surrounding and substrate temperature (Fig. 4.1b-top left) namely: evaporation-dominated, transition, and condensation-dominated. Three

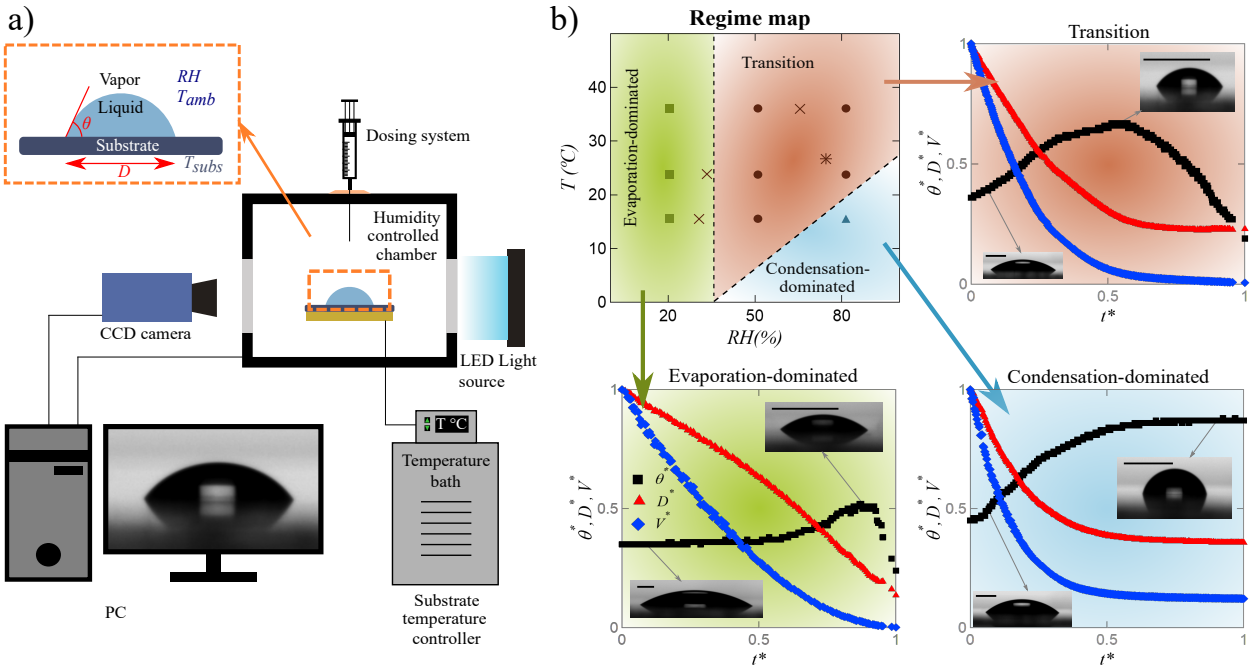

FIGURE 4.1: a) Schematic of the experimental setup with macroscopic parameters of droplet shown in the inset; b) regime map of droplet evaporation (top-left) under various relative humidity (RH) of surrounding and substrate temperature (T), evolutions of nondimensional contact angle, volume, and diameter versus time for evaporation-dominated (bottom-left), transition (top-right), and condensation-dominated (bottom-right) regimes. Each scale bar in droplet images represents a length of 1mm. The schematic is made using free and open-source software Inkscape (Harrington [38])

sub figures represent the evolutions of θ^*, V^*, and D^* over t^*. Nondimensional plots are reported to better visualize different evolution patterns.

At low relative humidity (the green-shaded region in Fig.4.1b), change in substrate temperature does not alter the qualitative evolution of droplet. In this regime, the contact angle stays constant for most of droplet lifetime followed by a slight increase and a sharp decrease towards the end (Fig.4.1b-bottom left). The modest rise in contact angle is attributed to the interplay of high evaporation rate of methanol and receding speed at the triple line [78]. Diameter and volume monotonically decrease during droplet lifespan.

Due to the high hygroscopic nature of methanol, at higher relative humidity, water

vapor transfers into the droplet at the liquid-gas interface. Water adsorbing-absorbing and possibly condensing on the interface is reported in previous studies [75, 18, 42, 32, 1, 50]. The growth in the concentration of water content changes the interfacial tensions and results in higher contact angle [50, 18, 1]. Unlike low relative humidity, substrate temperature plays a determining role in the regime of droplet evolution at high relative humidity of the surrounding. In the transition regime (red-shaded region), contact angle rises to a maximum value before gradually decreasing towards the end of droplet lifetime. Increasing contact angle demonstrates water uptake into droplet while methanol is evaporating. At the point of maximum contact angle, most of methanol has already evaporated and droplet consists mainly of water. However, some studies revealed that a small amount of residual methanol remains until the end of droplet lifetime [78, 55]. Even though diameter and volume decrease monotonically, two obvious slopes are observed in their evolutions (Fig.4.1b-top right). The two slopes correspond to two stages: the initial stage when merely methanol evaporates and the second stage when water mainly evaporates at a slower rate.

When the humidity of the environment is high and the substrate temperature is sufficiently low, another regime is observed. In condensation-dominated (blue-shaded) regime, contact angle monotonically increases until it reaches a plateau. Both diameter and volume converge to a non-zero value. Lower substrate temperature enhances water uptake through condensation by dropping the liquid-gas interface temperature below that of dew point [1]. In this regime, droplet comes to a quasi-steady state with a remaining droplet consisting mainly of water [78, 55, 18, 50].

4.3.2 Regime Classification

We have used a classification algorithm to detect the regime of droplet evaporation as sketched in Figure 4.1b. The classifier is trained with data on contact and diameter at each specific point in time and then classifies the regime of droplet evaporation. Dependence of variables is shown by the correlation matrix in Fig. 4.2a where RG stands for the regime of droplet evaporation. Diameter and volume are coupled for a spherical cap sessile droplet through the relation $V = (\pi/3)(D/2)^3(2+\cos\theta)(1-\cos\theta)^2$ which assumes slow quasi-static evaporation. t^*, D^*, and θ^* are used as input variables and RG is the target variable. It is observed that the contact angle is highly proportional to humidity because the higher the humidity, the higher the amount of water uptake into drop. Higher water content increases the interfacial tension at the triple line which results in higher contact angles.

The framework for detection of the regime of droplet evaporation characterizes the behavioral pattern of droplet by learning the values of contact angle and diameter at each specific point in time and classifying them to each regime. The model then labels the test and validation sets based on similar evolution observed previously during training. The ratio of training to test set is 80 to 20%. Two classifiers of Naïve Bayes (NB) and decision tree (DT) are trained and confusion matrices are used to compare the performance of classifiers on the test set (Fig. 4.2b). Precision, recall, F-score, and overall accuracy

TABLE 4.1: Regime classification results on test set: standard metrics for two different classifiers

Classifier	Accuracy	RG	Precision	Recall	F-score
NB	0.75	Evap.	0.74	0.65	0.6
		Trans.	0.81	0.78	0.79
		Cond.	0.46	0.93	0.61
DT	0.96	Evap.	0.99	0.97	0.97
		Trans.	0.97	0.96	0.96
		Cond.	0.83	0.89	0.85

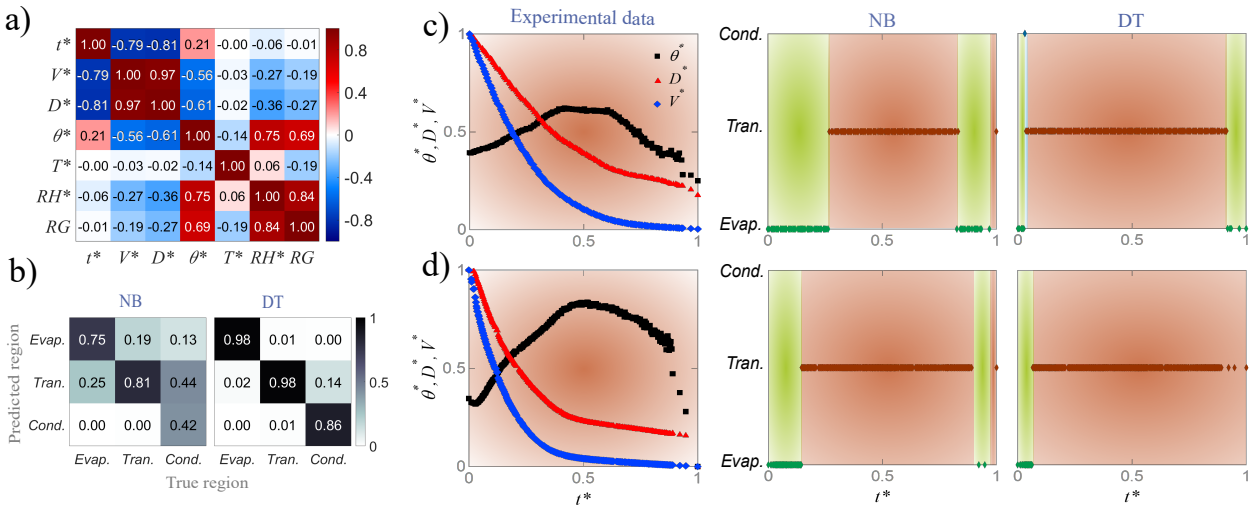

FIGURE 4.2: Results of regime classification: a) correlation matrix for parameters in droplet evaporation; b) results of test set for regime detection illustrated with confusion matrices for Naïve Bayes (NB) and decision tree (DT) algorithms; c) point-by-point validation results with NB and DT classifiers for regime detection with experimental data of droplet evaporation for RH = 80% and T = 35°C; d) point-by-point results of estimation set with NB and DT classifiers for regime detection with experimental data of droplet evaporation for experiment #4 (RH = 75% and T = 25°C) in estimation set. The colors in c and d correspond to the regime colors used in Figure 4.1.b.

values (shown in Table 4.1) provide a comprehensive evaluation of the performance of each classifier on the test set. Based on the results shown in the Fig. 4.2b and Table 4.1, DT outperforms NB for all regimes of the test set. It is also observed that the detection of the condensation-dominated regime is challenging for both classifiers. Detection of evaporation-dominated regime reaches an F-score value of 0.97 with decision tree classifier.For NB, around half (43%) of the points in the condensation-dominated regime are classified as transition regime (see Fig. 4.2b). Replacing diameter with volume slightly improves the results for both classifiers (6% on average) for this regime. This is due to a more discernible evolution of V^* compared to D^* towards the end of droplet lifetime for this regime. However, since measuring diameter is a more direct approach and also more convenient for the user, the model is trained with diameter.

TABLE 4.2: Regime classification results on validation set under each specific RH and T condition with two different classifiers

Classifier	$RH(\%)$	$15^{\circ}C$	$23^{\circ}C$	$35^{\circ}C$
NB	20	0.72 ($\pm$0.04)	0.73 ($\pm$0.08)	0.78 ($\pm$0.06)
	50	0.80 ($\pm$0.06)	0.62 ($\pm$0.11)	0.63 ($\pm$0.02)
	80	0.41 ($\pm$0.10)	0.88 ($\pm$0.06)	0.83 ($\pm$0.08)
DT	20	0.98 ($\pm$0.03)	0.96 ($\pm$0.08)	0.96 ($\pm$0.08)
	50	0.94 ($\pm$0.10)	0.94 ($\pm$0.03)	0.98 ($\pm$0.03)
	80	0.74 ($\pm$0.23)	0.97 ($\pm$0.05)	0.94 ($\pm$0.07)

The capability of the model to detect the regime of droplet evaporation under each specific condition (RH and T) is evaluated through a validation set. The validation step is performed on a single experiment at each time that is held out during training/testing. Validation results, averaged for each condition, are presented in Table 4.2. The accuracy and recall are the same for validation because at each condition there is only one true regime. Fig. 4.2c illustrates a sample of validation for $RH = 80\%$ and $T = 35^{\circ}C$. The classifier assigns a region for each point in time based on the value of contact angle and diameter. The true regime for this condition is the transition regime (red). The red regions on the two plots on the right side of Figure 4.2c represents the regions that are classified correctly as transition regime and the green regions show the regions that are incorrectly classified as the evaporation-dominated regime. It is observed that both classifiers correctly detect the region of the majority of the data points although DT demonstrates better performance. NB struggles at the beginning and end of droplet lifetime. This issue is less pronounced for DT.

The capability of the model to estimate the regime of droplet is evaluated on an estimation data set from conditions that are unseen by the model and do not contribute to the model training, testing, and validation. The values of RH and T for these conditions are randomly selected in the range of $20\%<RH<80\%$ and $15^{\circ}C<T<35^{\circ}C$ (shown with cross

TABLE 4.3: Results of regime estimation for four experiments under new conditions unseen by the model. The true regime of each experiment is shown on the regime map in Figure 4.1b.

			NB		DT	
Experiment	$RH(\%)$	$T(^{\circ}C)$	Evap.	Trans.	Evap.	Trans.
1 (X)	30	15	0.54	0.46	0.67	0.33
2 (X)	33	23	0.61	0.39	0.79	0.21
3 (X)	65	35	0.32	0.68	0.16	0.84
4 (*)	75	25	0.18	0.82	0.07	0.93

and star marks on the regime map of Figure 4.1b). The model classifies each experiment under each regime with different ratios as shown in Table 4.3. For example, experiment 1 with RH of 30% and T of $15^{\circ}C$ is close to the boundary of evaporation-dominated and transition regimes. With NB, 54% of the data points in this experiment are classified as evaporation-dominated regime and 46% as transition regime. This is expected due to the location of experiment 1 on the regime map. It should be noted that the lines on the regime map are approximate boundaries. Fig. 4.2d demonstrates regime estimation of all data points of experiment 4 with both classifiers. The shown evolution of contact angle is not similar to any of the evolutions shown in Fig. 4.1b subfigures. In fact, contact angle decreases at the beginning and then starts rising. Experiment #4 falls in transition regime. That is the reason that the profile for experimental data in Figure 4.2d is colored in red for the true regime of experiment #4. As it is seen, NB and DT correctly classify 84 and 93% of the data points in experiment 4 to transition regime. The green regions represent the data points that are incorrectly classified as evaporation-dominated regime.

4.3.3 Relative Humidity Estimation

In this section, we show the ability of the model to detect environmental humidity by analyzing the evolution of contact angle and diameter through regression algorithms. Polynomial regression with four different orders (linear, quadratic, third-order, and fourth-order) and regression tree are used for training. The coefficient of determination (R^2) increases from 0.66 for linear up to 0.93 for fourth-order polynomial regression. The test results for all five regression methods are shown in Fig. 4.3a. The horizontal axis shows the true value of RH^* and the vertical axis shows the estimated values averaged over all the points for each RH^*. As it can be seen, the higher the order of polynomial regression, the closer the average estimation to the ground-truth value and the smaller the error bar. Furthermore, regression tree performs more accurately compared to all polynomial regression methods. Model performance under each specific condition through validation set is shown in Fig. 4.2b. The consistent colors throughout Fig. 4.3a-c represent different regression methods and different markers are used for each substrate temperature in Fig. 4.3b. Based on the results shown in Fig. 4.3b, all methods except linear regression produce reasonably accurate results. The validation results get closer to actual values as the order of the polynomial regression increases. Nonetheless, it must be noted that higher order polynomial regression increases the computational cost as well as the chance of over-fitting. Performance of regression tree is comparable to third-order and fourth-order polynomial. The capability of different regression methods to estimate new humidity values by analyzing the time evolution of contact angle and diameter is presented in Fig. 4.3c. The new relative humidity values (30, 33, 65, and 75%) are randomly selected in the range of 20-80%. It is noteworthy that the model has not seen any data of droplet evolution under these RH values during training, testing, or validation. It is seen that, unlike testing and validation where increasing the order of polynomial

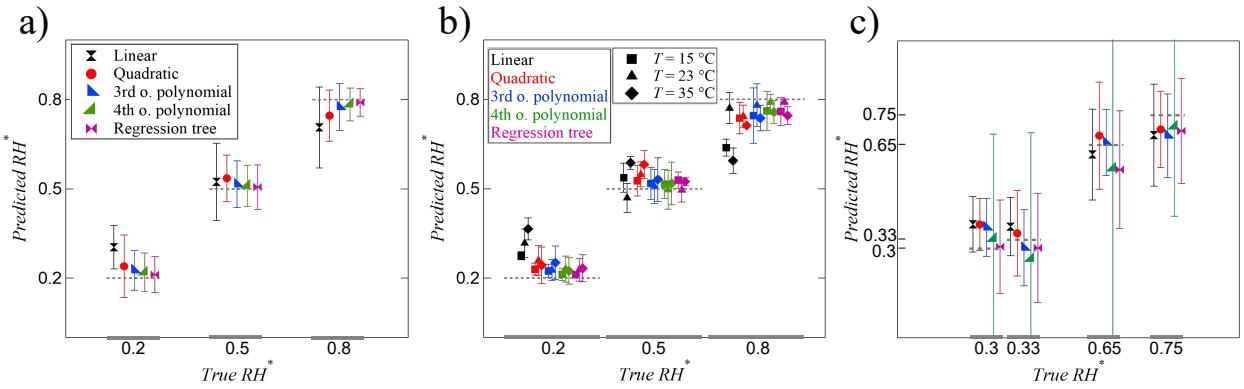

FIGURE 4.3: Relative humidity regression results: a) test set; b) validation; c) estimation. Markers for all colors in (b) represent different temperatures as shown in legend. Markers and colors in (c) are the same as in (a).

or complexity of the model (i.e., regression tree) produces more accurate results, higher order polynomials do not result in better estimation of unseen conditions. As a matter of fact, linear, quadratic, and third-order polynomials estimate more accurately. This is a common issue when the model fits the training data very well and it negatively affects the model performance on the new data set. Fig. 4.3c clearly indicates over-fitting with fourth-order polynomial.

4.3.4 Diameter and Contact Angle Estimation

In this section, the capability of the model to estimate the continuous evolution of contact angle and diameter over time is evaluated through regression algorithms. This means that the model estimates the evolution of diameter and contact angle at each time increment (approximately one second apart). The input variables include T^*, RH^*, t^*, and θ^* (or D^*) and the target variable is D^* (or θ^*). By increasing the order of the polynomial, the coefficient of determination, R^2, for training improves from 0.87 to 0.99, and from 0.78 to 0.96 for diameter and contact angle estimation, respectively. The performance of five different regression methods on the test set is presented in Fig. 4.4a. The first row

represents the results when D^* is the target variable and the second row illustrates the results for θ^* as the target variable. The closer the distribution of data to the diagonal line in these plots, the better the performance of the model on the test set. Based on the results shown in Fig. 4.4a., the diameter test results saturate after third order polynomial while for contact angle the performance keeps improving when increasing the degree of polynomial from third to fourth.

The validation results are summarized in Fig. 4.4b. for D^* (top) and θ^* (bottom) in terms of R^2 and root mean square error *rmse*. With D^* being the target variable, an average R^2 of 0.8 or higher and average *rmse* less than 0.1 are achieved for all nine conditions. Going from linear to quadratic to third order polynomial increases and decreases the value of R^2 and *rmse*, respectively. The profiles of R^2 and *rmse* exhibit saturation, and further increase in the order of the polynomial does not improve model performance on validation data. This is consistent with the test results where model performance saturates at third order. Furthermore, regression tree demonstrates accuracy comparable to third-order and fourth-order polynomials. By comparing the range of axes in Fig. 4.4b-top with bottom, it is obvious that R^2 values are generally lower (hardly reaching 0.7) and error is higher when θ^* is the target variable. In fact, there are a few instances where the average R^2 turns negative, suggesting that the overall estimation of the model is worse than an estimation with a constant average value.

The performance of the model on estimating the evolution of θ^* and D^* versus time under four new conditions that did not contribute to model training, testing, or validation as shown in Fig. 4.4c. One value of R^2 and *rmse* is reported for each condition (or experiment) which shows the overall quality of the fit. Higher coefficients of determination and lower *rmse* values demonstrate the better performance of the model in estimating D^* then θ^* evolution. Based on the results shown in Fig. 4.4c, third order polynomial regression

has the best performance in estimating diameter. The results become less accurate with fourth-order polynomial which suggests over-fitting. It is interesting to note that regression tree, which had higher accuracy during testing and validation, is outperformed even by linear regression during estimation. The evolution of diameter versus time estimated by quadratic regression for Experiment 3 is depicted in Fig. 4.4d. As it can be seen, even with a quadratic regression, the model estimates the evolution of D^* quite accurately for an unseen condition. Considering the range of values on axes of Fig. 4.4c-top and bottom, estimating the evolution of contact angle is more challenging for the model. Unlike estimating diameter, increasing the order of polynomials has a negligible effect. The accuracy of the model stays almost constant for linear, quadratic, and third order. However, it worsens drastically for fourth-order polynomial due to over-fitting the data. The R^2 and *rmse* values for fourth-order polynomial fall outside the range shown in the plot. Since the estimation of θ^* is generally more challenging for the model, the effect of over-fitting is more noticeable compared to D^* estimation. The overall better performance of the model for diameter estimation compared to contact angle estimation is due to the fact that diameter evolution is relatively smooth and therefore easier to estimate where contact angle evolution changes substantially under different conditions. Figure 4.4d-bottom illustrates contact angle evolution over time estimated with third-order polynomial for Experiment 1 which is in the evaporation-dominated regime. Although the maximum value of contact angle is underestimated with 3$^{\text{rd}}$ order polynomial, the time corresponding to the maximum contact angle is estimated accurately. Also, there is a good agreement between the estimated and actual contact angle evolution during most of droplet lifetime with R^2 value of 0.74 and *rmse* of 0.05.

4.4 Discussion

In this study, we have analyzed the complex physics of sessile droplet evaporation (which starts with a single component and turns into a binary system due to the transfer of a second component i.e., water) through machine learning, classification and regression algorithms. Four different parameters pertaining to droplet evaporation, namely: regime of droplet evaporation, level of surrounding humidity, time evolution of droplet base diameter, and time evolution of droplet contact angle, are estimated. Point-by-point analysis of droplet profile enables real-time estimations given a limited number of data points. The present approach is a real-time state estimation in a sense that the model assesses the evolution of droplet parameters at every single point in time. This means that the model does not need the entire evolution profile of a droplet to make an estimation. Instead, only a few (or even a single) data points are (is) sufficient for estimation, although more data points result in more accurate estimation. The model estimation capability is then assessed on the data that do not contribute to training, testing, or validation.

Two different classifiers are utilized to estimate the regime of droplet evaporation. NB is chosen as a simple easy-to-interpret algorithm, while DT serves as a more powerful algorithm. As expected, DT outperforms NB due to a more robust internal structure at the expense of computational cost and transparency. Both classifiers showed impressive performance (minimum 75% accuracy) on estimating the regime of droplet. Knowledge on droplet evaporation regime is necessary for compatible designs in numerous industries such as droplet-based biosensors or ink-jet printing.

Additionally, level of surrounding humidity, time evolution of droplet base diameter, and time evolution of droplet contact angle are estimated through regression techniques.

Polynomial regressors, as well as regression tree, are trained through point-by-point analysis of droplet evolution. The model performance improved by increasing the order of the polynomial and using regression tree for training, test, and validation sets. However, when estimating the new conditions unseen by the model, fourth-order polynomial and regression tree suffered from data over-fitting. The best performance of the model is achieved by third-order polynomial. In general, the model estimation results are more accurate when estimating diameter evolution compared to contact angle estimation. This is due to smoother, hence easier to estimate, evolution of diameter with time. The sharp changes in θ^* under different conditions make the estimation of its evolution challenging for the model. Information of this type is of great importance for technologies such as ink-jet printing, or droplet-based biodiagnostics where the estimations can provide critical information on the base diameter or contact angle of the droplet at a specific time.

In the current work, behavior of a sessile droplet transitioning from a single fluid into a binary mixture following transfer of a second component from the atmosphere is studied through data-driven techniques. The model demonstrated promising performance detecting the regime of droplet evolution, the humidity level surrounding droplet, and time evolution of diameter and contact angle. The current case study demonstrates the capability of the proposed model to analyze complex interfacial fluid mechanics problems through machine learning algorithms. Although we have estimated four parameters of droplet evaporation by this model, these kinds of techniques can be expanded to perform a wide range of estimations. Our preliminary study opens up new ways to study binary or multi-component droplet evolution which might lead to better analyzing the complex physics of the problem.

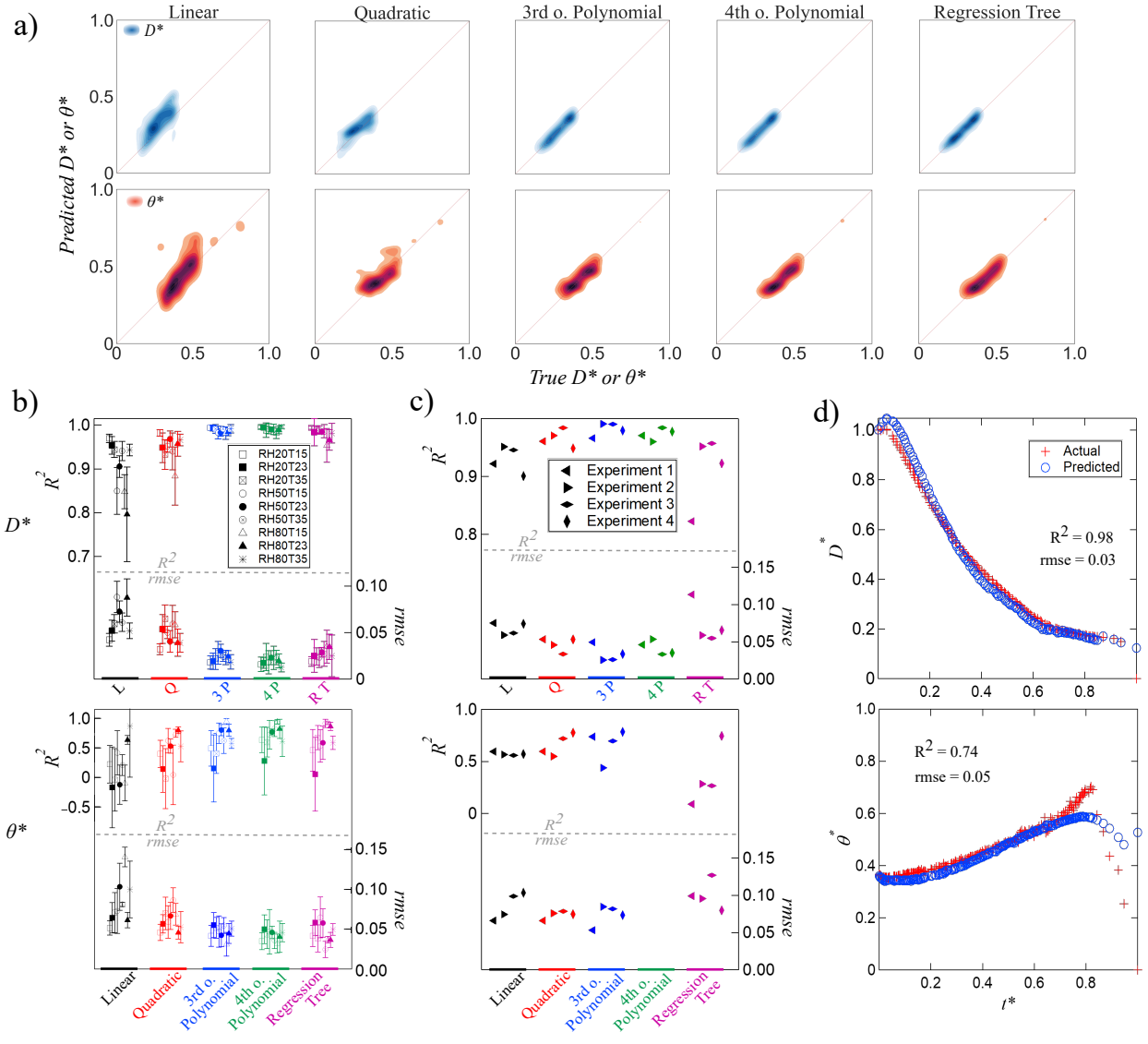

FIGURE 4.4: Diameter (D*) and contact angle (θ^*) regression results: a) test set; b) validation set; c) estimation set; d) diameter estimation with quadratic regression for E3 (top) and contact angle estimation with third-order polynomial regression for E1 (bottom).

4.5 Methods

4.5.1 Experimental Setup and Procedures

The experiments are carried out in a chamber (with dimensions $127 \times 127 \times 76\ mm^3$) of drop shape analyzer (DSA 100) from KRÜSS. The relative humidity inside the chamber is controlled and the temperature is kept at room temperature (i.e. 23 °C). The bottom side of the chamber is equipped with a Peltier plate (electrical system and a temperature bath) to control the substrate temperature. The top of the chamber has a small hole for passing the syringe. Both sides of the chamber have transparent windows for visualization purposes. A LED light is used for illumination and a CCD camera is utilized to capture the time evolution of droplet profile (Fig. 4.1a). The whole setup is mounted on an anti-vibration table to eliminate environmental disturbances.

Methanol is purchased from Fisher Scientific with a purity of 99.8%. The glass substrates are coated with a very thin PDMS (polydimethylsiloxane) layer to achieve spherical and reproducible droplets with measurable contact angles. In order to ensure that methanol does not interact with the PDMS coating, multiple methanol droplets are successively deposited at the same location on the substrate and let evaporate. No change is observed in the initial contact angle of droplets or in their evolution during evaporation. The relative humidity inside the chamber and the temperature of the substrate are set to desired values and enough time is passed to make sure quasi-steady state is achieved. Three values of relative humidity: 20%, 50%, and 80% alongside three values of substrate temperature: 15°C, 23°C (room temperature), and 35°C are tested. A drop of methanol is gently deposited on the glass substrate. Droplet volume is under $5\mu l$ in order to keep droplet size below capillary length. The corresponding volume to the capillary length for methanol droplet is around 45 μl. The evaporation process of methanol droplet is recorded by the

CCD camera at 50 frames per second. All experiments under each relative humidity and substrate temperature condition are repeated five to ten times to ensure the reproducibility of the data. A KRÜSS Drop Shape Analyzer software is utilized to measure the time evolution of contact angle (θ), base diameter (D), and volume (V). Due to the observed differences between the right and left contact angle values, elliptical fit is used for contact angle and volume measurements. For better analysis of droplet behavior, all dimensional parameters are nondimensionalized as followed: $D^* = D/D_0$, $V^* = V/V_0$, $t^* = t/t_f$; where D_0, V_0, and t_f are initial diameter, initial volume, and total evaporation time, respectively.

4.5.2 Data Acquisition

The data for the model is generated by experiments of methanol droplet evaporation under various environmental conditions. Nine different conditions are created by a combination of three levels of surrounding relative humidity: 20%, 50%, and 80% with three substrate temperatures: $15^\circ C$, $23^\circ C$, and $35^\circ C$. For each of these nine conditions, the relative humidity in the chamber and substrate temperature is set to the desired values and enough time is passed to ensure quasi-steady state. Then a droplet of methanol is gently deposited on the substrate and the evolution of droplet base diameter, contact angle, and volume is recorded over time with a CCD camera of Drop Shape Analyzer (see Fig.4.1a inset). Each point in time with corresponding contact angle, diameter, and volume is considered a data point for the model.

4.5.3 Data Partitioning and Processing

The data generated under nine different conditions mentioned in the previous section are used to train, test, and validate the model. The droplet evaporation experiments for each of these nine conditions are repeated five to ten times to make sure that the results are consistent and reproducible. We carried out 60 droplet evaporation experiments under these nine conditions which created a total number of 10,850 data points that are used for training, testing and validating the model. There are additional 761 data points that are used to assess the performance of the model at the final step. The environmental conditions under which these data points are generated are completely different than the other 10,850 data points used for training, testing, and validating the model.

4.5.4 Training and Testing

The data for training, testing, and validation are generated by methanol droplet evaporation under nine different conditions which are the combinations of three levels of surrounding humidity: 20%, 50%, and 80% with three substrate temperatures: $15°C$, $23°C$, and $35°C$. The behavior of droplet under the same condition is similar between experiments however it is not exactly the same due to microscopic defects of the surface, initial conditions, etc. The data from a single experiment is held out at the beginning of training as a validation set. The remaining data from 59 experiments is partitioned into a training set and a test set with 80-20% ratio. It should be noted that multiple training to test set ratios are examined to ensure the convergence of the model which is discussed in the "Performance Criteria" section.

4.5.5 Cross Validation

A 10-fold cross-validation is carried out. The results for the test set show one of 10 scenarios from the test set. Cross-validation is performed to ensure all the results for training and test set are similar to each other and there is no anomaly in the data.

4.5.6 Validation

Once the model is trained and tested, it is then examined on the validation set that was held out at the beginning of training. The validation set that is kept out is the data pertaining to one whole experiment out of 60 experiments. This means that the model has not seen the data for the specific experiment in the validation set. Validation is performed to specifically evaluate the performance of the model under each specific condition of surrounding humidity and substrate temperature. This procedure is repeated 60 times until each experiment is held out once and validated. Validation results are averaged over all experiments under each specific RH and T condition.

4.5.7 State Estimation

There are additional 761 data points, called estimation set, that are generated by four experiments of methanol droplet evaporation. It must be noted that the machine has not seen any data of droplet evaporation under these new conditions. The data in the estimation set does not contribute to the framework during training, testing, or validation. The surrounding humidity and substrate temperature for these new conditions are randomly selected to be in the range within which the model is trained (i.e. $20\%<RH<80\%$ and $15^{\circ}C<T<35^{\circ}C$).

4.5.8 Performance Criteria

The performance criteria of the model are reported by standard metrics. For classification, the confusion matrix of the model is used as well as the precision, recall, F-score, and overall accuracy values for each regime. For validation, the accuracy values are the same as recall values for each combination of RH and T because there is only one true regime for each validation set. For regression methods, coefficient of determination (R^2) is reported to show how well the model fits the data in the training set. For RH testing, validation, and estimation, the actual RH of the environment is compared against the estimated value of RH. When D^* (or θ^*) is the target variable, the test results are demonstrated as estimated values versus actual values. The validation and estimation results are reported by R^2 that shows the quality of the fit; the proportion of variance in the target variable which is predictable from the input variables; and root mean squared error ($rmse$) which represents how much the estimation is off on average when estimating the average target variable. We have also tested the model convergence for both classification and regression algorithms. We trained the model by considering only fractions of the available data i.e., 80%, 70%, 60%, and 50%, and observed that the results for the test set remain unchanged. This proves the fact that the number of data points used for machine learning of this specific problem is converged.

4.5.9 Classifiers

We have used Naïve Bayes Classifier [16, 51, 52, 53] as a simple and easy-to-interpret algorithm. Since the algorithm is simple, there is less chance for over-fitting the data, it is faster and needs a smaller memory footprint. However, the restrictive underlying

assumptions compromise its accuracy for real case scenarios when the variables are not fully independent of each other.

Bagged Decision Tree [91, 72, 67] with 250 trees is also used. It is a powerful classifier with built-in support for cross-validation and a specialized function to measure feature importance. However, it results in complex models that are not very transparent. It is often hard to understand how it makes estimations.

Chapter 5

Onset of Ouzo Effect in Evaporative Mixture Droplet: Relative Humidity and Substrate Temperature Considerations

This manuscript is in preparation for submission.

Sahar Andalib [a,*] , H. Pirouz Kavehpour [a]

[a] Department of Mechanical and Aerospace Engineering, University of California, Los Angeles, CA 90095

* Corresponding Author: email sandalib@ucla.edu

5.1 Abstract

Droplet evaporation is an omnipresent phenomenon in nature as well numerous industries ranging from microfabrication to biodiagnostics. Many factors such as liquid/substrate properties as well as environmental conditions affect the evolution of droplet. In this work, we have experimentally investigated the effect of relative humidity of the environment on evolution of a methanol-anise oil mixture droplet. We show that the initial

binary droplet turns into a ternary droplet due to absorption/adsorption and/or condensation of water vapor into droplet. The onset of nucleation of oil microdroplets in droplet and formation of an oil ring is highly dependant on the relative humidity. The lower the relative humidity, the later the onset of nucleation. Furthermore, we tried to control the water uptake to the droplet by changing the substrate temperature. Increasing the substrate temperature had two effects. First the interface temperature remains above the due point temperature and condensation of water vapor is limited. Second the faster evaporation of droplet reduces the total amount of water uptake to the droplet. Additionally, we have coupled infrared thermography with optical microscopy. Our observation revealed that the hydrothermal waves, that are the result of surface tension gradient and presence of methanol, reduce over time by water uptake into droplet. The results of this work open up easy and inexpensive method to alleviate the unwanted effects of environment on the final products of coating techniques such as light emitting diods (LEDs), microfabrication techniques, and droplet based biosensors.

5.2 Introduction

Droplet evaporation is an omnipresent phenomenon in nature as well industries such as spray cooling, ink-jet printing, microfabrication, biodiagnostics, DNA mapping, agricultural irrigation and crop dusting [63, 10, 62, 5, 22, 47, 60, 85, 83, 88, 58, 41, 93, 34]. Sessile droplet evaporation and the challenges it presents has caught scientific attention for over two decades now [17, 81, 14, 3, 4, 96]. Whenever there is a spillage of coffee or any other beverage, the stains remaining on the surface after droplet evaporation have darker periphery compared to the center. This well-known coffee-ring effect was explain by the original work of Deegan et al. [24]. They revealed that the distribution of evaporative

flux is not distributed uniformly along the liquid-gas interface, rather it increase with radial position. In fact, the higher evaporative flux occurs at the contact line (or triple line) where all three phases of solid, liquid, and gas meet. The maximum evaporative flux at the contact line creates an outward radial flow inside the droplet which brings the liquid and potential particles to the edge to replenish the lost liquid due to evaporation. Later on, Hu and Larson [40] experimentally, theoretically, and numerically calculated the evaporation rate of sessile water droplets. Multiple factors influence the evaporation of a pure liquid droplet such as substrate temperature [57], environment pressure [74], surfactant concentration [77], substrate thermal conductivity [69, 21, 87], and surrounding gas [76].

Although the evolution of a single component droplet is mainly understood, the physics becomes complex when there is more than one component in the droplet. Three stages were reported for evaporation of water-ethanol mixture droplets where the first stage corresponded to evaporation of a more volatile component while the last stage was responsible for evaporation of a less volatile component. The middle stage was a transition stage where the contact angle experiences a rise [75]. The humidity of the surrounding plays a crucial role in evaporation of a binary sessile droplet. Sefiane et al. [78] and Liu et al. [55] both reported a rise in contact angle of binary mixtures which suggested possible condensation of water on droplet. Adsorption of water in ethanol and ethanol/water mixtures is also reported by time-resolved infrared spectroscopy [42]. Three different techniques of optical visualization, infrared thermography, and acoustic high-frequency echography were employed in a comprehensive study [18] to examine the evaporation of butanol, ethanol, water/butanol, and water/ethanol droplets. Their results showed that due to the high hygroscopic power of ethanol, the humidity of the environment had a noticeable

effect on the evolution of pure ethanol droplets. Heterogeneous thermal patterns alongside the evolution of acoustic reflection coefficient proved that ethanol droplet undergoes continuous water loading. The combined influence of ambient temperature and relative humidity on early stages (i.e. pinned contact angle) of ethanol droplet was also examined [32]. In another study [50] the water loaded onto ethanol droplet was quantified by gas injection chromatography (GIC) under controlled ambient temperature and relative humidity. The observed reduction in ethanol concentration was attributed to both ethanol evaporation as well as water intake on the drop. They concluded that at low relative humidity the main mechanism for water intake was that of adsorption-absorption, though at high relative humidity water condensation plays a more dominant role. While the changes in relative humidity are commonly imposed environmental conditions, controlling ambient temperature to tune the effect of humidity is rather an expensive method for practical applications. The effects of relative humidity on methanol droplet evaporation was regulated by adjusting the temperature of the substrate [1, 2] which is less expensive compared to controlling ambient temperature. It was concluded that increasing substrate temperature maintains the liquid-gas interface temperature above the dew point which in turn limits the water condensation on the drop. A regime map was also proposed based on droplet evolution under various environmental conditions.

Multi-component droplets are present in most of the industrial applications. Ternary droplet and their evolution has been studied recently and showed very rich dynamics [92, 25, 54, 56]. In the previous ternary droplet studies, it was shown that the phase separation (nucleation of oil microdroplets) is triggered by preferential evaporation of the most volatile component. In this work we study the effect of relative humidity of the surrounding on the evolution of a binary droplet. We show that the nucleation of oil microdroplet can also be initiated by the absorption/adsorption and/or condensation of water vapor

present in the environment. Furthermore, we show how to control this effect by simply changing the substrate temperature. The results of this study is of great importance for instances when the operating liquid consists of some kind of oil and organic solvent and the water uptake results in undesired finished products. We show that tuning the substrate temperature can alleviate the unwanted effects of humidity. This is a cost-effective and more practical approach than controlling the humidity of the environment as it might be very costly to control the humidity of a large area or even impossible to fit the machines or even unsafe to do so.

In the present work, we first show the evaporation of methanol-anise oil mixture droplet under different relative humidity values and discuss the involved mechanisms. Subsequently, we show the side view and infrared (IR) visualization of evaporation of binary droplet under different relative humidity and substrate temperature. We show that the formation of ring is not only the function of relative humidity but substrate temperature as well. It should be noted the IR visualization of a ternary droplet has been done for the first time.

5.3 Experimental Methods

The schematics of the two setup that we use in this study are shown in Figure 5.1. Experiments are carried out in a temperature and humidity controlled chamber (with a dimension of $127 \times 127 \times 76\ mm^3$) of drop shape analyzer (DSA 100) from KRÜSS. The relative humidity (RH) and ambient temperature (T_{amb}) in the chamber were controlled between 20% and 80% and at 25 °C. For the effect of relative humidity at room temperature, the microscope is mounted on top and the evolution of droplet is recorded from the top. No temperature is imposed on the substrate. For the study of the combined effect of

substrate temperature and relative humidity, the bottom side of the chamber is equipped with a Peltier plate with temperature control. The tested substrate temperature ($T_{substrate}$) is between 15 °C and 35 °C. We have used both infrared (IR) camera and a CCD camera to simultaneously visualize droplet evolution from top and side. The infrared camera is fit to the top side of the chamber in a way that there is no large opening in the chamber for controlled humidity purposes. The needle was fitted in the chamber at an angle through a small hole at the top side. The DSA 100 equipment is placed on an optical anti-vibration table to eliminate environmental disturbances.

0.6 ml of anise oil is dissolved in 10 ml of methanol. The glass substrates are coated with a very thin PDMS (polydimethylsiloxane) layer to achieve spherical and reproducible droplets with measurable contact angles. The temperature and relative humidity of the chamber as well as substrate temperature are set to desired values. Enough time is allowed for the chamber and substrate to achieve quasi-steady state. Drops of methanol with specified volume are deposited on the coated substrate and let evaporate under the set conditions. Evolution of the drop is recorded with DSA 100 camera from the side at 50 frames per second and with IR camera from the top at 11 frames per second. Post-processing for optical microscopy is done with DSA Advanced software to study the time evolution of droplet contact angle (θ), base diameter (D), and volume (V). Elliptical fitting is used to compute the volume and contact angle of the droplet due to the observed differences in right and left contact angle. Post-processing for IR thermography was carried out with FLIR ResearchIR Max software. In order to confirm that methanol did not interact with the coating on the substrate, multiple droplets are repeatedly deposited at the same location. No change is observed in their initial contact angle or evolution during evaporation. The deposited droplet volumes are all smaller than 10 μl in order to keep the droplet size lower than the capillary length. The corresponding volume to the

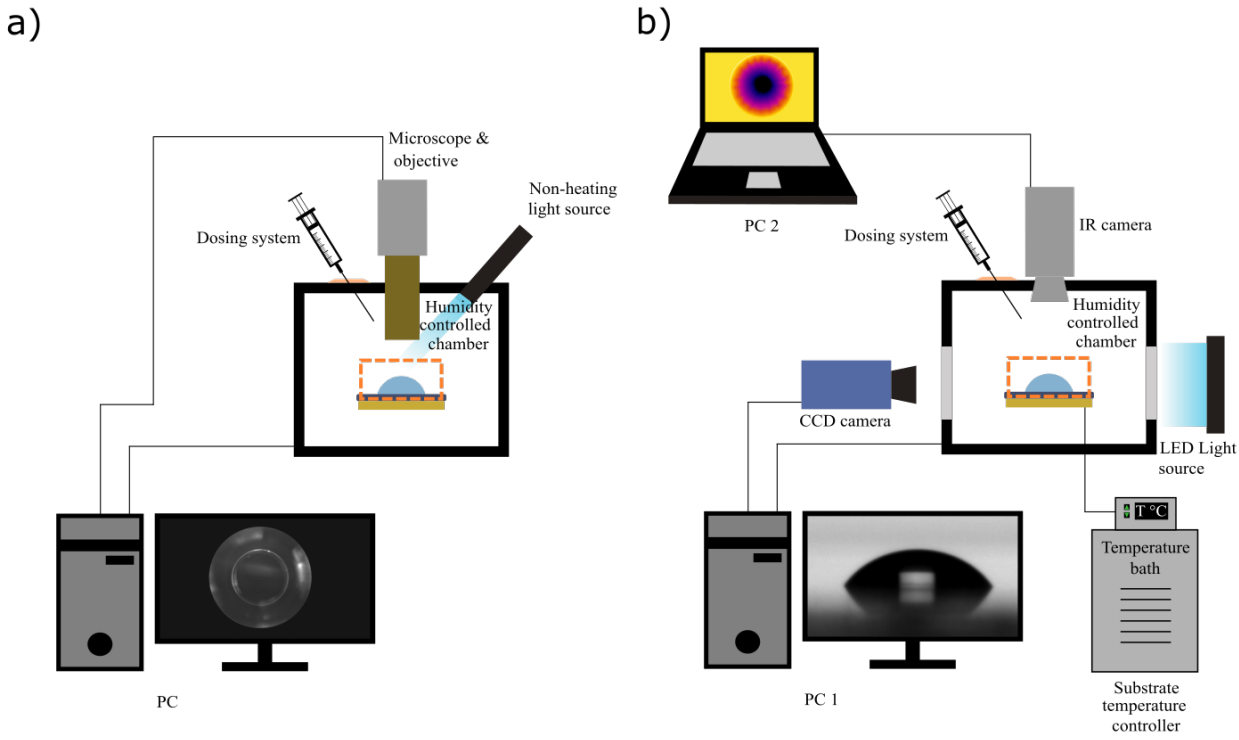

FIGURE 5.1: Schematic of experimental setups: a) optical microscopy from the top for studying the sole effect of humidity; b) simultaneous optical visualization from the side and infrared thermography from the top for studying the combined humidity and substrate temperature effect.

capillary length for methanol is around 45 μl.All experiments were repeated five times to ensure reproducible data. Base diameter (D) and volume (V) are normalized by their initial values i.e. $D^* = D/D_0$ and $V^* = V/V_0$, while the time t is nondimensionalized by final evaporation time of the droplet $t^* = t/t_f$.

5.4 Results and Discussion

Anise oil is soluble in methanol and results in transparent mixture. When a droplet of the mixture is deposited on a substrate, the volatile component which is methanol starts

to evaporate. Methanol is highly hygroscopic which means it dissolves water or water vapor. Therefore when a methanol and anise oil mixture drop is sitting on surface, the droplet absorbs/adsorbs water vapor present in the environment. Additionally, the gas-liquid interface temperature drops due to the evaporative cooling effect. If the interface temperature goes below the dew point, water vapor in the surrounding condenses on the droplet. These are the two mechanisms for water uptake in the droplet as it evaporates.

5.4.1 Relative Humidity Effect at Room Temperature

First, the sole effect of relative humidity is investigated using the setup shown in Figure 5.1.a. Three different values of relative humidity, i.e., 20%, 50%, and 80% are set and the evolution of droplet is recorded with the microscope on top. The successive images of droplet evolution under each relative humidity level of surrounding is demonstrated in Figure 5.2.a-c. When a drop of methanol and anise oil is deposited on the substrate, methanol start evaporating. At low relative humidity (RH = 20%), even though the amount of water vapor present in the air is low, due to high hygroscopic properties of methanol, the droplet absorbs/adsorbs some water. By both evaporation of methanol and water uptake on the droplet, the concentration of methanol decreases and thus the solubility of the liquid for anise oil. This results in the nucleation of oil microdroplets at the periphery of droplet. These microdroplets coalesce and creates an oil ring which occurs around 103 seconds. This oil ring takes on a shape of polygon until it transform into a triangle. This triangular middle section shows brighter corners (135 s) which suggests some localized internal flow at the corners. This localized internal flow has also been reported in non-circular droplet evaporation [71] as well as liquid-liquid phase separation inside aqueous droplets during molecule compartmentalization [35]. This triangular mid-section evolves into a circular shape and reduces in size as time progresses.

When relative humidity of surrounding is increased to 50%, the onset of the oil ring happens sooner. Under this condition, nucleation of oil microdroplets creates an opaque white middle section before turbulence starts at 83 s (see Figure 5.2). Oil microdroplets in the middle section merge together and then larger and larger oil droplet become noticeable at the middle section (88 s and 96 s). These large oil microdroplets gradually find their way to merge into the oil ring at the periphery. The middle section goes through a couple turbulence cycles until the middle section starts shrinking and evaporation stops. The remaining of droplet on the substrate mainly consists of anise oil.

If the relative humidity of the environment is increased even further (RH = 80%), much brighter middle section is observed at even earlier time of droplet lifetime (46s). This is due higher water uptake into the droplet which results in sudden nucleation of oil microdroplets. Microdroplets create an emulsion in the droplet scattering the light. The more microdroplet nucleated, the more light scattering and the brighter the middle section. After the bright middle section, the process is similar to RH of 50% where larger oil droplets are observed and they eventually merge to the oil ring. Unlike RH of 50% where the middle section disappears at the end, for RH of 80% the middle section plateaus to the specific size and do not change afterwards. This is due to the higher humidity of the surrounding where the water up taken by the droplet comes into equilibrium with surrounding. This behavior has been seen before at higher relative humidity values for binary droplet in chapter 2.

Figure 5.2.d demonstrates the time evolution of the areas of droplet, oil ring, and the middle section over time. It is seen that increasing the humidity results in appearance of the oil ring at earlier times. It is also observed that for RH of 20% and 50%, the area of the middle section goes to zero. However, for RH of 80%, the area of the middle section plateaus to a non-zero value. The effect of early onset of the oil ring is also shown by

the ratio of droplet diameter at the onset of the oil ring to droplet initial diameter (see Figure 5.3. The values are averaged for five droplets. It is seen that the for higher relative humidity the ratio of diameter is higher which corresponds to earlier times in droplet evaporation.

5.4.2 Combined Effect of Substrate Temperature and Relative Humidity of Surrounding

In order to investigate the combined effect of substrate temperature and relative humidity of surrounding, the set up shown in Figure 5.1.b is used. The CCD camera from the side gives information of time evolution of base diameter, D, contact angle, θ, and volume, V, of droplet while the information on thermal patterns on the droplet is recorded with the IR camera from the top. Three different levels of relative humidity (20%, 50%, and 80%) and three different values for substrate temperature ($15^{\circ}C$, $25^{\circ}C$ or room temperature, and $35^{\circ}C$) are used.

Optical Visualization

The time evolution of droplet base diameter as well as the diameter of the mid section and contact angle of droplet as well as the contact of the middle section on top are presented in Figure 5.4 for nine different condition of RH and T. We have superimposed the optical images with infrared images to accurately measure the diameter and contact angle of the mid section (shown in Figure 5.5). It is seen (Figure 5.4) that for higher relative humidity of surrounding and lower substrate temperatures the onset of the oil ring occurs earlier in droplet evaporation (i.e., higher values of D_{onset}/D and lower values of t_{onset}/t_f). It should be noted that no value is reported for t_{onset}/t_f for $RH = 80\%$ and $T = 35^{\circ}C$, the

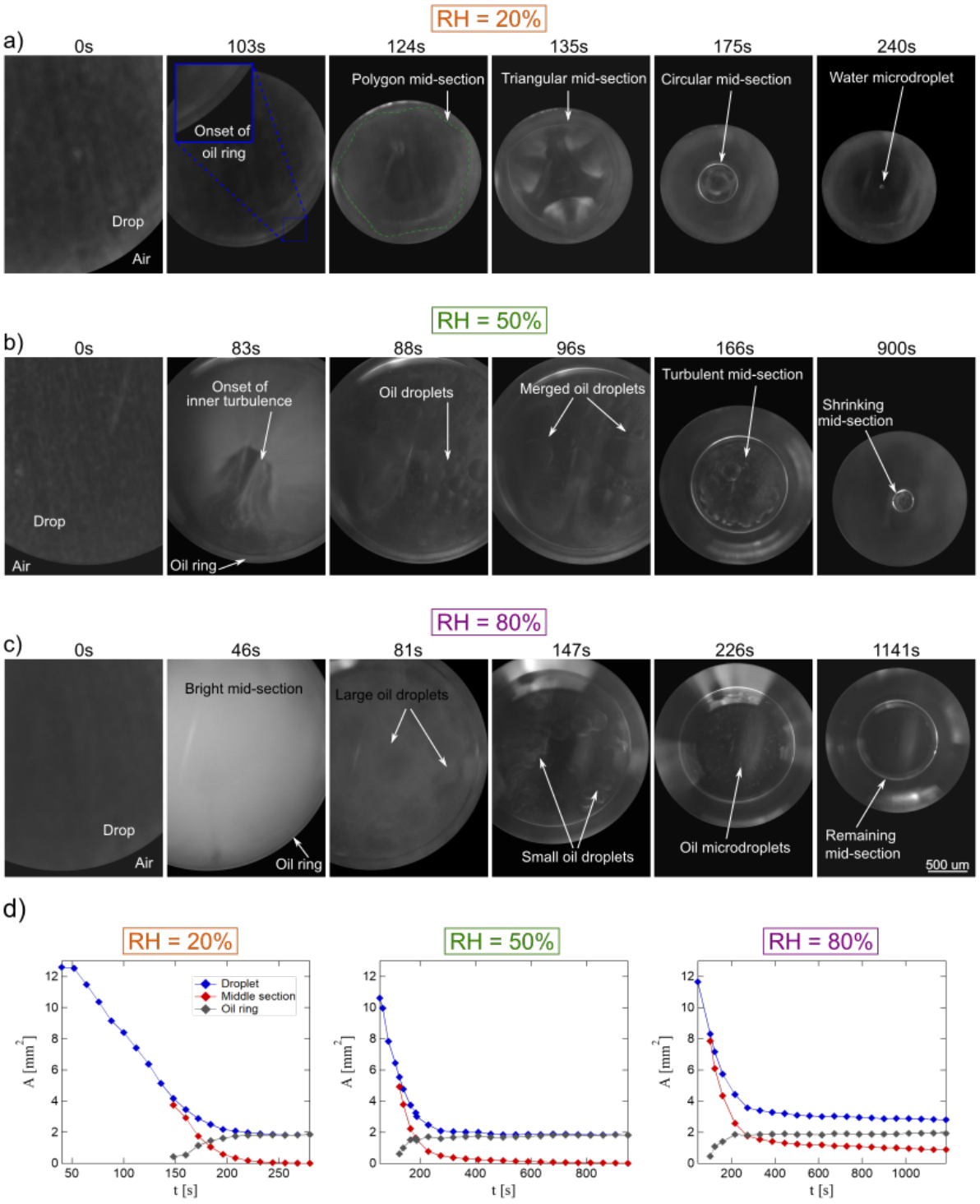

FIGURE 5.2: Successive images of methanol and anise oil mixture droplet; a) RH = 20 %, b) RH = 50 %, c) RH = 80 % all at room temperature; d) time evolution of area at different relative humidity of the environment and room temperature

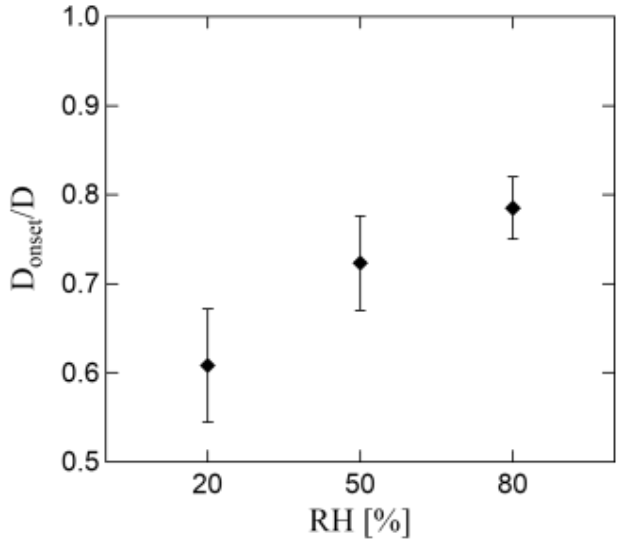

FIGURE 5.3: Dimensionless diameter of droplet at the onset of oil ring for different relative humidity of surrounding

lower left plot in the figure. The reason is due to the fact that the middle section comes to equilibrium with surrounding and the data recording is stopped. A value for t_{onset}/t_f based on the recording time span for this particular experiment would not reflect the underlying physics and would be a misleading value. It is observed that the latest occurrence of the oil ring happens for the highest substrate temperature and lowest humidity level (the top-right plot in Figure 5.4).

The maximum contact angle of the middle section, θ^*_{max}, is also measured and reported in Figure 5.4. The higher the value of maximum contact angle, the higher the water concentration in the middle section. As it is explained in Chapter 2 of this dissertation, increasing the substrate temperature has two effects on droplet evaporation. First, it increases the temperature of the liquid-gas interface above the due point temperature that lowers the possibility water vapor condensation at the interface. Second, it reduces the lifetime of droplet which restricts the amount of water vapor being absorbed/adsorbed

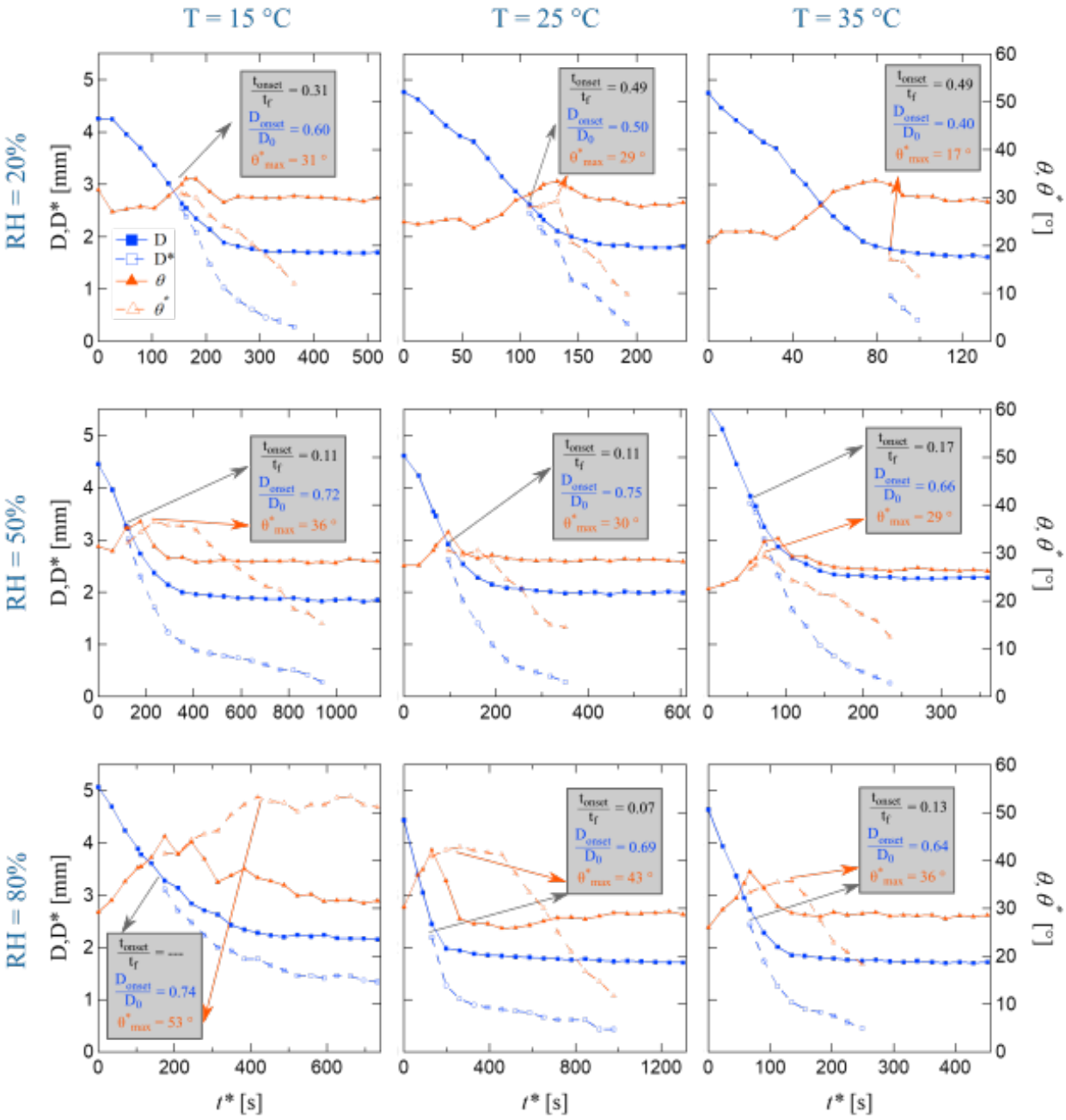

FIGURE 5.4: Evolution of diameter and contact angle under different relative humidity and substrate temperature values for a mixture droplet of methanol-anise oil. D and θ are the diameter and contact of droplet. D^* and θ^* are the diameter and contact angle of the middle section. Onset subscript corresponds to the onset of the oil ring in the droplet.

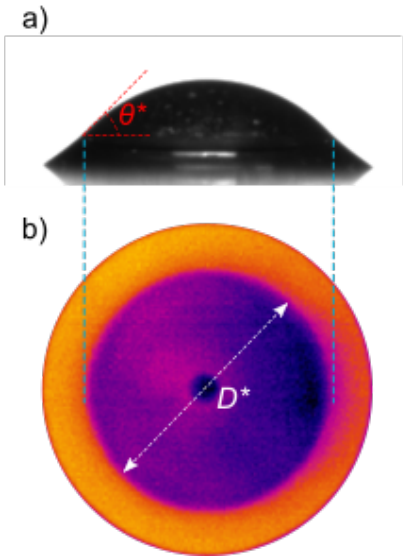

FIGURE 5.5: Ternary methanol-anise oil-water droplet at $RH = 80\%$ and $T = 15°C$; a) CCD camera side view, b) IR camera top view.

into droplet. Consistent with the above explanation, it is seen that the highest value for $\theta^*_{max} = 53°C$ is for $RH = 80\%$ and $T = 15°C$ and the lowest value is for $\theta^*_{max} = 17°C$ is for $RH = 20\%$ and $T = 35°C$.

Infrared Thermography

Organic liquid droplets develop thermal-convective instabilities driven by evaporation. These instabilities are referred to as hydrothermal waves [86] that are caused by surface tension gradients along the liquid-gas interface. It has been reported that as water gets into ethanol droplets, these hydrothermal waves disappear [32, 18]. These instabilities are not observed in water and the reason is not yet fully understood. It is attributed to the fact that air-water interface easily gets contaminated and it might be a reason for the absence of these waves in water droplets. Therefore, in our study, the presence of the hydrothermal waves are used as indirect measure for the concentration of methanol in droplet. These waves are formed near to the triple line and move in azimuthal direction.

It is seen that the evolution of the number of waves goes under three different stages. Initially the waves are distributed in an organized manner at droplet periphery and the number of waves decreases (0 to 3 s in Figure 5.6.a) until it reaches a state of a plateau. During this stage, the shape of the waves become irregular and their number stays relatively constant (3 to 60 s in Figure 5.6.a). At the last stage, the waves transform into slow moving cells ad their number decrease until their disappear (60 to 100 s in Figure 5.6.a). Under two condition of $RH = 20\%$, $T = 15^{\circ}C$ and $RH = 50\%$, $T = 15^{\circ}C$, the turbulence inside droplet is observed as secondary waves. These secondary waves show up the periphery of the middle section and follow the similar three stage evolution of the primary hydrothermal waves (see Figure 5.6.b). To the best of our knowledge, these waves are not reported in the literature previously. We think they might be the disturbances in the middle section due to oil microdroplet nucleation and merging to the oil ring that disturbs the thermal pattern in the drop.

The time evolution of the number of waves for all nine conditions of RH and T are shown in Figure 5.7. The initial decrease in the number of waves are very sharp and seems to be following a power law. The inset of the profiles zoom on the initial drop in the number of waves in log-log scale. The data in the log-log scale can be fit by a linear line which confirms the reduction in number of waves with a power law. These results are in agreement with the evolution of the number of waves at the initial stage of evaporation of ethanol droplet in study by Sobac and Brutin [86]. The middle stage where the number of waves stay relatively constant are fitted by a horizontal green line. The inclined green lines represent a fitted line to the number of waves at the last stage. It can be observed that the number of waves in all stages are relatively higher for higher temperatures. It is also evident from the two plots in 5.7, $RH = 20\%$, $T = 15^{\circ}C$ and $RH = 50\%$, $T = 15^{\circ}C$, that the lifespan of the secondary hydrothermal waves are much shorter than the primary

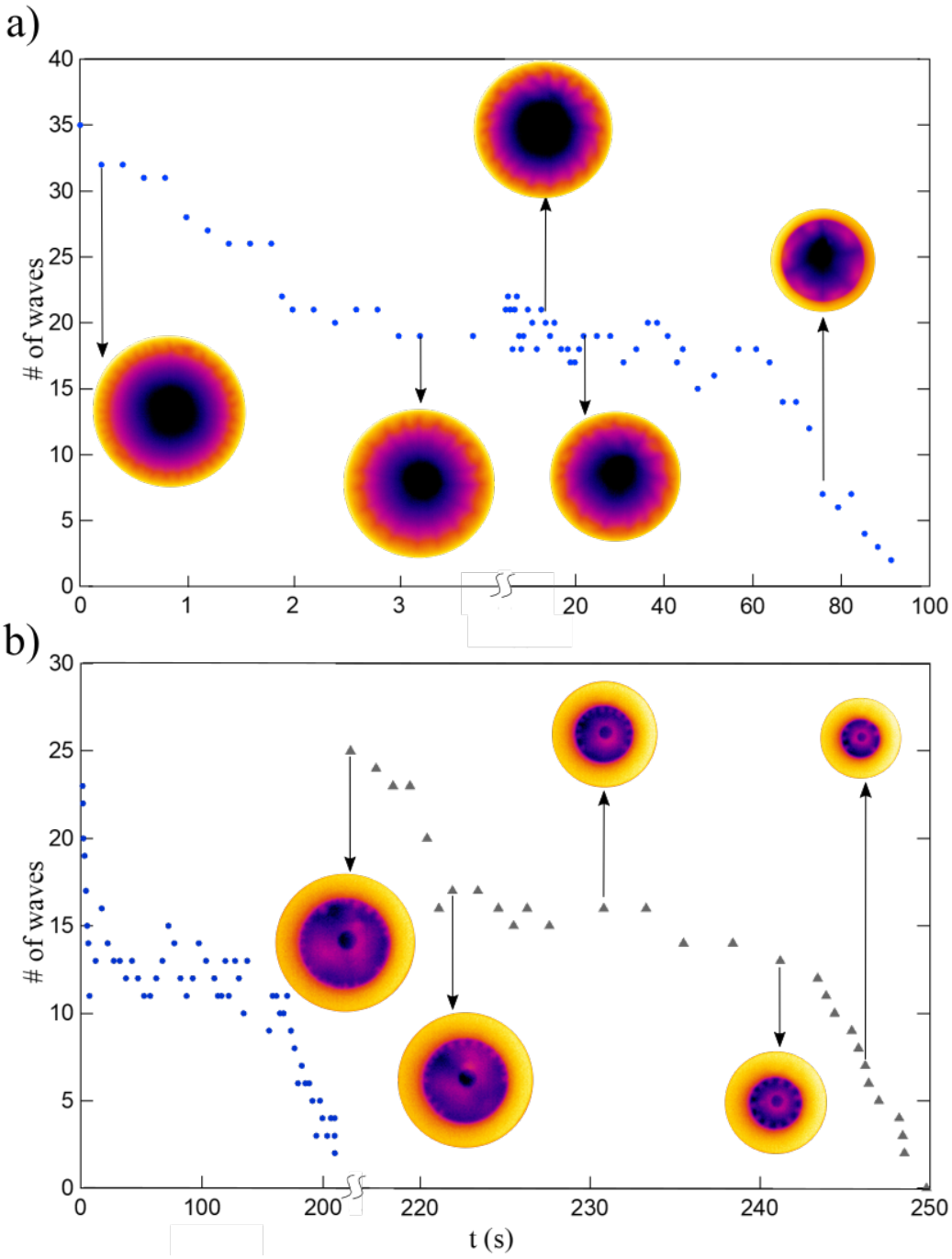

FIGURE 5.6: Time evolution of the number of hydrothermal waves: a) $RH = 70\%$, $T = 35°C$; b) $RH = 20\%$, $T = 15°C$. The blue circular markers represent the number of primary hydrothermal waves and the grey triangular markers correspond to the number of secondary hydrothermal waves. The snapshot of droplet with IR camera are connected to their corresponding data points in the plots. The horizontal time axes are not uniformly scaled.

ones.

As the size of droplet and its base diameter increases, the number of hydrothermal waves forming near droplet periphery rises. The nature of these hydrothermal waves are the thermal instabilities that are caused by surface tension gradient. Surface tension is dependant on temperature of the interface as well the concentration of each component. We have also noticed that higher humidity of the environment results in more water uptake on the droplet and therefore faster disappearance of the thermal waves. Figure 5.8 illustrates that all data collapse using the following function:

$$N_w = f((RH(\frac{t}{t_f}))^b) \tag{5.1}$$

Using the following scaling and the constant from fitting the data, the number of waves is calculated:

$$N_w = 7.13(\frac{d_0}{L_c})(\frac{\Delta T}{T_{amb}})(RH(\frac{t}{t_f}))^{-0.301} \tag{5.2}$$

where d_0, L_c, ΔT, T_{amb} are the initial base diameter, capillary length, temperature difference between the apex and close to contact line of droplet, and ambient temperature. A similar scaling for the vertical axes has been used in a previous work by Sobac and Brutin [86]. It is interesting to see that the effect of surrounding humidity, effects the time axes for the physics of hydrothermal waves rather than the number of waves. The scaling used for Figure 5.8 is in accordance with the physics of evaporation. The larger the temperature difference between the apex and periphery of droplet, the stronger the surface tension gradients and the more noticeable the thermal instabilities as hydrothermal waves.

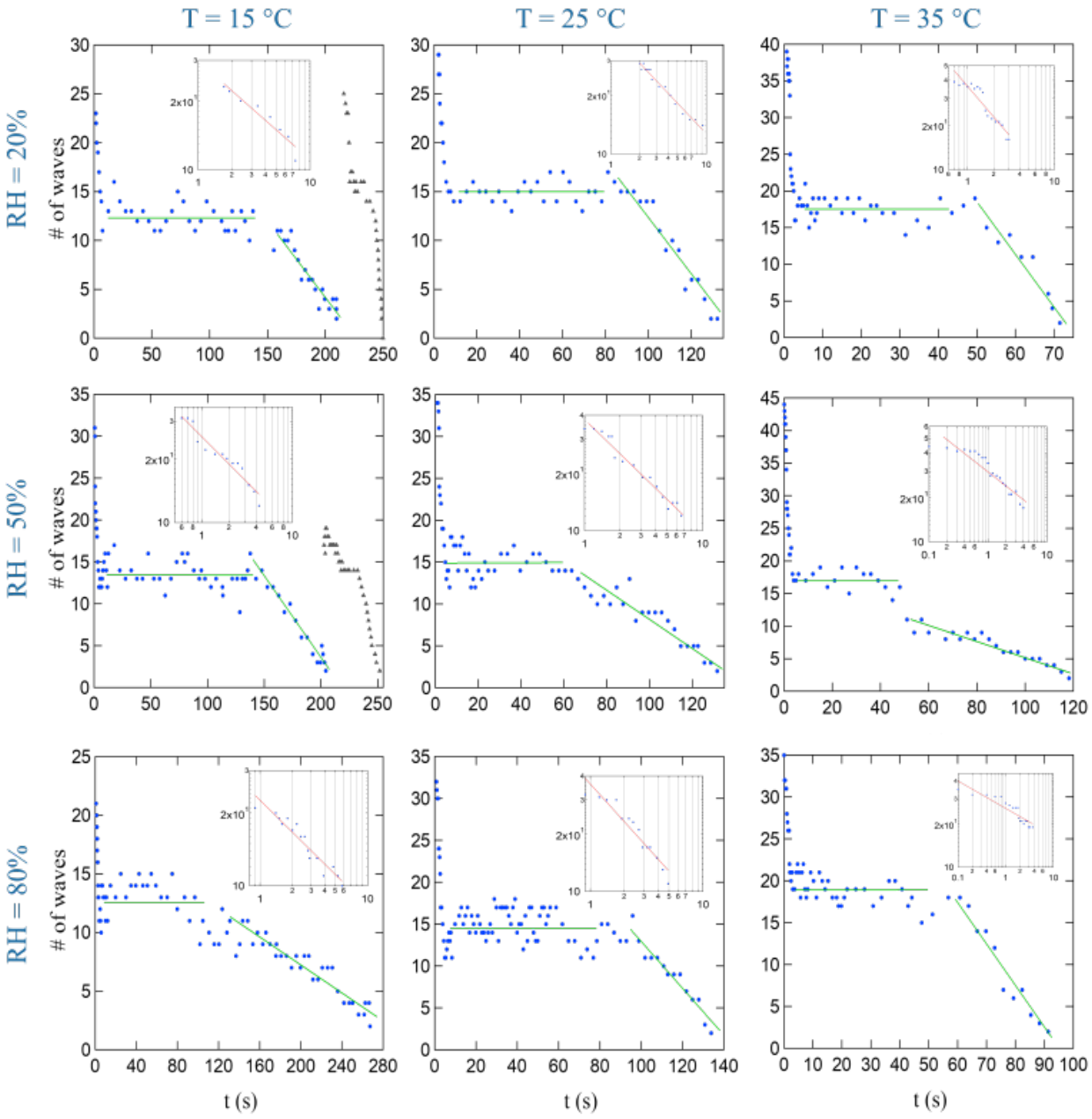

FIGURE 5.7: Number of hydrothermal waves (HTWs) versus time at different relative humidity (RH) of surrounding and substrate temperature (T); inset shows the early sharp decline in number of waves in log-log scale. The markers are similar to Figure 5.7.

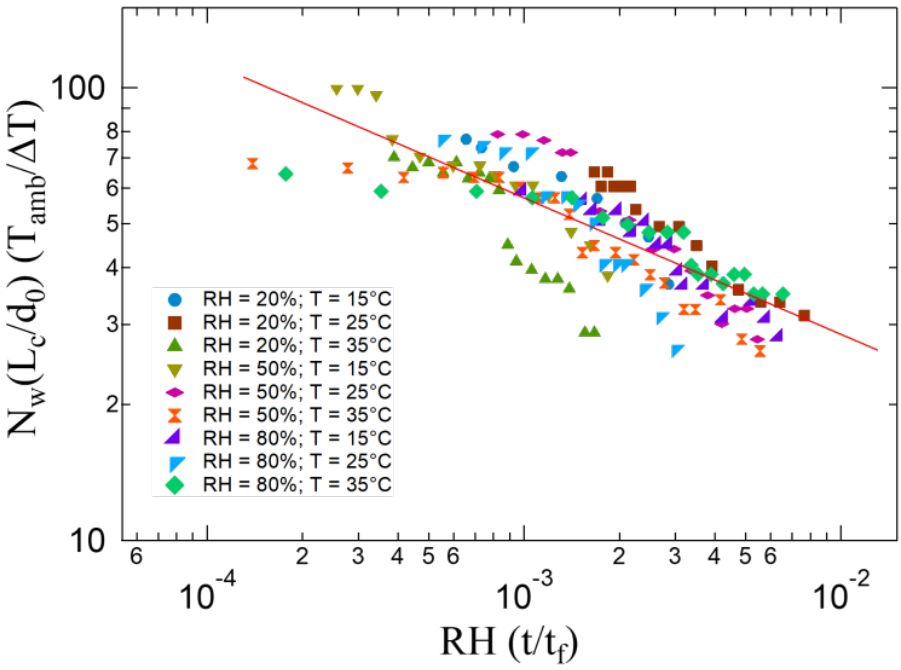

FIGURE 5.8: Scaled number of hydrothermal waves versus scaled normalized time for various relative humidity of surrounding and substrate temperatures in log-log scale. Experimental data (different shades and symbols) and fit by power law $N_w = a(d_0/Lc)(\Delta T/T_{amb})(RH(t/t_f))^b$ with $a = 7.13$ and $b = -0.301$.

5.5 Conclusion

The Ouzo effect is studied in evaporating methanol-anise oil mixture droplets under various relative humidity of surrounding and temperature of substrate. Two different experimental setup are used in order to perform the study. First, the sole effect of humidity on evaporation of droplet is recorded from the top by an optical microscope. Our results revealed different mechanisms during droplet evaporation. A polygon middle section is formed at low humidity levels transforming into triangular mid-section. Strong localized internal flow is observed at the triangle corners. At higher humidity levels, the droplet became opaque white color which showed the nucleation of oil microdroplets. The higher the relative humidity, the brighter the droplet gets. After this phase, large oil droplets appear at the droplet surface at the middle section. These oil droplets merge together and become larger until they merge into the oil ring at the periphery of droplet. If the humidity level is so high that the up taken water onto the droplet comes to equilibrium with surrounding, a middle section of droplet does not shrink, instead it reaches a plateau and remains of relatively constant area. Our results also demonstrated that as the relative humidity increases the onset of the oil ring occurs sooner in droplet lifetime.

For investigating the combined effect of substrate temperature and relative humidity of surrounding, simultaneous optical microscopy and infrared thermography are used. Superposition of infrared and optical images are carried out for accurate measurements of the middle section diameter and contact angle at each time. It is observed that at higher substrate temperature and lower relative humidity of surrounding, the water uptake is the lowest with the lowest value for the maximum contact angle of the middle section. As relative humidity increases or substrate temperature decreases, the onset of the oil ring

occurs sooner with higher maximum contact angle of the middle section which represents higher water uptake. Infrared thermography revealed three stages of evolution of the number of hydrothermal waves in the droplets. It is seen that higher substrate temperature increases the number of waves in all stages. Aside from primary hydrothermal waves, secondary waves were also observed for two conditions with much shorter lifespan compared to primary hydrothermal waves. The number of hydrothermal waves and their regularity is an indirect measure of methanol concentration inside droplet.

Chapter 6

Conclusion

In this dissertation, evaporation of binary and multi-component droplets have been investigated through experimental and data-driven techniques and the effects of environmental conditions such as humidity of surrounding and substrate temperature on behavior of these droplets are tested and analyzed.

In Chapter 2, an experimental investigation is carried out to study the combined effect of substrate temperature and relative humidity of the environment on evaporation of pure methanol droplet. While humidity of the environment is usually an imposed condition that results in unwanted effects on behavior of droplet, controlling the temperature of substrate is a low-cost and easy approach to eliminate the unwanted effects. In this study, we tested three different relative humidity values and three different substrate temperatures. It was observed that at low relative humidity of the surrounding, droplet undergoes three stages of evaporation: constant, slightly increasing, and sharply decreasing contact angle while volume and diameter drop continuously. No significant effect of substrate temperature was noticed on the qualitative behavior of droplet during evaporation at low relative humidity. Increasing substrate temperature expedites the evaporation process and shortens the lifetime of droplet. At high relative humidity, substrate temperature plays a role on the evolution of droplet. At high temperature, droplet

experiences two stages of evaporation. The contact angle rises to a maximum value while both volume and diameter decrease, then it drops until the end of droplet lifetime. If the substrate temperature is low enough, the drop undergoes a single stage of evaporation where contact angle, volume, and diameter reach plateau and droplet stops evaporating. Water vapor present in humid environment gets adsorbed-absorbed and possibly condensed on the droplet. Changing the substrate temperature affects the temperature at the liquid-gas interface. If the temperature at the liquid-gas interface drops below the dew point at that specific relative humidity, the condensation of water takes place in addition to adsorption-absorption of water. This will result in more water uptake on the droplet and will change its evolution. Also, when the humidity of surrounding is high, increasing the substrate temperature decreases the droplet lifetime that restricts the amount of water uptake into the droplet. The maximum value of contact angle during evaporation is lower than that of pure water which confirms the presence of residual methanol in the drop after the first stage of evaporation. Evaporation rate enhances by increasing substrate temperature and reduces by rising the relative humidity. The enhancement in total evaporation time with increase in relative humidity is more pronounced for lower substrate temperature. This is due to the lower dew point temperature at higher relative humidity as well as lower liquid-gas interface temperature which augments the condensation of water on the droplet. The initial evaporation rate is found to be independent of relative humidity of surrounding. A regime map was suggested based on different evolution of droplet under different conditions of surrounding and substrate. The presented approach suggests that the unwanted environmental effects on droplet evaporation can be alleviated and controlled by tuning the temperature of the substrate. The idea can be applied to any industrial application involving droplet evaporation such as ink-jet printing, fabrication techniques, etc.

In Chapter 3, machine learning and data-driven technique are employed to detect the humidity of surrounding by analyzing the evolution of macroscopic parameters of droplet during evaporation. Two different classifiers have been tested: Naive Bayes and bagged decision tree. Three models were built based on input variables. Model a only contains dimensionless contact angle and time as features, however models b and c include extra information on temperature and diameter in dimensionless and dimensional format, respectively. As expected, bagged decision tree Classifier produced more accurate results with all three models compared to Naive Bayes. Model b and c produce more accurate results compared to model a for decision tree classifier. However, the performance of Naïve Bayes does not improve from model a to models b or c. Since decision tree has more robust algorithm, it benefits from extra information given to the classifier (i.e., model b or c compared to model a), however Naïve Bayes classifier does not make use of extra information provided to the classifier. Further examining the predictions made by Naive Bayes revealed that the algorithm defines threshold values for contact angle. However, it was not so transparent how Bagged Decision Tree was making predictions. The effect of input data distribution was examined with both algorithms and all three models. It was observed that Bagged Decision Tree was very stable and did not change by altering the input data distribution. Models b and c of Naive Bayes were also quite intact by input data distribution. Nevertheless, the results of model a with Naive Bayes Classifier changed substantially by input data distribution. The reason is changing input data distribution changed the threshold values for contact angle. Therefore, the accuracy for RH = 20% decreases while it increases for RH = 50%.

In Chapter 4, we further analyze the behavior of sessile droplet evaporation that start

with a single component and evolves into a binary system. Machine learning, classification and regression, techniques have been used to estimate the regime of droplet evaporation as well as humidity of the surrounding, and evolution of diameter and contact angle over time. Point-by-point analysis of droplet profile enables time-dependent estimations given a limited number of data points. This means that the model does not need the entire evolution profile of a droplet to make an estimation. Instead, only a few (or even a single) data points are (is) sufficient for estimation, although more data points result in more accurate estimation. The model estimation capability is then assessed on the data that do not contribute to training, testing, or validation. Two different classifiers are utilized to estimate the regime of droplet evaporation. NB is chosen as a simple easy-to-interpret algorithm, while DT serves as a more powerful algorithm. As expected, DT outperforms NB due to a more robust internal structure at the expense of computational cost and transparency. Both classifiers showed impressive performance (minimum 75% accuracy) on estimating the regime of droplet. Knowledge on droplet evaporation regime is necessary for compatible designs in numerous industries such as droplet-based biosensors or inkjet printing. Additionally, level of surrounding humidity, time evolution of droplet base diameter, and time evolution of droplet contact angle are estimated through regression techniques. Polynomial regressors, as well as regression tree, are trained through point-by-point analysis of droplet evolution. The model performance improved by increasing the order of the polynomial and using regression tree for training, test, and validation sets. However, when estimating the new conditions unseen by the model, fourth-order polynomial and regression tree suffered from data over-fitting. The best performance of the model is achieved by third-order polynomial. In general, the model estimation results are more accurate when estimating diameter evolution compared to contact angle estimation. This is due to smoother, hence easier to estimate, evolution of diameter with time.

The sharp changes in θ^* under different conditions make the estimation of its evolution challenging for the model. Information of this type is of great importance for technologies such as ink-jet printing, or droplet-based biodiagnostics where the estimations can provide critical information on the base diameter or contact angle of the droplet at a specific time. In the current work, behavior of a sessile droplet transitioning from a single fluid into a binary mixture following transfer of a second component from the atmosphere is studied through data-driven techniques. The model demonstrated promising performance detecting the regime of droplet evolution, the humidity level surrounding droplet, and time evolution of diameter and contact angle. The proposed method to study the dynamics of droplet evaporation through machine learning techniques can be expanded to analyze the complex physics underlying interfacial fluid mechanics.

In Chapter 5, evaporation of a ternary droplet is studied experimentally. Droplet evaporation starts as a binary, methanol -anise oil, droplet and evolves into a ternary droplet consisting methanol-anise oil-water. Since anise oil is soluble in methanol and non-solvable in water, the capability of the mixture to dissolve anise oil decreases by increasing water concentration. This will result in oil microdroplet nucleation creating an emulsion that is called Ouzo effect. The mixture will appear milky white due to the scattering of light by microdroplets. The combined effect of surrounding humidity and substrate temperature is investigated. Two different experimental setups are used in order to perform the study. First, the sole effect of humidity on evaporation of droplet is recorded from the top by an optical microscope. Our results revealed different mechanisms during droplet evaporation. A polygon middle section is formed at low humidity levels transforming into triangular mid-section. Strong localized internal flow is observed at the triangle corners. At higher humidity levels, the droplet became opaque white color which showed the nucleation of oil microdroplets. The higher the relative humidity, the

brighter the droplet gets. After this phase, large oil droplets appear at the droplet surface at the middle section. These oil droplets merge together and become larger until they merge into the oil ring at the periphery of droplet. If the humidity level is so high that the up taken water onto the droplet comes to equilibrium with surrounding, a middle section of droplet does not shrink, instead it reaches a plateau and remains of relatively constant area. Our results also demonstrated that as the relative humidity increases the onset of the oil ring occurs sooner in droplet lifetime. For investigating the combined effect of substrate temperature and relative humidity of surrounding, simultaneous optical microscopy and infrared thermography are used. Superposition of infrared and optical images are carried out for accurate measurements of the middle section diameter and contact angle at each time. It is observed that at higher substrate temperature and lower relative humidity of surrounding, the water uptake is the lowest with the lowest value for the maximum contact angle of the middle section. As relative humidity increases or substrate temperature decreases, the onset of the oil ring occurs sooner with higher maximum contact angle of the middle section which represents higher water uptake. Infrared thermography revealed three stages of evolution of the number of hydrothermal waves in the droplets. It is seen that higher substrate temperature increases the number of waves in all stages. Aside from primary hydrothermal waves, secondary waves were also observed for two conditions with much shorter lifespan compared to primary hydrothermal waves. The number of hydrothermal waves and their regularity is an indirect measure of methanol concentration inside droplet.

In conclusion, in the present dissertation, the physics of binary and multi-component sessile droplet evaporation is studied experimentally and through data-driven and machine learning techniques. We have shown that the unwanted effect of humidity of surrounding can be reversed by tuning the temperature of substrate for both binary and

ternary droplets which suggests a low-cost and easy to implement approach for the quality of final products in numerous industries such as biodiagnostics, microfabrication, printing, and irrigation. We have also developed machine learning algorithms to analyze the behavior of binary sessile droplet. Our results and conclusion introduce a great potential in opening up new ways to study and analyze the intricate physics underlying interfacial fluid mechanics. Our simultaneous optical microscopy and infrared thermography for ternary droplet evaporation revealed interesting physics of hydrothermal instabilities known as hydrothermal waves. Even thought extensive research has been performed in the field of interfacial fluid mechanics and sessile droplet evaporation, fully understanding the underlying physics of evaporation needs more sophisticated equipment. Also, the advances in the field of data-science show great potential in analyzing such complex phenomena which still needs to be explored.

Appendix A

Empirical Model on Methanol Droplet Evaporation

A diffusion-limited model employed in this work based on the assumption that the evaporation from the droplet is quasi-steady and limited by the diffusion of vapor in the surrounding gas. It is also considered that the size of droplet is small enough to neglect the gravitational effects. The geometry of the model is illustrated in Figure A.1 in cylindrical coordinates. The free surface of droplet, $z = h(r, t)$, is a spherical cap with radius R = R(t) (R>R), contact radius $R = R(t)$ $(R \geq 0)$, and contact angle $\theta = \theta(t)$ $(0 \leq \theta \leq \pi)$ given by

$$h = -\mathrm{R}\cos\theta \pm \sqrt{R^2 - r^2}, \text{where} \mathrm{R} = \frac{R}{\sin\theta} \tag{A.1}$$

When $\pi/2 < \theta \leq \pi$, the non-negative part of h given by the above equation is a double-valued function of r for $R \leq r <$ R, with plus and minus signs corresponding to the upper and lower hemispheres. The volume of droplet, V is given by

$$V = 2\pi \int_0^R hrdr = \frac{\pi R^3}{3} \frac{\sin\theta(2 + \cos\theta)}{(1 + \cos\theta)^2} \tag{A.2}$$

and the initial volume of droplet is given by

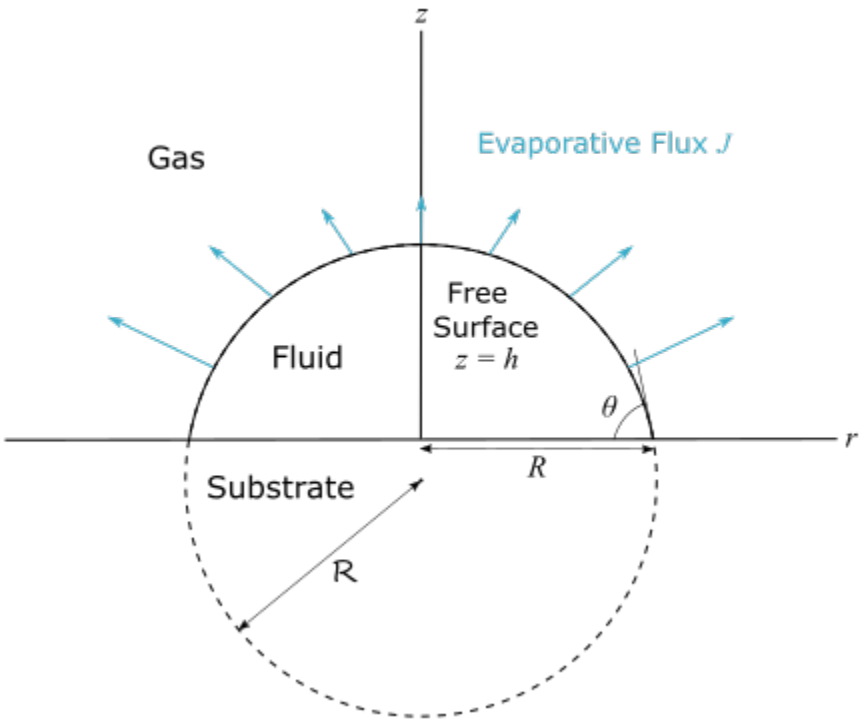

FIGURE A.1: a) Geometry of the mathematical model. Free surface of droplet, $z = h$, is a spherical cap with radius R, contact radius R, and contact angle θ. The arrows show the evaporative flux from the free surface of the droplet into the surrounding gas. Adapted from Stauber et al. [89].

$$V_0 = \frac{\pi R^3}{3} \frac{\sin\theta_0 (2 + \cos\theta_0)}{(1 + \cos\theta_0)^2} \tag{A.3}$$

The droplet evaporation rate is estimated with Popov's evaporative model for a moving contact line [65, 89] as:

$$\frac{dV}{dt} = -\frac{\pi D (c_{sat} - c_\infty)}{\rho} \frac{R g(\theta)}{(1 + \cos\theta)^2} \tag{A.4}$$

where D is the diffusion coefficient of methanol in air, and ρ is the density of liquid droplet. c_{sat} and c_∞ are the saturation concentration of methanol and concentration of

methanol far away from the interface, respectively. $g(\theta)$ is a function that takes into account the non-uniform diffusion along liquid-gas interface and is given by:

$$g(\theta) = (1 + \cos\theta)^2 \left\{ \tan\frac{\theta}{2} + 8\int_0^8 \frac{\cosh^2\theta\tau}{\sinh 2\pi\tau} \tanh[\tau(\pi - \theta)]d\tau \right\} \tag{A.5}$$

Vapor transport by buoyant convection is assumed to be negligible [87]. The influence of evaporative cooling of the droplet on evaporation rate is also neglected. The present model assumes that vapor transport occurs mainly by diffusion of vapor. The characteristic time for diffusion is $t_D = R^2/D$. The diffusion time for methanol or water vapor in the air is on the order of 10^{-2} to 10^{-1} s. It is also supposed that evaporation occurs in quasisteady fashion because the diffusion time is much smaller than the average evaporation time $t_D/t_f \approx 10^{-4}$. This means that the vapor concentration adjusts fast in comparison with the time needed for evaporation.

When the temperature of the substrate is the same as the temperature of the surrounding, both c_{sat} and c_∞ are calculated at T_{amb}. When the temperature of the substrate is different from the temperature of surrounding, our model assumes that the temperature of the liquid-gas interface is the same as substrate temperature. Assuming the interface is isothermal at the substrate temperature (T_{subs}) is reasonable due to the difference in thermal conductivity of air compared to thermal conductivity of methanol and water. Thermal conductivity of both methanol and water are about an order of magnitude larger than thermal conductivity of air. Based on Fourier's law of conduction $q = -kA\frac{dT}{dx}$ where q, k, and A are heat flux (W), thermal conductivity $(W/m.k)$, and area (m^2), the temperature difference between the liquid and substrate is much smaller than the temperature difference between substrate and surrounding air. This assumption has been used previously in literature for the case of water droplet evaporating on hot substrates [87]. Therefore

for substrate temperatures other than the room temperature the concentration difference is calculated as $\Delta c = c_{sat}(T_{subs}) - c_{\infty}(T_{amb})$ where T_{subs} and T_{amb} represent substrate temperature and temperature of surrounding, respectively.

We have used this empirical model to calculate the time evolution of volume for methanol droplet evaporation. The evolution of droplet base radius and contact angle are the input for the model as well as the temperature of the substrate and surrounding. Figure A.2 demonstrates the volume evolution versus time for all nine RH and T conditions. It can be seen that for all the nine conditions, the evaporation rate is underestimated with the model. This is due to the importance of buoyant convection in the surrounding air. It is noteworthy that the present model does not take into account the adsorption/absorption and possible condensation of water into droplet as well as the reduction in the concentration of methanol in the droplet. It is observed that for higher levels of humidity, the model predicts shorter lifetime for droplet compared to the experiments. This is due to the fact that by water uptake, the lifetime of droplet is increased which is not accounted in the model.

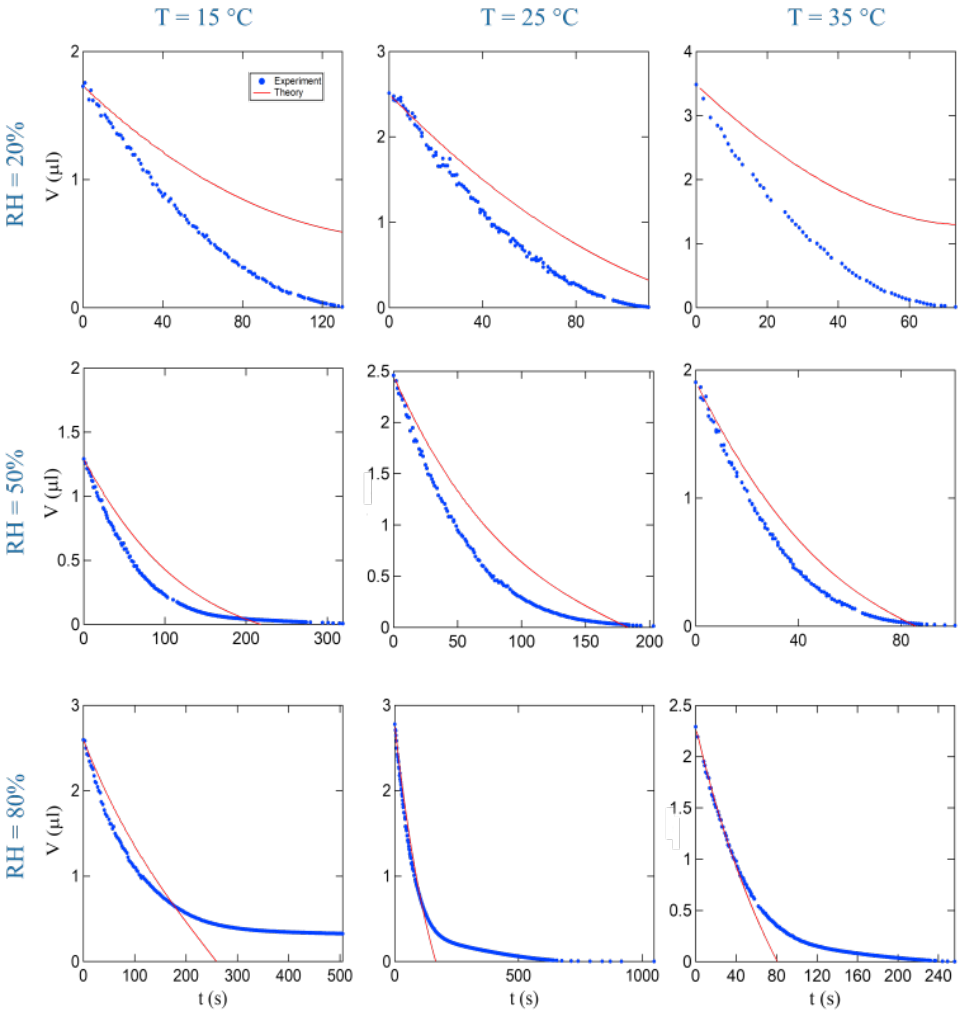

FIGURE A.2: Time evolution of volume for methanol droplet evaporation: empirical model vs. experimental data.

Appendix B

Ternary Diagram of Methanol- Water- Anise Oil

Anise oil is soluble in methanol while being non-soluble in water. The solubility of anise oil in a mixture of methanol-water decrease as the concentration of water increases. The ternary diagram of methanol- water- anise oil is shown in Figure B.1. The mixture of anise oil and methanol is transparent. When the water is added to the mixture, the solubility of mixture decreases and the mixture cannot hold as much anise oil. Therefore, the excess anise oil nucleates as oil microdroplets. The microdroplets create a suspension and the color of the mixture become opaque white as a result of light scattering by microdroplets. The ternary diagram for methanol- water- anise oil is shown in Figure B.1. The orange shaded represents the region where the microdroplet nucleation, i.e., Ouzo effect, occurs. The white region corresponds to the region where the mixture stays transparent due to very small amount of anise oil in the mixture or very little amount of water in the mixture.

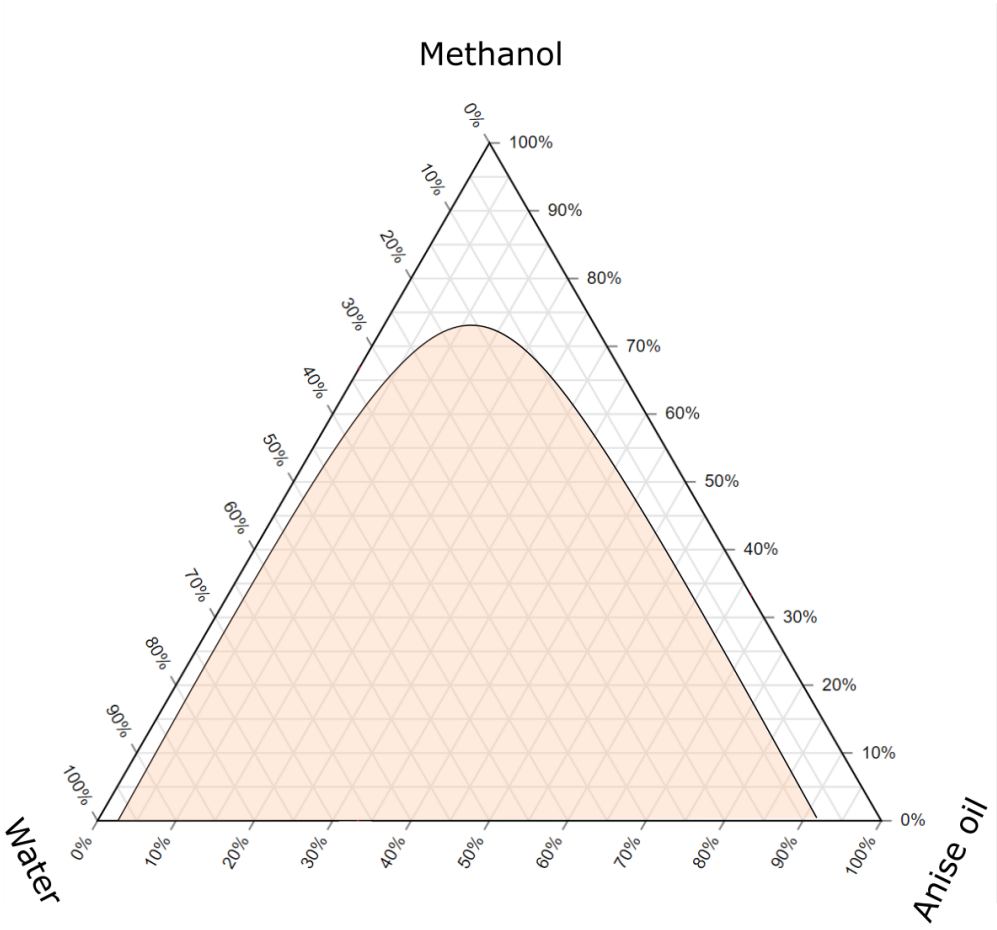

FIGURE B.1: Ternary diagram of methanol- water- anise oil. The orange shaded represents the region where oil microdroplet nucleation occurs, i.e., Ouzo effect.

Appendix C

Empirical Model on Evaporation of Ternary Droplet

In this section, we have developed an empirical model for time evolution of volume for ternary droplet under nine conditions. The model is similar to the one in Appendix B for binary droplet. The difference for ternary droplet is that anise oil present in the droplet does not evaporate and therefore does not contribute to the evaporation rate from droplet, however, it is measured in the experiments. Therefore, it appears as the integration constant for volume of the droplet. The volume of the oil is calculated both from the mixing ratio of the fluid for droplet as well as the volume of the remaining droplet for condition when humidity of surrounding is low and temperature of substrate is high so that all volatile components, i.e., water and methanol, fully evaporates. The evaporation rate is similar to binary droplet as:

$$\frac{dV}{dt} = -\frac{\pi D(c_{sat} - c_{\infty})}{\rho} \frac{Rg(\theta)}{(1+\cos\theta)^2} \tag{C.1}$$

where D is the diffusion coefficient of methanol in air, and ρ is the density of liquid droplet. c_{sat} and c_{∞} are the saturation concentration of methanol and concentration of

methanol far away from the interface, respectively. $g(\theta)$ is a function that takes into account the non-uniform diffusion along liquid-gas interface and is given by:

$$g(\theta) = (1+\cos\theta)^2 \left\{ \tan\frac{\theta}{2} + 8\int_0^8 \frac{\cosh^2\theta\tau}{\sinh 2\pi\tau} \tanh[\tau(\pi-\theta)]d\tau \right\} \tag{C.2}$$

The volume of anise oil is added as a constant when the volume of droplet calculated as the integral of the evaporation rate as follows:

$$\int_{V_0}^{V} dV = -\frac{\pi D(c_{sat}-c_\infty)}{\rho}\int_0^{t_f} \frac{Rg(\theta)}{(1+\cos\theta)^2}dt \tag{C.3}$$

$$V = V_0 - \frac{\pi D(c_{sat}-c_\infty)}{\rho}\int_0^{t_f} \frac{Rg(\theta)}{(1+\cos\theta)^2}dt + V_{\text{anise oil}} \tag{C.4}$$

The evolution of methanol- anise oil droplet versus time is shown in Figure C.1 for nine different conditions. It is seen that rate of evaporation is underestimated by the model. This is due to the role of buoyant convection in the surrounding air which is not taken into account in the model. It is noteworthy that even though the volume of the anise oil is added as a constant to the volume of droplet, it still cannot predict plateau of droplet volume at the right time.

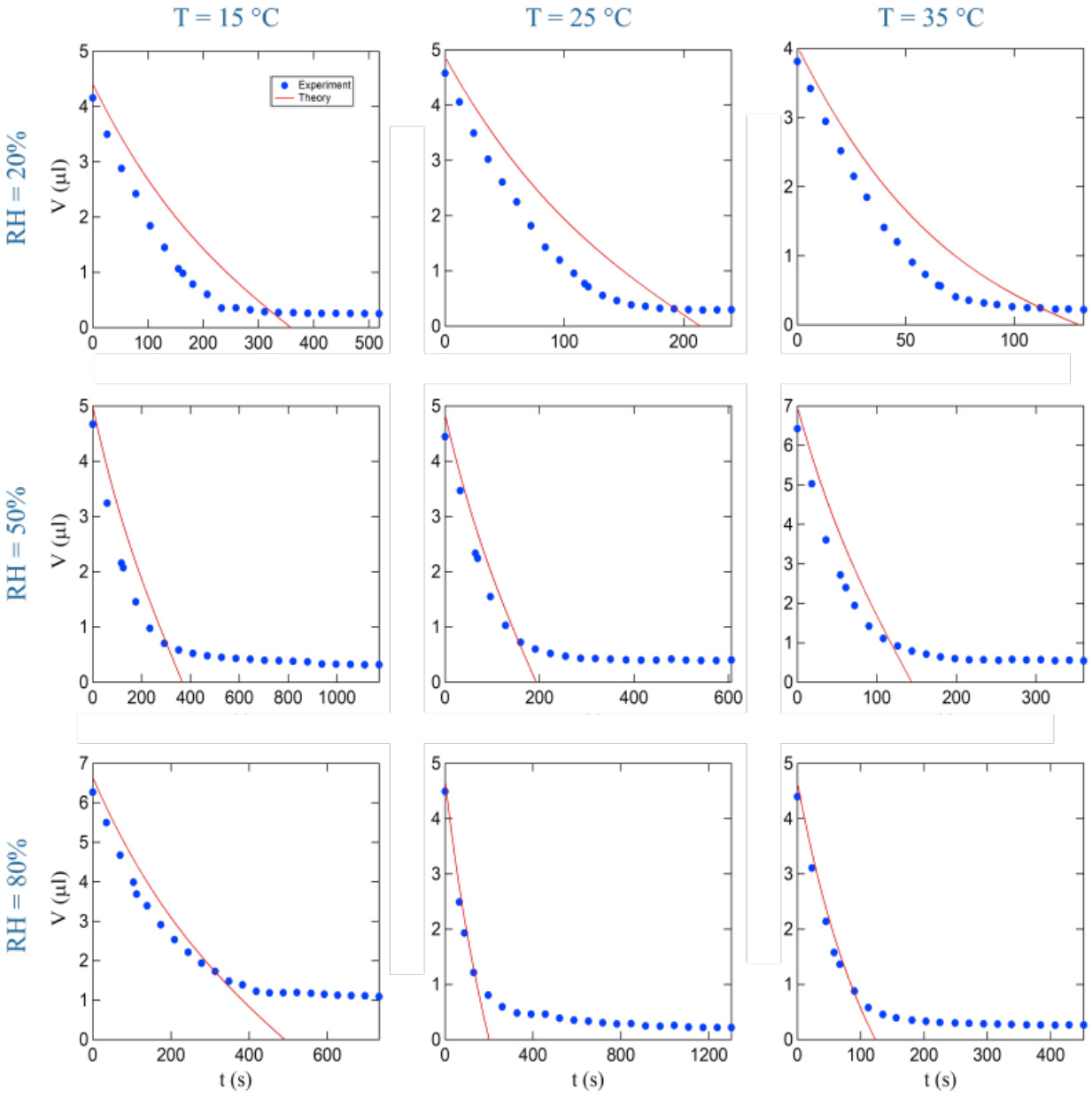

FIGURE C.1: Time evolution of volume for methanol- anise oil droplet evaporation: empirical model vs. experimental data.

Bibliography

[1] Sahar Andalib, Ali Alshehri, and Pirouz Kavehpour. "Combined effect of relative humidity and substrate temperature on evaporation of methanol droplet". In: *Journal of Coatings Technology and Research* 16.6 (2019), pp. 1691–1698.

[2] Sahar Andalib, Ali Alshehri, and Pirouz Kavehpour. "Effect of a second component in organic droplet evaporation: initially present versus absorbed during the process". In: *APS Division of Fluid Dynamics Meeting Abstracts*. 2019, pp. M04–031.

[3] Sahar Andalib and Pirouz Kavehpour. "Effect of Evaporation Rate on Stick-Slip Behavior of the Contact Line". In: *Bulletin of the American Physical Society* 63 (2018).

[4] Sahar Andalib and Pirouz Kavehpour. "Experimental Investigation of Evaporation Rate of a Droplet on Behavior of the Contact Line." In: *19th International Coating Science and Technology Symposium*. 2018, pp. xx–xx.

[5] Sahar Andalib and Pirouz Kavehpour. "Fluorescence microscopy of precursor films in evaporating droplets". In: *APS Division of Fluid Dynamics Meeting Abstracts*. 2017, Q11–003.

[6] Vance Bergeron et al. "Controlling droplet deposition with polymer additives". In: *Nature* 405.6788 (2000), p. 772.

[7] Rajneesh Bhardwaj, Jon P Longtin, and Daniel Attinger. "A numerical investigation on the influence of liquid properties and interfacial heat transfer during microdroplet deposition onto a glass substrate". In: *International Journal of Heat and Mass Transfer* 50.15-16 (2007), pp. 2912–2923.

[8] Liu Bin, Rachid Bennacer, and Adrien Bouvet. "Evaporation of methanol droplet on the Teflon surface under different air velocities". In: *Applied thermal engineering* 31.17-18 (2011), pp. 3792–3798.

[9] Christopher M Bishop. *Pattern recognition and machine learning*. springer, 2006.

[10] Daniel Bonn et al. "Wetting and spreading". In: *Reviews of Modern Physics* 81.2 (2009), p. 739.

[11] "Bootstrap aggregation (bagging) of regression trees using treebagger. Available online:
https://www.mathworks.com/help/stats/regression-treeBagger-examples.html". In:

[12] MP Brenner, JD Eldredge, and JB Freund. "Perspective on machine learning for advancing fluid mechanics". In: *Physical Review Fluids* 4.10 (2019), p. 100501.

[13] Steven L Brunton, Bernd R Noack, and Petros Koumoutsakos. "Machine learning for fluid mechanics". In: *Annual Review of Fluid Mechanics* 52 (2020), pp. 477–508.

[14] D Brutin and V Starov. "Recent advances in droplet wetting and evaporation". In: *Chemical Society Reviews* 47.2 (2018), pp. 558–585.

[15] David Brutin et al. "Pattern formation in drying drops of blood". In: *Journal of fluid mechanics* 667 (2011), p. 85.

[16] Wray Lindsay Buntine. “A theory of learning classification rules”. PhD thesis. university of technology, sydney, 1990.

[17] Anne-Marie Cazabat and Geoffroy Guena. “Evaporation of macroscopic sessile droplets”. In: *Soft Matter* 6.12 (2010), pp. 2591–2612.

[18] Pin Chen et al. “Evaporation of binary sessile drops: infrared and acoustic methods to track alcohol concentration at the interface and on the surface”. In: *Langmuir* 32.38 (2016), pp. 9836–9845.

[19] Manish Chopra et al. “DNA molecular configurations in an evaporating droplet near a glass surface”. In: *Journal of Rheology* 47.5 (2003), pp. 1111–1132.

[20] “CVpartition. Available online: https://www.mathworks.com/help/stats/cvpartition.html”. In:

[21] S David, K Sefiane, and L Tadrist. “Experimental investigation of the effect of thermal properties of the substrate in the wetting and evaporation of sessile drops”. In: *Colloids and Surfaces A: Physicochemical and Engineering Aspects* 298.1-2 (2007), pp. 108–114.

[22] B-J De Gans, Paul C Duineveld, and Ulrich S Schubert. “Inkjet printing of polymers: state of the art and future developments”. In: *Adv. Mater.* 16.3 (2004), pp. 203–213.

[23] B-J De Gans, Paul C Duineveld, and Ulrich S Schubert. “Inkjet printing of polymers: state of the art and future developments”. In: *Advanced materials* 16.3 (2004), pp. 203–213.

[24] Robert D Deegan et al. “Capillary flow as the cause of ring stains from dried liquid drops”. In: *Nature* 389.6653 (1997), pp. 827–829.

[25] Christian Diddens et al. “Evaporating pure, binary and ternary droplets: thermal effects and axial symmetry breaking”. In: *Journal of Fluid Mechanics* 823 (2017), pp. 470–497.

[26] Richard O Duda, Peter E Hart, and David G Stork. *Pattern classification*. John Wiley & Sons, 2012.

[27] Vincent Dugas, Jérôme Broutin, and Eliane Souteyrand. “Droplet evaporation study applied to DNA chip manufacturing”. In: *Langmuir* 21.20 (2005), pp. 9130–9136.

[28] Karthik Duraisamy, Gianluca Iaccarino, and Heng Xiao. “Turbulence modeling in the age of data”. In: *Annual Review of Fluid Mechanics* 51 (2019), pp. 357–377.

[29] Thomas Duriez, Steven L Brunton, and Bernd R Noack. *Machine learning control-taming nonlinear dynamics and turbulence*. Vol. 116. Springer, 2017.

[30] Kai Fukami, Koji Fukagata, and Kunihiko Taira. “Assessment of supervised machine learning methods for fluid flows”. In: *Theoretical and Computational Fluid Dynamics* 34.4 (2020), pp. 497–519.

[31] Kai Fukami, Koji Fukagata, and Kunihiko Taira. “Super-resolution reconstruction of turbulent flows with machine learning”. In: *Journal of Fluid Mechanics* 870 (2019), pp. 106–120.

[32] Yuki Fukatani et al. “Effect of ambient temperature and relative humidity on interfacial temperature during early stages of drop evaporation”. In: *Physical Review E* 93.4 (2016), p. 043103.

[33] Heather Meloy Gorr, Ziye Xiong, and John A Barnard. “Pattern recognition for identification of lysozyme droplet solution chemistry”. In: *Colloids and Surfaces B: Biointerfaces* 115 (2014), pp. 170–175.

[34] Christopher P Gulka et al. “Coffee rings as low-resource diagnostics: detection of the malaria biomarker Plasmodium falciparum histidine-rich protein-II using a surface-coupled ring of Ni (II) NTA gold-plated polystyrene particles”. In: *ACS Appl. Mater. Interfaces* 6.9 (2014), pp. 6257–6263.

[35] Wei Guo et al. “Non-associative phase separation in an evaporating droplet as a model for prebiotic compartmentalization”. In: *Nature Communications* 12.1 (2021), pp. 1–13.

[36] Isabelle Guyon and André Elisseeff. “An introduction to variable and feature selection”. In: *Journal of machine learning research* 3.Mar (2003), pp. 1157–1182.

[37] Lama Hamadeh et al. “Machine Learning Analysis for Quantitative Discrimination of Dried Blood Droplets”. In: *Scientific Reports* 10.1 (2020), pp. 1–13.

[38] B. Harrington. *Inkscape*. `http://www.inkscape.org`. 2004-2005.

[39] Wei Hou, Darwin Darakananda, and Jeff D Eldredge. “Machine-learning-based detection of aerodynamic disturbances using surface pressure measurements”. In: *AIAA Journal* 57.12 (2019), pp. 5079–5093.

[40] Hua Hu and Ronald G Larson. “Evaporation of a sessile droplet on a substrate”. In: *Journal of Physical Chemistry B* 106.6 (2002), pp. 1334–1344.

[41] Cedric Hurth et al. “Biomolecular interactions control the shape of stains from drying droplets of complex fluids”. In: *Chemical Engineering Science* 137 (2015), pp. 398–403.

[42] Plinio Innocenzi et al. “Evaporation of ethanol and ethanol- water mixtures studied by time-resolved infrared spectroscopy”. In: *The Journal of Physical Chemistry A* 112.29 (2008), pp. 6512–6516.

[43] Suat Irmak et al. “Irrigation efficiency and uniformity, and crop water use efficiency”. In: (2011).

[44] RB Jadrich, BA Lindquist, and TM Truskett. “Unsupervised machine learning for detection of phase transitions in off-lattice systems. I. Foundations”. In: *The Journal of chemical physics* 149.19 (2018), p. 194109.

[45] Junping Jing et al. “Automated high resolution optical mapping using arrayed, fluid-fixed DNA molecules”. In: *Proceedings of the National Academy of Sciences* 95.14 (1998), pp. 8046–8051.

[46] Carlos RG Junior et al. “A Machine Learning-Based Approach for Prediction of Plant Protection Product Deposition”. In: *2017 Brazilian Conference on Intelligent Systems (BRACIS)*. IEEE. 2017, pp. 234–239.

[47] Takeo Kawase et al. “Inkjet printed via-hole interconnections and resistors for all-polymer transistor circuits”. In: *Adv. Mater.* 13.21 (2001), pp. 1601–1605.

[48] Anthony A Killeen et al. “Protein self-organization patterns in dried serum reveal changes in B-cell disorders”. In: *Molecular diagnosis & therapy* 10.6 (2006), pp. 371–380.

[49] Namwon Kim et al. “Identification of fluid and substrate chemistry based on automatic pattern recognition of stains”. In: *Analytical Methods* 4.1 (2012), pp. 50–57.

[50] Yutaku Kita et al. “Quantifying vapor transfer into evaporating ethanol drops in a humid atmosphere”. In: *Physical Chemistry Chemical Physics* 20.29 (2018), pp. 19430–19440.

[51] I Kononenko. *Comparison of inductive and naive Bayesian learning approaches to automatic knowledge adquisition. B. Wielinga Editors, Current trends in Knowledge Adquisition*. 1990.

[52] Pat Langley. “Induction of recursive Bayesian classifiers”. In: *European Conference on Machine Learning*. Springer. 1993, pp. 153–164.

[53] Pat Langley and Stephanie Sage. “Induction of selective Bayesian classifiers”. In: *Uncertainty Proceedings 1994*. Elsevier, 1994, pp. 399–406.

[54] Yaxing Li et al. “Evaporation-triggered segregation of sessile binary droplets”. In: *Physical review letters* 120.22 (2018), p. 224501.

[55] Chuanjun Liu, Elmar Bonaccurso, and Hans-Jürgen Butt. “Evaporation of sessile water/ethanol drops in a controlled environment”. In: *Physical Chemistry Chemical Physics* 10.47 (2008), pp. 7150–7157.

[56] Detlef Lohse and Xuehua Zhang. “Physicochemical hydrodynamics of droplets out of equilibrium”. In: *Nature Reviews Physics* 2.8 (2020), pp. 426–443.

[57] R Mollaret et al. “Experimental and numerical investigation of the evaporation into air of a drop on a heated surface”. In: *Chemical Engineering Research and Design* 82.4 (2004), pp. 471–480.

[58] B Molle et al. “Evaporation and wind drift losses during sprinkler irrigation influenced by droplet size distribution”. In: *Irrigation and Drainage* 61.2 (2012), pp. 240–250.

[59] Vaisala Oyj. “Calculation Formulas for Humidity—Humidity Conversion Formulas”. In: *Vaisala: Helsinki, Finland* (2013).

[60] Jungho Park and Jooho Moon. “Control of colloidal particle deposit patterns within picoliter droplets ejected by ink-jet printing”. In: *Langmuir* 22.8 (2006), pp. 3506–3513.

[61] Aaron H Persad, Khellil Sefiane, and Charles A Ward. “Source of temperature and pressure pulsations during sessile droplet evaporation into multicomponent atmospheres”. In: *Langmuir* 29.43 (2013), pp. 13239–13250.

[62] JL Plawsky et al. “Nano-and microstructures for thin-film evaporation—A review”. In: *Nanoscale and microscale thermophysical engineering* 18.3 (2014), pp. 251–269.

[63] Joel L Plawsky et al. “Review of the effects of surface topography, surface chemistry, and fluid physics on evaporation at the contact line”. In: *Chemical Engineering Communications* 196.5 (2008), pp. 658–696.

[64] Pavel P Popov et al. “Machine learning-assisted early ignition prediction in a complex flow”. In: *Combustion and Flame* 206 (2019), pp. 451–466.

[65] Yuri O Popov. “Evaporative deposition patterns: spatial dimensions of the deposit”. In: *Physical Review E* 71.3 (2005), p. 036313.

[66] Maziar Raissi et al. “Deep learning of vortex-induced vibrations”. In: *Journal of Fluid Mechanics* 861 (2019), pp. 119–137.

[67] J Sunil Rao and William JE Potts. “Visualizing Bagged Decision Trees.” In: *KDD*. 1997, pp. 243–246.

[68] Sebastian Raschka. “Model evaluation, model selection, and algorithm selection in machine learning”. In: *arXiv preprint arXiv:1811.12808* (2018).

[69] WD Ristenpart et al. “Influence of substrate conductivity on circulation reversal in evaporating drops”. In: *Physical Review Letters* 99.23 (2007), p. 234502.

[70] Thomas Rückstieß, Christian Osendorfer, and Patrick van der Smagt. “Sequential feature selection for classification”. In: *Australasian Joint Conference on Artificial Intelligence*. Springer. 2011, pp. 132–141.

[71] PJ Sáenz et al. "Dynamics and universal scaling law in geometrically-controlled sessile drop evaporation". In: *Nature communications* 8.1 (2017), pp. 1–9.

[72] S Rasoul Safavian and David Landgrebe. "A survey of decision tree classifier methodology". In: *IEEE transactions on systems, man, and cybernetics* 21.3 (1991), pp. 660–674.

[73] K Sefiane and R Bennacer. "Nanofluids droplets evaporation kinetics and wetting dynamics on rough heated substrates". In: *Advances in Colloid and Interface Science* 147 (2009), pp. 263–271.

[74] K Sefiane and L Tadrist. "Experimental investigation of the de-pinning phenomenon on rough surfaces of volatile drops". In: *International Communications in Heat and Mass Transfer* 33.4 (2006), pp. 482–490.

[75] K Sefiane, L Tadrist, and M Douglas. "Experimental study of evaporating water–ethanol mixture sessile drop: influence of concentration". In: *International Journal of Heat and Mass Transfer* 46.23 (2003), pp. 4527–4534.

[76] K. Sefiane et al. "On the effect of the atmosphere on the evaporation of sessile droplets of water". In: *Physics of Fluids* 21.6 (2009), p. 062101.

[77] Khellil Sefiane. "The coupling between evaporation and adsorbed surfactant accumulation and its effect on the wetting and spreading behaviour of volatile drops on a hot surface". In: *Journal of Petroleum Science and Engineering* 51.3-4 (2006), pp. 238–252.

[78] Khellil Sefiane, Samuel David, and Martin ER Shanahan. "Wetting and evaporation of binary mixture drops". In: *Journal of Physical Chemistry B* 112.36 (2008), pp. 11317–11323.

[79] "Sequential Feature Selection. Available online: https://www.mathworks.com/help/stats/sequentialfs.html". In:

[80] VN Shabalin and SN Shatokhina. "Diagnostic markers in the structures of human biological liquids". In: *Singapore medical journal* 48.5 (2007), p. 440.

[81] Noushine Shahidzadeh-Bonn et al. "Evaporating droplets". In: *Journal of Fluid Mechanics* 549 (2006), p. 307.

[82] Shai Shalev-Shwartz and Shai Ben-David. *Understanding machine learning: From theory to algorithms*. Cambridge university press, 2014.

[83] TA Shedd and AG Pautsch. "Spray impingement cooling with single-and multiple-nozzle arrays. Part II: Visualization and empirical models". In: *International Journal of Heat and Mass Transfer* 48.15 (2005), pp. 3176–3184.

[84] Anand Pratap Singh, Shivaji Medida, and Karthik Duraisamy. "Machine-learning-augmented predictive modeling of turbulent separated flows over airfoils". In: *AIAA Journal* 55.7 (2017), pp. 2215–2227.

[85] Patrick J Smith and Dong H Shin. *Inkjet-based micromanufacturing*. John Wiley & Sons, 2012.

[86] Benjamin Sobac and David Brutin. "Thermocapillary instabilities in an evaporating drop deposited onto a heated substrate". In: *Physics of fluids* 24.3 (2012), p. 032103.

[87] Benjamin. Sobac and David Brutin. "Thermal effects of the substrate on water droplet evaporation". In: *Physical Review E* 86.2 (2012), p. 021602.

[88] Christof Sodtke and Peter Stephan. "Spray cooling on micro structured surfaces". In: *International Journal of Heat and Mass Transfer* 50.19-20 (2007), pp. 4089–4097.

[89] Jutta M Stauber et al. "On the lifetimes of evaporating droplets with related initial and receding contact angles". In: *Physics of fluids* 27.12 (2015), p. 122101.

[90] Xinjun Su et al. “Enhancement of heat transport in oscillating heat pipe with ternary fluid”. In: *International Journal of Heat and Mass Transfer* 87 (2015), pp. 258–264.

[91] Philip H Swain and Hans Hauska. “The decision tree classifier: Design and potential”. In: *IEEE Transactions on Geoscience Electronics* 15.3 (1977), pp. 142–147.

[92] Huanshu Tan et al. “Evaporation-triggered microdroplet nucleation and the four life phases of an evaporating Ouzo drop”. In: *Proceedings of the National Academy of Sciences* 113.31 (2016), pp. 8642–8647.

[93] Joshua R Trantum, David W Wright, and Frederick R Haselton. “Biomarker-mediated disruption of coffee-ring formation as a low resource diagnostic indicator”. In: *Langmuir* 28.4 (2012), pp. 2187–2193.

[94] Siddhartha Verma, Guido Novati, and Petros Koumoutsakos. “Efficient collective swimming by harnessing vortices through deep reinforcement learning”. In: *Proceedings of the National Academy of Sciences* 115.23 (2018), pp. 5849–5854.

[95] Tatiana A Yakhno et al. “The informative-capacity phenomenon of drying drops”. In: *IEEE engineering in medicine and biology magazine* 24.2 (2005), pp. 96–104.

[96] Duyang Zang et al. “Evaporation of a droplet: From physics to applications”. In: *Physics Reports* 804 (2019), pp. 1–56.

[97] Alexander Zien et al. “The feature importance ranking measure”. In: *Joint European Conference on Machine Learning and Knowledge Discovery in Databases*. Springer. 2009, pp. 694–709.